A New Experiment Run Group Proposal Submitted to Jefferson Lab PAC44

A Search for Hybrid Baryons in Hall B with CLAS12

Volker Burkert *(Spokesperson)*, Daniel S. Carman *(Spokesperson)*, Valery Kubarovsky, Victor Mokeev *(Spokesperson)*, Maurizio Ungaro, Veronique Ziegler
Thomas Jefferson National Accelerator Facility, Newport News, Virginia 23606, USA

Annalisa D'Angelo *(Contact Person, Spokesperson)*, Lucilla Lanza, Alessandro Rizzo
Università di Roma Tor Vergata and INFN Roma Tor Vergata, 00133 Rome, Italy

Gleb Fedotov, Boris Ishkhanov, Evgeny Isupov, Evgeny Golovach *(Spokesperson)*
Skobeltsyn Institute of Physics, Moscow State University, 119234 Moscow, Russia

Ralf W. Gothe *(Spokesperson)*, Iuliia Skorodumina
University of South Carolina, Columbia, South Carolina 29208, USA

Vincent Mathieu[†], Vladyslav Pauk, Alessandro Pilloni, Adam Szczepaniak[†]
Theory Center, Jefferson Laboratory, Newport News, Virginia 23606, USA
([†]*Joint with Indiana University, Bloomington, Indiana 47405, USA*)

Simon Capstick, Volker Crede
Florida State University, Tallahassee, Florida 32306, USA

Jan Ryckebusch
Ghent University, B-9000 Ghent, Belgium

Michael Döring
The George Washington University, Washington, DC 20052, USA

Philip Cole
Idaho State University, Pocatello, Idaho 83209, USA

Vincenzo Bellini, Francesco Mammoliti, Giuseppe Russo, Concetta Sutera, Francesco Tortorici
INFN, Sezione di Catania, 95125 Catania, Italy

Ilaria Balossino, Luca Barion, Giuseppe Ciullo, Marco Contalbrigo, Paola Lenisa, Aram Movsisyan, Luciano Pappalardo, Mateo Turisini
INFN, Sezione di Ferrara, 44100 Ferrara, Italy

Marco Battaglieri, Andrea Celentano, Raffaella De Vita, Erica Fanchini, Mikhail Osipenko, Marco Ripani, Elena Santopinto, Mauro Taiuti
INFN, Sezione di Genova, 16146 Genova, Italy

Alessandra Filippi
INFN, Sezione di Torino, 10125 Torino, Italy

César Fernández-Ramírez
Universidad Nacional Autónoma de México, 04510 Mexico City, Mexico

Inna Aznauryan
Yerevan Physics Institute, 375036 Yerevan, Armenia

and the CLAS Collaboration

Abstract

This proposal aims to establish a program to search for new excited baryon states in the mass range from 1.8 GeV to 3 GeV, as well as to explore for the first time the behavior of resonance electrocouplings over the full spectrum of excited proton states at photon virtualities Q^2 approaching the photon point ($Q^2 < 0.2$ GeV^2). This work focuses on measuring $K^+\Lambda$, $K^+\Sigma^0$, and $\pi^+\pi^- p$ exclusive final states in CLAS12 and detecting the scattered electrons in the angular range from 2.5° to 35° using the electron detection capabilities of the Forward Tagger and the CLAS12 detector. The experiment will use longitudinally polarized electron beams of 6.6 GeV and 8.8 GeV to cover the range of invariant mass W up to 3 GeV and Q^2 from 0.05 GeV^2 to 2 GeV^2. The main aspects of this proposal are to:

- search for new hybrid baryon states with the glue as an extra constituent component beyond the three constituent quarks by focusing on measurements at $Q^2 <$ 1.0 GeV^2 where the expected magnitudes of the hybrid electroexcitation amplitudes are maximal;

- search for three-quark "missing" resonances in the electroproduction of different hadronic final states with the highest fluxes of virtual photons ever achieved in exclusive meson electroproduction experiments;

- study the structure of prominent nucleon resonances in the mass range up to 3 GeV in the regime of large meson-baryon cloud contributions and explore the N^* longitudinal electroexcitation approaching the photon point.

Exclusive events from KY and $\pi^+\pi^- p$ final states will be selected and the unpolarized differential cross sections will be obtained, complemented by measurements of the differential transverse-transverse and transverse-longitudinal interference cross sections, as well as induced and recoil hyperon polarizations. From these data the $\gamma_v p N^*$ electrocouplings will be determined for all possible new states with I=1/2 and I=3/2 and with all possible J^P quantum numbers, and the Q^2 evolution of their helicity amplitudes will then be determined in the low Q^2 range ($Q^2 < 2$ GeV^2) for the different reaction channels.

The hybrid baryons will be identified as additional states in the N^* spectrum beyond the regular three-quark states. Since spin-parities of hybrid baryons are expected to be the same as those for regular three-quark states, the hybrid-baryon signature will emerge from the distinctively different low Q^2-evolution of its electrocouplings, due to the additional gluonic component in their wave function.

This kinematic range also corresponds to the region of the largest contributions from the meson-baryon cloud, allowing us to improve our knowledge on this component, which is relevant to understand the structure of all N^* states studied so far, as well as to explore the longitudinal N^* electroexcitations as the photon virtuality goes to zero. This program adds an important new physics component to the existing CLAS12 N^* program at 11 GeV, which aims to measure the transition form factors for all prominent N^* states up to $Q^2 < 12$ GeV^2, the highest photon virtualities ever probed in exclusive reactions. The study of the spectrum and structure of excited nucleon states at distance scales from low to high Q^2, encompassing the regime where low-energy meson-baryon degrees of freedom dominate to the regime where quark degrees of freedom dominate, creates new opportunities to better understand how the strong interaction of dressed quarks and gluons gives rise to the spectrum and structure of excited nucleon states and how these states emerge from QCD.

Contents

1 Introduction

The ongoing program at Jefferson Lab and several other laboratories to study excitation of nucleons in the so-called nucleon resonance region with real-photon and electron beams has been very successful. Although only a fraction of the photoproduction data taken during the CLAS g8, g9, g11, and g12 run groups has yet been analyzed and published, the available data have allowed for very significant advances in light-quark baryon spectroscopy, and have led to strong evidence for several new nucleon excitations as documented in the PDG review of 2014 [1]. These discoveries were possible due to the very high meson production rates recently obtained for energy-tagged photoproduction processes. Furthermore, the use of meson electroproduction has led to completely new insights into the nature of several prominent baryon resonances, such as the $N(1440)\frac{1}{2}^+$ Roper resonance. For a long time this state defied an explanation of its properties, such as its mass, transition amplitudes, and transition form factors, within the constituent quark model (CQM). The analyses of the new electroproduction data from CLAS were crucial in dissecting its complex structure and providing a qualitative and quantitative explanation of the space-time evolution of the state [2]. The Roper was also considered as a candidate for the lowest mass hybrid baryon [3]. It was only due to the meson electroproduction data that this possibility could be dismissed [4, 5].

The theory of the strong interaction, QCD, not only allows for the existence of baryons with dominant gluonic contributions (hybrid baryons), but Lattice QCD calculations have now also predicted several baryon states with a dominant gluonic admixture to the wave function, and with the lowest mass hybrids approximately 1.3 GeV above the nucleon ground state [6], i.e. in the range of $W = 2.2$ GeV to 2.5 GeV. In the meson sector, exotic states (hybrid mesons) are predicted with quantum numbers that cannot be obtained in a pure $q\bar{q}$ configuration. The selection of mesons with such exotic quantum numbers provides a convenient way to identify candidates for gluonic mesons. In contrast to the meson sector, hybrid baryons have quantum numbers that are also populated by ordinary three-quark states. Hybrid baryons hence mix with these three-quark excited states or with dynamically generated states making the identification of gluonic baryons more difficult. An important question immediately arises, how we can distinguish gluonic excitations of baryons from their ordinary quark excitations?

Mapping out the nucleon spectrum and the excitation strengths of individual resonances is a powerful way to answer a central question of hadron physics: "What are the effective degrees of freedom as the excited states are probed at different distance scales?". Previous analyses of meson electroproduction have shown to be most effective in providing answers for several excited states including: $\Delta(1232)\frac{3}{2}^+$, $N(1440)\frac{1}{2}^+$, $N(1520)\frac{3}{2}^-$, $N(1535)\frac{1}{2}^-$, $\Delta(1620)\frac{1}{2}^-$, $N(1680)\frac{5}{2}^+$, $N(1675)\frac{5}{2}^-$, and $N(1710)\frac{1}{2}^+$ [7, 8, 9, 10].

The experimental program outlined in this proposal is meant to vastly improve upon the available information and to extend the reach of meson electroproduction to cover the nucleon resonance mass range up to 3 GeV and an extended low Q^2 range from 0.05 GeV^2 to 2 GeV^2, using electron beam energies of 6.6 GeV and 8.8 GeV. The unpolarized differential cross sections will be measured for the K^+Y and $\pi^+\pi^-p$ exclusive channels, complemented by measurements of the differential transverse-transverse and transverse-longitudinal interference cross sections, along with other polarization observables.

From these data the $\gamma_v pN^*$ electrocouplings will be determined employing the well known unitary isobar models and dispersion relation approaches that have proven very effective for the study of two-body final states such as πN [4, 11] and KY [12], as well as the JLab-Moscow (JM) meson-baryon reaction model for $\pi^+\pi^- p$ electroproduction [11, 13], the multi-channel partial wave techniques employing either the Bonn-Gatchina [14] or GWU [15] approaches, and approaches starting from the Veneziano model and Regge phenomenology [16] that are applicable at higher energies, where many hadron channels open in the final state interactions.

The proposed experimental program will search for all possible new states with isospin I=1/2 and I=3/2 and with all possible J^P quantum numbers. As new states are identified using the high event rates at very small Q^2 values ("quasi-real" photoproduction), the Q^2 dependence of their helicity amplitudes will be determined. The results at different values of Q^2 in the different exclusive channels will substantially enhance the discovery potential for new baryon states. Consistent results on the resonance masses and the $\gamma_v pN^*$ electrocouplings from the different exclusive decay channels, as well as Q^2-independent partial hadronic decay widths over the full Q^2 range, will offer convincing evidence for the existence of new states and the reliable extraction of their parameters. This approach has been highly effective in determining the Q^2 dependence of the $A_{1/2}$, $A_{3/2}$, and $S_{1/2}$ helicity amplitudes for several lower mass baryons, such as the $\Delta(1232)\frac{3}{2}^+$, $N(1440)\frac{1}{2}^+$, and $N(1535)\frac{1}{2}^-$ [4, 7]. These and many other results are included in the review of the N^* and Δ^* states in the latest edition of the PDG [17].

The hybrid baryons will be identified as additional states in the N^* spectrum beyond the regular three-quark states as has been predicted in recent LQCD studies of the baryon spectrum [6]. Since spin-parities of hybrid baryons are expected to be the same as those for regular three-quark states, information on the $\gamma_v pN^*$ electrocoupling evolution with Q^2 becomes critical in the search for hybrid baryons. A distinctively different Q^2 evolution of the hybrid-baryon electrocouplings is expected considering the different color-multiplet assignments for the quark-core in a regular versus a hybrid baryon, i.e. color singlet versus octet, which also calls for low photon virtualities as the preferential regime for studies of the hybrid-baryon electrocouplings. In conjunction with experiment E12-09-003 [18], which focuses on the highest Q^2, as well as E12-06-108A [19], which explores KY production, the proposed experiment will complement the existing program of nucleon resonance electroexcitation.

2 Theoretical Studies of Hybrid Baryons

2.1 Model Projections

In an extension of the MIT bag model, gluonic excitations of the nucleon, to states where a constituent gluon in the lowest energy transverse electric mode combines with three quarks in a color octet state to form a colorless state in the mass range of 1.600 ± 0.100 GeV, have been broadly discussed since 1983 [3].

The gluon flux-tube model applied to hybrid baryons [20, 21] came up with similar quantum numbers of the hybrid states, but predicted considerably higher masses than the bag model. For the lowest mass flux-tube hybrid baryon a mass of 1.870 ± 0.100 GeV was found. In all cases the lowest mass hybrid baryon was predicted as a $J^P = 1/2^+$

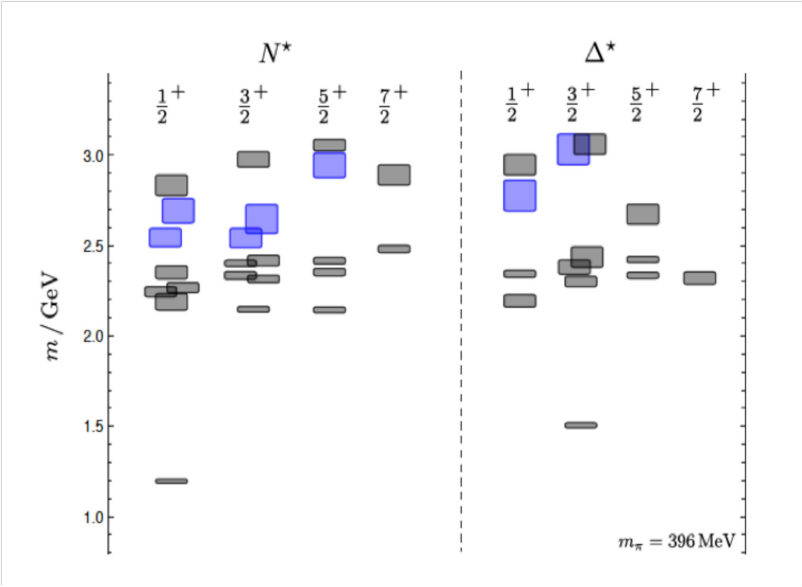

Figure 1: The light-quark baryon spectrum predicted in Lattice QCD at a pion mass of 396 MeV [6]. The blue shaded boxes indicate states with dominant gluonic contributions. Note that both the mass of the nucleon ground state and of the $\Delta(1232)$ are shifted by nearly 300 MeV to higher masses.

state, i.e. a nucleon- or Roper-like state. Hybrid baryons were also discussed in the large N_c approximation of QCD for heavy quarks [22], which also led to the justification of the constituent glue picture used in the models. The high energy behavior of hybrid baryons was discussed in Ref. [23]. However, in contrast to hybrid meson production, which has received great attention both in theory and in experiments, the perceived difficulties of isolating hybrid baryon states from ordinary quark states led this part of the field to remain dormant for several years.

2.2 Lattice QCD Predictions

The first quenched calculations on the lattice came in 2003 [24], when the lowest gluonic three-quark hybrid system was projected at a mass of 1 GeV above the nucleon mass, placing the lowest hybrid baryon at a mass of ∼2 GeV. The first LQCD calculation of the full light-quark baryon spectrum with unquenched quarks that occurred in 2012 included the projections of the hybrid isospin-1/2 N_G states and isospin-3/2 Δ_G states [6]. Fig. 1 shows the projected light quark baryon spectrum in the lower mass range.

At the pion mass of 396 MeV used in this projection, the prediction for the nucleon mass is shifted by nearly 300 MeV to higher masses. In the following we take this shift into account by subtracting 300 MeV from the masses of the excited states shown in Fig. 1. As stated in Ref. [6], the lowest hybrid baryons, shown in Fig. 1 in blue, were identified as states with leading gluonic contributions. If hybrid baryons are not too wide, we might expect the lowest hybrid baryon to occur at masses of about 1.3 GeV above the ground state, i.e. in a mass range of 2.2 GeV to 2.5 GeV, and a few hundred MeV above the band of radially excited $J^P = \frac{1}{2}^+$ three-quark nucleon excitations of isospin 1/2, and thus possibly well separated

from other states.

In this computation the lowest $J^P = \frac{3}{2}^+$ gluonic states are nearly mass degenerate with the corresponding $J^P = \frac{1}{2}^+$ gluonic states, generating a glue-rich mass range of hybrid nucleons. If these projections hold up with LQCD calculations using near physical pion masses, one should expect a band of the lowest mass hybrid baryon states with spin-parity $\frac{1}{2}^+$ and $\frac{3}{2}^+$ to populate a relatively narrow mass band of 2.2 GeV to 2.5 GeV. Note, that these states fall into a mass range where no three-quark nucleon excitations are predicted to exist in these calculations. The corresponding negative parity hybrid states, which are expected to occur at much higher masses, are not included in Fig. 1, and are not further considered here. However, they may be the subject of analysis should they appear within the kinematic range covered by this proposal.

2.3 Hadronic Couplings

Very little is known about possible hadronic couplings of hybrid baryons B_G. One might expect an important role for final states with significant gluonic admixtures, e.g. $B_G \to N\eta'$ [25], or final states containing $s\bar{s}$ contributions due to the coupling $G \to s\bar{s}$, e.g. $B_G \to K^+\Lambda$, $B_G \to N^*(1535)\pi \to N\eta\pi$, $B_G \to N\pi\pi$, $B_G \to \phi(1020)N$, and $B_G \to K^*\Lambda$. Quark-model estimates of the hadronic couplings would be helpful in selecting the most promising final states for the experimental evaluation. As long as such estimates are not available we will use a range of assumptions on the hadronic couplings to estimate the sensitivity required for definitive measurements. Assuming hadronic couplings of a few percent in the less complex final states, e.g. $K^+\Lambda$, $K^*\Lambda$, or $N\pi\pi$, we should be able to identify these states and proceed to experimentally establish their electromagnetic couplings and Q^2 dependences. We focus in this proposal on measurements of those decay channels that have already been successfully analyzed from CLAS data and that will be further investigated in data from CLAS12, i.e. $K^+\Lambda$, $K^+\Sigma^0$ and $\pi^+\pi^-p$. These studies can be extended by the exploration of other electroproduction channels such as $\phi(1020)N$ or $K^*\Lambda$.

2.4 Electromagnetic Couplings

The study of excited nucleon state electrocouplings in a wide range of photon virtualities is a proven effective tool for establishing the active degrees of freedom that contribute to the N^* structure at different distance scales [4, 7, 26, 27, 28]. The information on the $\gamma_v NN^*$ electrocoupling evolution with Q^2 becomes critical in the search for hybrid baryons. A distinctively different Q^2 evolution of the hybrid-baryon electrocouplings is expected considering the different color-multiplet assignments for the quark-core in a regular versus a hybrid baryon, i.e. color singlet versus octet. Electromagnetic couplings have been studied within a non-relativistic constituent quark-gluon model, but only for two possible hybrid states, the Roper $N_G(1440)\frac{1}{2}^+$ and the $\Delta_G(1600)\frac{3}{2}^+$. In Ref. [29] the photoexcitation of the hybrid Roper resonance $N(1440)\frac{1}{2}^+$ was studied, and in Ref. [30] the electroproduction transition form factors of a hybrid Roper state were evaluated. The latter was essential in eliminating the Roper resonance as a candidate for a hybrid state, both due to the Q^2 dependence of its transverse helicity amplitude and the prediction of $S_{1/2}(Q^2) = 0$ at all Q^2 (see Fig. 2). It also showed that the hybrid Roper $A_{1/2}$ transition amplitude should behave like $A_{1/2}$ for the

ordinary $\Delta(1232)$. Clearly the $S_{1/2}$ amplitude behaves differently and $A_{3/2}$ does not exist for the Roper. Both amplitudes exhibit a Q^2 dependence that is distinctively different from the hybrid baryon prediction, especially the scalar amplitude $S_{1/2}(Q^2)$ which was found to be large, while it is predicted to be suppressed in leading order for the lowest mass $\frac{1}{2}^+$ hybrid state.

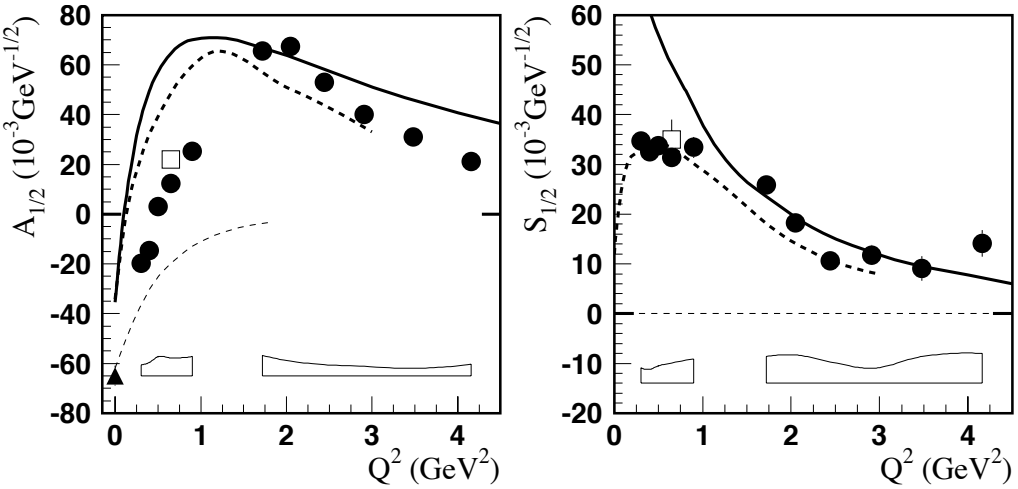

Figure 2: Electrocoupling amplitudes of the Roper resonance $N(1440)\frac{1}{2}^+$ [5]. The thin dashed lines are the constituent quark-glue model predictions for the gluonic Roper [25].

The aforementioned predictions should apply to each lowest mass hybrid state with $J^P = \frac{1}{2}^+$ and $\frac{3}{2}^+$. One may ask about the model-dependence of this prediction. The transverse amplitude has model sensitivity in its Q^2 dependence and it depends on the model ingredients, however, there are no ordinary three-quark model predictions that would come even close to the predictions of the hybrid quark-gluon model. The radial excitation of the Roper resonance gives a qualitatively different prediction for $A_{1/2}(Q^2)$ compared to the hybrid excitation, where the three-quark component remains in the ground state with only a spin-flip occurring (just as for the $N \rightarrow \Delta(1232)$ transition). The suppression of the longitudinal coupling, which is a property of the γqG vertex, is largely independent of specific model assumptions.

The $\Delta(1600)\frac{3}{2}^+$ was the other state considered as a hybrid candidate, specifically for the lowest mass gluonic Δ_G. A result similar to that for the hybrid Roper is found in Ref. [30] for a hybrid $\Delta_G(1600)\frac{3}{2}^+$, i.e. a fast falling $A_{1/2}(Q^2)$ and $S_{1/2}(Q^2) \approx 0$. The amplitudes at the photon point are not inconsistent with the ordinary three-quark model calculation but are inconsistent with the hybrid baryon hypothesis. On the other hand this result is also in line with the expectation that the lowest mass hybrid states should have considerably higher masses than the first radially excited quark states. Note that there are currently no experimental results for the Q^2 dependence of the $A_{1/2}$ and $S_{1/2}$ amplitudes of this state.

Based on constituent counting rules [31], we expect that the electrocouplings of hybrid baryons should decrease faster with increasing photon virtuality Q^2 than for regular three-quark nucleon resonances because of the extra constituent. Therefore, low photon virtualities are the preferential region to study hybrid baryons and we are proposing to explore the $Q^2 < 2.0$ GeV^2 range with a particular focus on the hybrid baryon search at $Q^2 < 1.0$ GeV^2.

In order to identify hybrid baryons, we are looking to map out their electrocoupling behavior, which should have distinctively different features in comparison with already established states from the CLAS results [7]. Electrocouplings of three-quark resonances for $J^P = \frac{1}{2}^+$ are shown in Figs. 2 and 3 and for $J^P = \frac{3}{2}^+$ in Figs. 4, 5, and 6. If hybrid baryons will be established in the proposed experiment, further studies of their electrocouplings can be extended towards higher photon virtualities from the data of the approved CLAS12 experiments [18, 19].

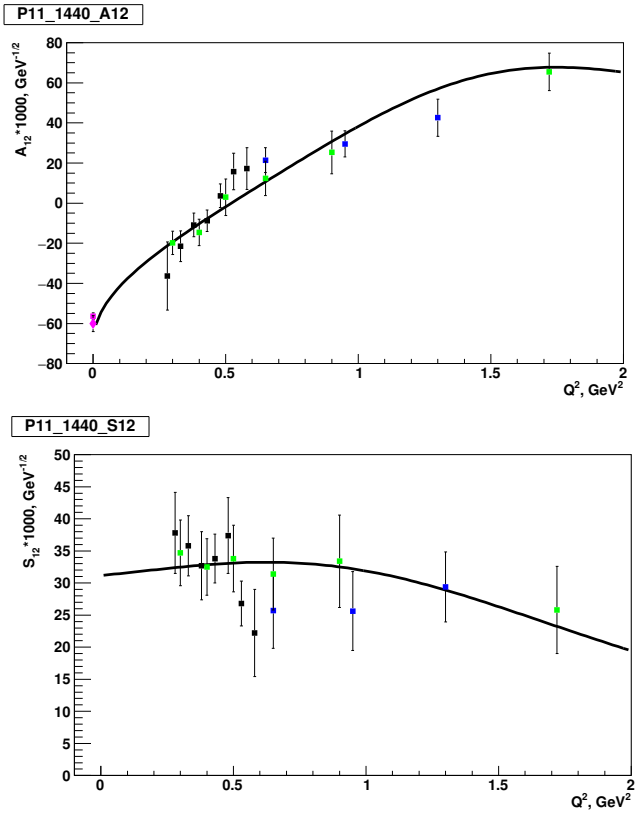

Figure 3: Electrocouplings of the $N(1440)\frac{1}{2}^+$ from the CLAS data on $N\pi$ (green circles) [5] and $\pi^+\pi^- p$ [13, 28] (black and blue squares) exclusive electroproduction off the proton. The results at the photon point are taken from Refs. [1, 32].

3 Strategies for Identifying New Baryon States

Advanced studies of the data for exclusive meson photoproduction off the proton carried out within the framework of the global multi-channel amplitude analysis developed by the Bonn-Gatchina group [35, 36, 37] have revealed many new baryon states in the mass range from 1.7 GeV to 2.5 GeV. These states were included in the PDG [1] with statuses from one to three stars. Notably, the most prominent signals for new states came from analyses of the CLAS [38, 39, 40, 41], ELSA [42], MAMI [43] and GRAAL [44, 45] data on KY photoproduction. However, studies of the KY as well as the $\pi^+\pi^- p$ exclusive electroproduction channels considerably extend our understanding of the excited nucleon state spectrum, including both regular three-quark and exotic hybrid states.

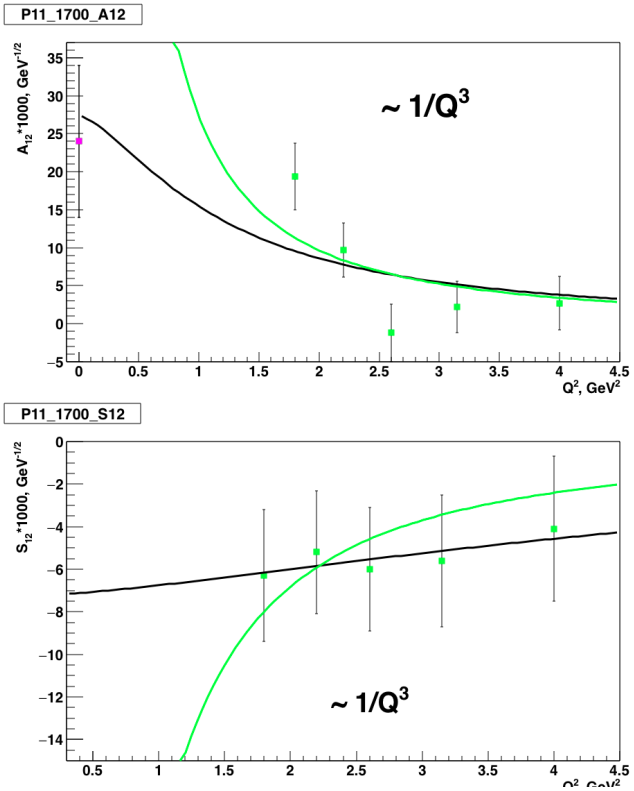

Figure 4: Electrocouplings of the $N(1720)\frac{3}{2}^+$ from the CLAS data on $\pi^+\pi^- p$ [33] exclusive electroproduction off the proton [34]. The results at the photon point are taken from Refs. [32, 33].

The new baryon states, if they are excited in the s-channel should be seen in exclusive reactions both with real and virtual photons in the same final states. Furthermore, their masses, total decay widths, and partial decay widths to different final states, should be Q^2 independent. The values of the $\gamma_v pN^*$ electrocouplings obtained independently from analyses of different exclusive channels with completely different non-resonant contributions should be the same. Consistent results over the full covered Q^2 range on resonance masses, $\gamma_v pN^*$ electrocouplings for all exclusive decay channels under study, and Q^2-independent partial hadronic decay widths, will offer convincing evidence for the existence of new states. These studies offer a model-independent way to prove not only the existence of new excited nucleon states, but also their nature as s-channel resonances, eliminating alternative interpretations for the structures observed in the kinematic dependencies of the observables as complex coupled-channel effects, dynamical singularities for the non-resonant amplitudes, kinematic reflections, etc.

The studies of the exclusive KY and $\pi^+\pi^- p$ electroproduction channels at $Q^2 < 2.0$ GeV^2 with the highest virtual photon flux ever achieved in exclusive electroproduction will allow us to solidify the results on the spectrum of excited nucleon states, confirming or ruling out the signal of "missing" resonances observed in exclusive photoproduction. Furthermore, for the first time the information on the $\gamma_v pN^*$ electrocouplings of new baryon states will become available, offering access to the structure of "missing" resonances and elucidating

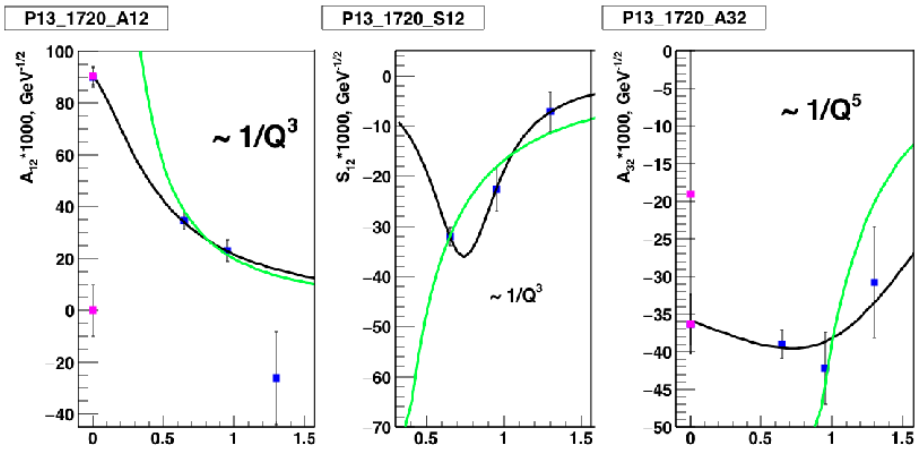

Figure 5: Electrocouplings of the $N(1720)\frac{3}{2}^+$ $A_{1/2}$ (left), $S_{1/2}$ (middle), and $A_{3/2}$ (right) from the CLAS data on $\pi^+\pi^- p$ [33] exclusive electroproduction off the proton [34]. The results at the photon point are taken from Refs. [32, 33].

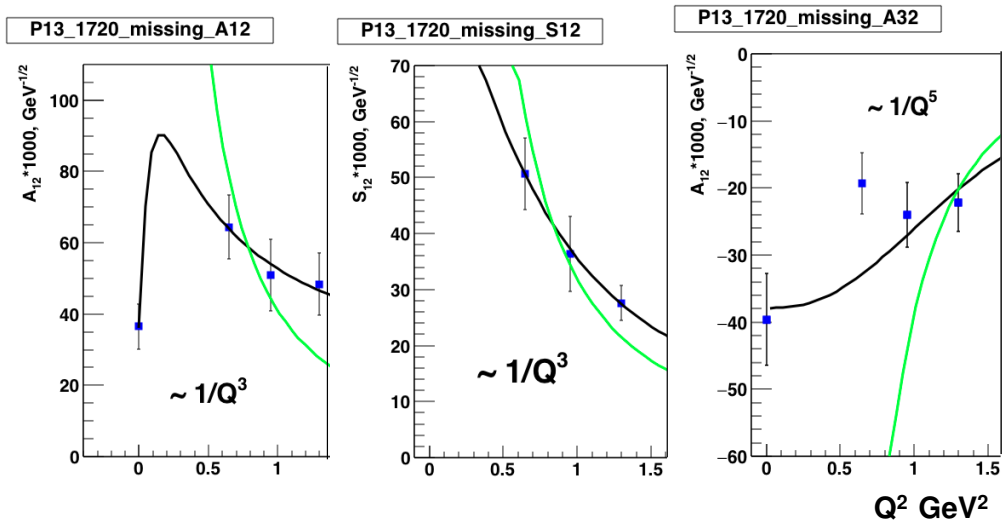

Figure 6: Electrocouplings of the $N'(1720)\frac{3}{2}^+$ $A_{1/2}$ (left), $S_{1/2}$ (middle), and $A_{3/2}$ (right) electrocouplings from the CLAS data on $\pi^+\pi^- p$ [33] exclusive electroproduction off the proton [34]. The results at the photon point are taken from Refs. [32, 33].

any differences from the conventional resonances. Finally, in this general introduction to our strategies for identifying new baryon states, we want to note that studies of the two major exclusive $N\pi$ and $\pi^+\pi^- p$ electroproduction channels with CLAS have revealed the relative growth of the resonant contributions with Q^2 in both channels. Therefore the use of the high-intensity virtual photon fluxes in the proposed experiment is preferential for a new baryon state search in comparison to photoproduction. It still remains to be seen which range of photon virtualities is the most suitable for the discovery of new excited nucleon states.

In this section we address the question of how gluonic hybrid baryons are distinct from ordinary three quark baryon excitations and we will also elucidate additional opportunities offered by studies of exclusive electroproduction processes at different photon virtualities for the search of new baryon states, both hybrid baryons and regular three-quark states.

3.1 Search for Hybrid Baryon States

As discussed in Section 2.2 the lowest hybrid baryons should have isospin $I = \frac{1}{2}$ and $J^P = \frac{1}{2}^+$ or $J^P = \frac{3}{2}^+$. Their masses should be in the range from 2.2 GeV to 2.5 GeV. This mass range will be further refined once LQCD calculations with physical pion masses become available, since masses may shift toward lower values with more realistic pion masses. Four regular states with $I = \frac{1}{2}$ and $J^P = \frac{1}{2}^+$ are predicted with dominant three-quark contributions and with masses below the mass of the lowest LQCD hybrid states. Of these four states two are the well known $N(1440)\frac{1}{2}^+$ and $N(1710)\frac{1}{2}^+$, and two are the less well established $N(1880)\frac{1}{2}^+$ and $N(2100)\frac{1}{2}^+$ with 2^* and 1^* ratings, respectively. Another state, the $N(2300)$, has a 2^* rating and falls right into the lowest hybrid mass band predicted by LQCD. This state, if confirmed, could be a candidate for the predicted lowest mass LQCD hybrid state.

In order to address this question, it is necessary to confirm (or refute) the existence of the 2^* state $N(1880)$ and of the 1^* state $N(2100)$, and to measure the electromagnetic couplings of the $N(2300)$ and their Q^2 dependences. Improved information on the lower mass states should become available in the next one or two years when the new high-statistics single- and double-polarization data from CLAS have been fully included into the multi-channel analysis frameworks such as the Bonn-Gatchina and the Jülich/GWU approaches. Should these two states be confirmed, then any new nucleon state with $J^P = \frac{1}{2}^+$, which happens to be in the right mass range, should be a candidate for the lowest mass hybrid baryon. Another $N(2300)\frac{1}{2}^+$ state has only been seen at BES III in the invariant mass $M(p\pi^0)$ of $\Psi(2S) \to p\bar{p}\pi^0$ events [46]. In this case the production of the $N(2300)$ occurs at very short distances as it emerges from heavy quark flavor $c\bar{c}$ decay. Hence this state may even be observed in single pion electroproduction $ep \to e'\pi^+ n$ and $ep \to e'p'\pi^0$ if it couples to photons with sufficient strength to be measurable.

In the $J^P = \frac{3}{2}^+$ sector the situation is more involved. There are two hybrid states predicted in the mass range 2.2 GeV to 2.4 GeV, with masses above five quark model states at the same J^P. Of the five states, two are the well known 4^* and 3^* states, the $N(1720)\frac{3}{2}^+$ and the $N(1900)\frac{3}{2}^+$, respectively, and one state, the $N(2040)\frac{3}{2}^+$, has a 1^* rating. Here we will have to confirm (or refute) the 1^* star state and find two or three (if the $N(2040)$ does not exist) more quark model states with the same quantum numbers in the mass range 1.7 GeV to 2.1 GeV. There is one candidate $\frac{3}{2}^+$ state near 1.72 GeV seen in $p\pi^+\pi^-$ electroproduction

[47], whose status will be pinned down with the expected very high statistics data.

Possible signatures of the lowest mass hybrid baryons are:

- Resonance masses in the range of 2.2 GeV $< W <$ 2.5 GeV with $I = \frac{1}{2}$, $J^P = \frac{1}{2}^+$ or $J^P = \frac{3}{2}^+$, and almost degenerate masses where no regular three-quark states are observed
- Q^2 dependence of the $A_{1/2}(Q^2)$ transverse helicity amplitude similar to that for the $\Delta(1232)\frac{3}{2}^+$ but different from the three-quark excited states with the same J^P, and
- A strongly suppressed helicity amplitude $S_{1/2}(Q^2) \approx 0$ in comparison to other ordinary three-quark states or meson-baryon excitations.

This list of expected hybrid signatures may provide some initial guidance when examining new baryon states for possible large gluonic components. However, they are not sufficient to firmly establish the hybrid nature of a state. To achieve this goal, improved modeling of other degrees-of-freedom, such as meson-baryon contributions and direct calculations of electrocouplings from LQCD, will be needed. The expected high statistics data will be used to identify any new or poorly known state, whether or not it is a candidate for a hybrid baryon state. This will aid in the identification of the effective degrees of freedom underlying the resonance excitation of all states that couple to virtual photons.

3.2 Known and New Three-Quark Baryon States

Besides the search for hybrid baryon states, there are many open issues in our knowledge of the structure of ordinary baryon excitations that can be addressed with the data taken in parallel from the proposed experiment. As an example we show in Fig. 7 the electrocouplings of the $N(1680)\frac{5}{2}^+$ resonance [48], the strongest state in the third nucleon resonance region. With the exception of the real photon point, the data are quite sparse for $Q^2 \leq 1.8$ GeV^2 and the high statistics data expected from this experiment would remedy the lack of experimental information and address similar situations for other states as well. Note that the high-Q^2 part will be covered by the approved JLab experiment E12-09-003 [18].

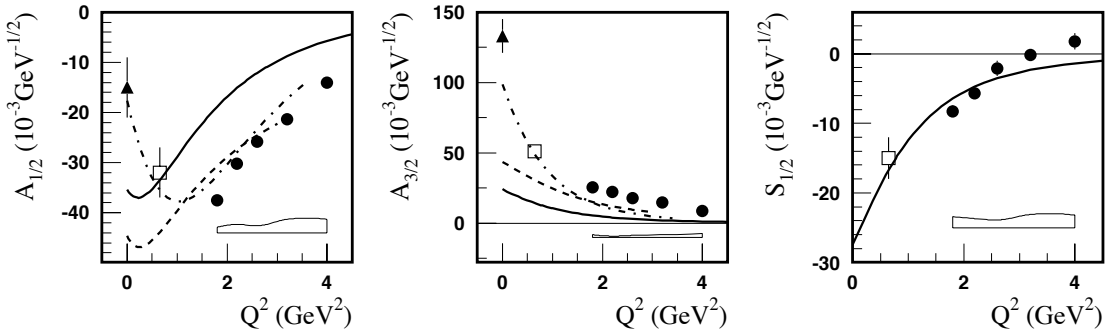

Figure 7: Electrocoupling amplitudes $A_{1/2}$ (left), $A_{3/2}$ (middle), and $S_{1/2}$ (right) of the $N(1680)\frac{5}{2}^+$ resonance [48].

An even more compelling example is the $N(1675)\frac{5}{2}^-$ state, where data at $Q^2 > 1.8$ GeV^2 have been published recently by the CLAS Collaboration [48]. Fig. 8 shows the measured helicity amplitudes. Low Q^2 data are very important here, as for this state the quark transitions are strongly suppressed by the Moorhouse selection rule, and therefore, any non-zero value of the electrocoupling amplitudes will directly measure the strength of the meson-baryon contributions. The main data needed are single pion production $ep \to e'\pi^+ n$ and $ep \to e'\pi^0 p$. These processes can be accumulated with sufficiently high event rates, even with a pre-scale factor of 10 on the Forward Tagger, should the overall event rate be too high in this two-prong topology.

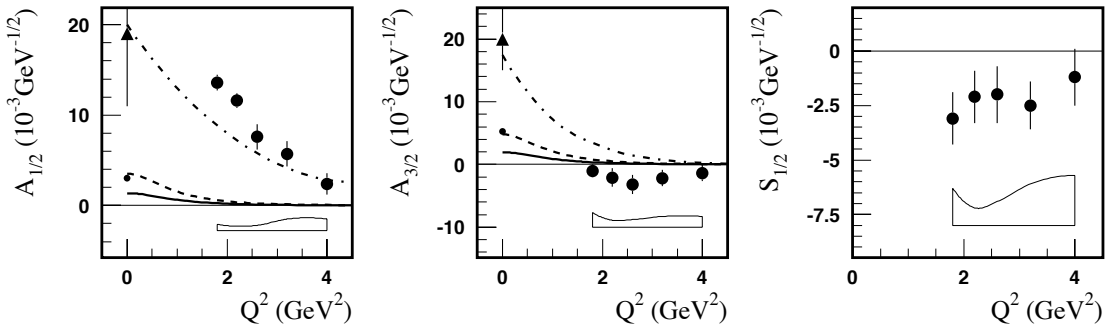

Figure 8: Electrocoupling amplitudes $A_{1/2}$ (left), $A_{3/2}$ (middle), and $S_{1/2}$ (right) of the $N(1675)\frac{5}{2}^-$ resonance [48]. Quark models predict the transverse amplitudes to be suppressed. The significant deviation of the $A_{1/2}$ amplitude from zero is consistent with meson-baryon contributions to the excitation strength (dashed-dotted lines).

The recent combined analysis [33] of the CLAS $\pi^+\pi^- p$ photoproduction [49] and electroproduction [47] data revealed further convincing evidence for a new $N'(1720)\frac{3}{2}^+$ baryon state. This state has the same spin-parity and almost the same mass and total decay width as the conventional $N(1720)\frac{3}{2}^+$, but a distinctively different Q^2 evolution of the resonance electrocouplings (see Figs. 5 and 6) and partial hadronic decay widths to the $\pi\Delta$ and ρp final states. The electrocouplings of the new $N'(1720)\frac{3}{2}^+$ state are available at the photon point and in the limited Q^2 range from 0.5 GeV^2 to 1.5 GeV^2. As shown in Figs. 5 and 6, the $A_{1/2}(Q^2)$ electrocouplings of the $N(1720)\frac{3}{2}^+$ and $N'(1720)\frac{3}{2}^+$ states evolve for $Q^2 < 0.5$ GeV^2 in a completely different manner. The $A_{1/2}(Q^2)$ amplitude of the conventional $N(1720)\frac{3}{2}^+$ baryon state decreases with Q^2, while it increases for the new $N'(1720)\frac{3}{2}^+$ state in the range of $Q^2 < 0.5$ GeV^2. Therefore, the future results on the $N(1720)\frac{3}{2}^+$ and $N'(1720)\frac{3}{2}^+$ state electrocouplings from the data on exclusive $\pi^+\pi^- p$ electroproduction off the proton at small Q^2 will shed light on the differences in the structure of the conventional and the "missing" baryon states.

In general, the studies of resonance electrocouplings at small photon virtualities in the proposed experiment will, for the first time, allow us to explore their Q^2 evolution at distance scales where the meson-baryon cloud contributions are expected to be largest, offering preferential conditions for exploration of this component of N^* structure. Recent advances in the studies of nucleon structure using QCD-based Dyson-Schwinger equations have provided strong indications that quark-gluon confinement in the real-world is a dynamical process

and point to an intimate connection between confinement and Dynamical Chiral Symmetry Breaking (DCSB) [50, 51]. Moreover, in providing a clear explanation of the dichotomous nature of pions, as both bound-states of massive constituents and Nambu-Goldstone bosons, these studies force a realization that baryons constituted from fully-dressed confined-quarks must also be surrounded by a complex meson-baryon cloud, generated by a sequence of meson-baryon final-state interactions. A detailed understanding of the interplay between the dressed-quark core in a diverse array of nucleon excited states and the associated meson-baryon clouds is crucial to developing a quantitative picture of the dynamical confinement mechanism; and this requires a systematic investigation of resonance electrocouplings at low virtuality. The studies proposed herein will therefore address a critical open problem in hadron physics; namely, exposing those features of the hadronization process which control the transition from the quark-gluon color-confinement regime to the asymptotic domain of strong interactions between color-neutral mesons and baryons.

3.3 Amplitude Analyses in the Search for New Baryon States

In our studies of the experimental data we will start from the extraction of the resonance parameters from the independent analyses of the KY and $\pi^+\pi^-p$ final states carried out within the framework of the reaction models for the description of these exclusive channels. Eventually we will employ the amplitude analysis methods for the resonance search and extract the resonance parameters in a global fit of all exclusive channels studied with CLAS12. Consistent results on the resonant parameters determined from independent analyses of different exclusive meson electroproduction channels and extracted from a global multi-channel fit of all available data will offer strong and almost model independent evidence for the existence of any new states and the reliable extraction of their parameters. Note, that in order to apply the coupled-channel approaches to the analyses of KY and $\pi^+\pi^-p$ exclusive electroproduction data, information on $N\pi$ electroproduction is also needed. The $N\pi$ exclusive channels dominate at $W < 1.6$ GeV. These cross sections remain much larger in comparison with the KY channels over our entire kinematics area. The events from the $N\pi$ exclusive channels will be collected simultaneously in CLAS12 with those for the KY and $\pi^+\pi^-p$ channels.

The advanced amplitude analysis approach for extraction of the nucleon resonance parameters from the global analysis of the photoproduction data, which includes almost all relevant exclusive γp meson production channels in the nucleon resonance region, has been developed by the Bonn-Gatchina group [35, 36, 37]. In this approach, the production amplitudes are decomposed over the set of partial waves. The partial wave amplitudes are parameterized fully accounting for the restrictions imposed by the general unitarity and analyticity conditions, employing the K- and D-matrix approaches for the final hadron rescattering, while for the photoproduction amplitudes, the P-vector approach is used. In the case of pronounced t-channel contributions, Reggeized t-exchanges are incorporated into the photoproduction amplitudes. The resonance parameters were determined from the global fit of all available exclusive photoproduction data augmented by the fit of the final state hadroproduction. Application of the Bonn-Gatchina approach to the global analysis of the dominant part of the exclusive meson photoproduction data measured with CLAS and elsewhere has provided information on masses, widths, photocouplings, and hadronic decay

parameters for most excited nucleon states in the mass range up to 3 GeV. These analyses have revealed evidence for ∼10 new baryon states, reported in the PDG [1] with status from one to three stars (see Fig. 9).

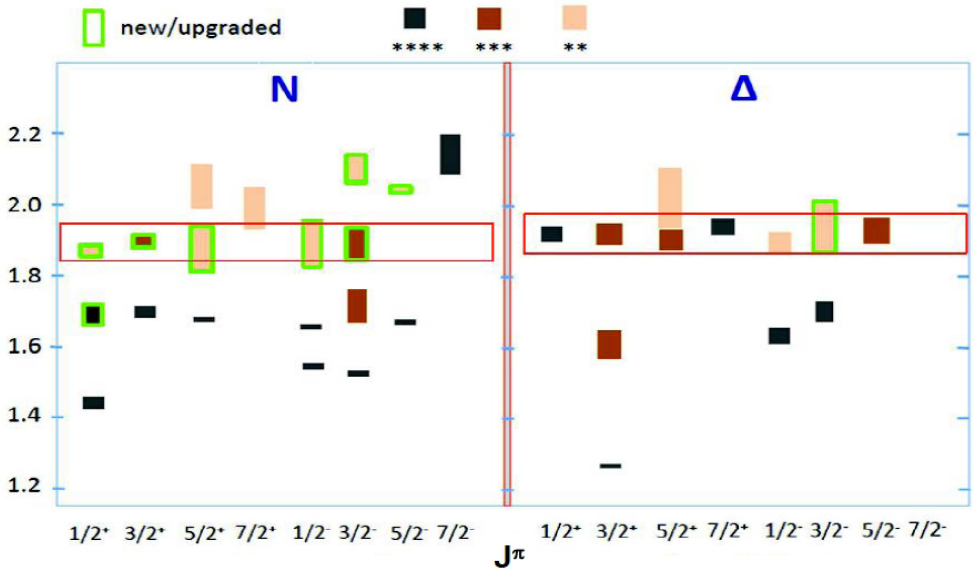

Figure 9: Recent results on the spectrum of excited nucleon states [1]. Signals from the states shown in the green boxes were observed in a global multi-channel analysis of exclusive meson photoproduction data carried out within the framework of the Bonn-Gatchina approach [35, 36, 37].

An extension of this approach for the description of the exclusive electroproduction channels represents a future commitment of the Bonn-Gatchina group [52]. The Bonn-Gatchina approach extended for the analysis of the exclusive electroproduction channels will be used for the extraction of the resonance parameters and the search for new baryon states in the proposed experiment. This extension will be vital in order to check the signals from new baryon states observed in the exclusive meson photoproduction independently in the exclusive electroproduction processes, confirming or rejecting the candidate states.

An advanced dynamical coupled-channel (DCC) model has been developed by the Argonne-Osaka Collaboration for the combined analysis of the world data for $\pi N, \gamma N \to \pi N$, ηN, $K\Lambda$, $K\Sigma$, and $N\pi\pi$ photo-, electro-, and hadroproduction with a goal of extracting resonance parameters [53, 54]. The DCC approach incorporates tree level diagrams derived from an effective Lagrangian for the resonant and non-resonant contributions to photo- and electroproduction, as well as to the final state hadronic interactions. The amplitudes for all exclusive channels are fully consistent with the restrictions imposed by the general unitarity and analyticity conditions. This is the only coupled-channel approach capable of describing the $N\pi\pi$ data in accord with the general unitarity condition. In order to fulfill the unitarity restrictions, the meson-baryon interactions present in the non-resonant amplitudes of the included exclusive channels are incorporated into the electromagnetic and hadronic vertices of nucleon resonances, together with the direct resonance decays to the $\gamma_{r,v}p$ and meson-baryon final states. The former generate the so-called meson-baryon cloud contributions to the bare verticies for the resonance electromagnetic and/or hadronic decays. Analysis of

the observables within the framework of the DCC approach allows us not only to extract the fully dressed resonance electromagnetic and hadronic decay amplitudes, but also to disentangle the contributions from the meson-baryon cloud and the bare vertices associated with the quark core in the nucleon resonance structure. In this way, the DCC approach is capable of providing valuable insight into the structure of excited nucleon states. The DCC model currently is the only available coupled-channel approach that has provided results on the structure of excited nucleon states from analysis of the CLAS $N\pi$ electroproduction data [5], including the $N \to \Delta(1232)\frac{3}{2}^+$ transition form factors at Q^2 up to 7 GeV^2 [7] and the $N(1440)\frac{1}{2}^+$ electrocouplings at Q^2 up to 3 GeV^2 [55].

The Argonne-Osaka DCC model will be employed in the analysis of the data of the proposed experiment with the goal to observe manifestations of the new excited nucleon states and to extract the $\gamma_v pN^*$ electrocouplings of the established and new baryon states. This model will allow us to fully account for the impact of the final state interactions in the extraction of the $\gamma_v pN^*$ electrocouplings from the KY channels with the $N\pi$, and $N\pi\pi$ open channels for which the electroproduction cross sections are much larger.

The $N\pi$ data have been analyzed within the framework of two conceptually different approaches: a unitary isobar model (UIM) and dispersion relations (DR) [5, 48]. The UIM describes the $N\pi$ electroproduction amplitudes as a superposition of N^* electroexcitations in the s-channel, non-resonant Born terms, and ρ and ω t-channel contributions. The latter are Reggeized, which allows for a better description of the data in the second- and third-resonance regions. The final-state interactions are treated as πN rescattering in the K-matrix approximation [5]. In the DR approach, the dispersion relations relate the real to the imaginary parts of the invariant amplitudes that describe the $N\pi$ electroproduction. Both approaches provide a good and consistent description of the $N\pi$ data in the range of $W < 1.7$ GeV and $Q^2 < 5.0$ GeV^2, resulting in $\chi^2/d.p. < 2.9$. In this proposal, this approach will be used for the evaluation of the $N\pi$ electroproduction amplitudes needed as the input for the aforementioned global multi-channel analyses of the KY and $\pi^+\pi^- p$ exclusive electroproduction data.

The $\pi^+\pi^- p$ electroproduction data from CLAS [34, 56] provide for the first information on nine independent single-differential and fully-integrated cross sections binned in W and Q^2 in the mass range $W < 2.0$ GeV and at photon virtualities of 0.25 GeV$^2 < Q^2 < 1.5$ GeV^2. The analysis of the data have allowed us to develop the JM reaction model [11, 13, 28] with the goal of extracting the resonance electrocouplings, as well as the $\pi\Delta$ and ρp hadronic decay widths. This model incorporates all relevant reaction mechanisms in the $\pi^+\pi^- p$ final-state channel that contribute significantly to the measured electroproduction cross sections off the proton in the resonance region, including the $\pi^-\Delta^{++}$, $\pi^+\Delta^0$, $\rho^0 p$, $\pi^+ N(1520)\frac{3}{2}^-$, $\pi^+ N(1685)\frac{5}{2}^+$, and $\pi^-\Delta(1620)\frac{3}{2}^+$ meson-baryon channels, as well as the direct production of the $\pi^+\pi^- p$ final state without formation of intermediate unstable hadrons. In collaboration with JPAC [57], a special approach has been developed allowing us to remove the contributions from the s-channel resonances to the Reggeized t-channel non-resonant terms in the $\pi^-\Delta^{++}$, $\pi^+\Delta^0$, and $\rho^0 p$ electroproduction amplitudes. The contributions from well established N^* states in the mass range up to 2 GeV were included into the amplitudes of the $\pi\Delta$ and ρp meson-baryon channels by employing a unitarized version of the Breit-Wigner ansatz [13]. The JM model provides a good description of the $\pi^+\pi^- p$ differential cross sections at $W < 1.8$ GeV and 0.2 GeV$^2 < Q^2 < 1.5$ GeV^2 with $\chi^2/d.p. < 3.0$. The

achieved quality of the CLAS data description suggests an unambiguous and credible separation between the resonant and non-resonant contributions [28]. The credible isolation of the resonant contributions makes it possible to determine the resonance electrocouplings and the $\pi\Delta$ and ρN decay widths from the resonant contributions employing for their description the amplitudes of the unitarized Breit-Wigner ansatz [13] that fully accounts for the unitarity restrictions on the resonant amplitudes. This model will be used in the proposed experiment for the analysis of exclusive $\pi^+\pi^- p$ electroproduction, allowing us to determine the electrocouplings of most excited nucleon states, since almost all nucleon resonances have substantial hadronic decays to the $N\pi\pi$ channel. The capability of the JM model to pin down new baryon states was demonstrated in the combined studies of exclusive $\pi^+\pi^- p$ photo- and electroproduction [33], which provided convincing evidence for a new $N(1720)\frac{3}{2}^+$ baryon state.

The model employed for the description of the KY exclusive photo- and electroproduction channels is the "Regge-plus-Resonance" (RPR) approach developed by the Ghent group [12, 58]. In this model the full production amplitude is described by the superposition of eight resonances and the non-resonant contribution. The non-resonant amplitudes represent the sum of t-channel exchanges by K- and K^*-Regge trajectories. The model provided a good description of KY photoproduction data. However, the RPR model only is able to produce the gross features of the available electroproduction data. The world's database for $K^+\Lambda$ and $K^+\Sigma^0$ electroproduction in the nucleon resonance region ($1.6 < W < 3.0$ GeV) in the domain of momentum transfer $0.5 < Q^2 < 4$ GeV^2 is completely dominated by the measurements of the CLAS program. These include measurements of beam-recoil transferred polarization [59, 60] and induced recoil polarization [61]. Also extensive measurements of the separated structure functions $\sigma_U = \sigma_T + \epsilon\sigma_L$, σ_{LT}, σ_{TT}, and $\sigma_{LT'}$ [62, 63, 64] have been published. Finally, the first Rosenbluth separation from CLAS data at beam energies of 2.5 and 4 GeV allowed for a separation of σ_T and σ_L [62, 65]. We are planning to use the RPR model for the extraction of the resonance electrocouplings from exclusive KY electroproduction data after the model has been refit and upgraded to be able to describe the available data. The development in this direction was presented in Ref. [66].

4 The Experimental Program

4.1 The CLAS12 Detector

The experimental program will use the CLAS12 detector, shown in Fig. 10, for the detection of the hadronic final states. CLAS12 consists of a Forward Detector (FD) and a Central Detector (CD). The Forward Detector is comprised of six symmetrically arranged sectors defined by the six coils of the superconducting torus magnet. Charged particle tracking is provided by a set of 18 drift chambers with a total of 36 layers in each sector. Additional tracking at $5^\circ - 35^\circ$ is achieved by a set of 6 layers of micromesh gas detectors (micromegas) immediately downstream of the target area and in front of the High Threshold Cherenkov Counter (HTCC). Particle identification is provided by time-of-flight information from two layers of scintillation counter detectors (FTOF). Electron, photon, and neutron detection are provided by the triple layer electromagnetic calorimeter, PCAL, EC(inner), and EC(outer). The heavy gas Cherenkov Counter (LTCC) provides separation of high momentum pions

from kaons and protons. The Central Detector consists of 6 to 8 layers (depending on the configuration) of silicon strip detectors with stereo readout and 6 layers of micromegas arranged as a barrel around the target, a barrel of scintillation counters to measure the particle flight time from the target (CTOF), and a scintillation-counter based Central Neutron Detector (CND). Further details on all CLAS12 components (magnets, detectors, data acquisition, software) are given in Ref. [67].

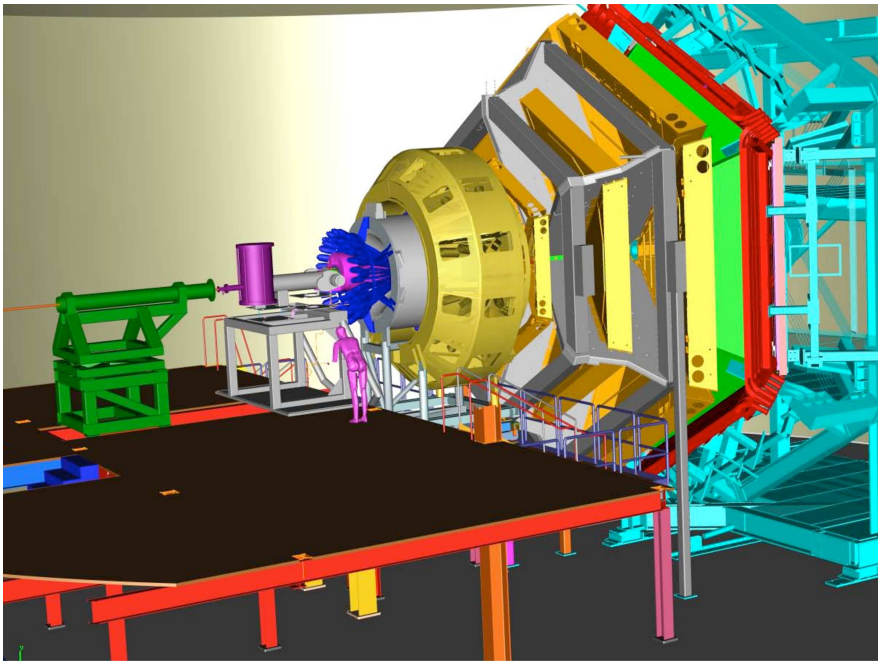

Figure 10: A model view of the CLAS12 detector that was designed to have high hermeticity and to allow for reconstruction of high multiplicity final states. This detector was designed to operate at a nominal luminosity of $\mathcal{L} > 10^{35}\text{cm}^{-2}\text{s}^{-1}$.

A longitudinally polarized electron beam will be scattered off a liquid-hydrogen target. The scattered electrons will be detected in the Forward Detector of CLAS12 for scattering angles greater than about 5° and in Forward Tagger for angles from 2.5° to 4.5°, which allows us to cover the Q^2 range of interest between 0.05 GeV^2 and 2 GeV^2. Charged hadrons will be measured in the full polar angle range from 5° to 130°. At an operating luminosity of $\mathcal{L} = 1 \times 10^{35}$ cm^{-2}s^{-1} the total hadronic rate is expected to be 5×10^6 s^{-1}.

4.2 The Forward Tagger

An essential component of the hadron spectroscopy program with CLAS12 is the Forward Tagger (FT) shown in Fig. 11. The FT uses a high resolution crystal calorimeter composed of 324 lead-tungstate crystals to measure the scattered electrons in the polar angle range from 2.5° to 4.5° and with full coverage in azimuthal angle. The calorimeter measures electron and photon energies with an energy resolution of $\sigma(E)/E \leq 0.02/\sqrt{E(\text{GeV})} + 0.01$. The fine granularity of the calorimeter also provides good polar angle resolution. A two-layer tiled scintillator hodoscope is located in front of the calorimeter for the discrimination of photons. An additional four-layer micromegas tracker, located in front of the hodoscope, is used for precise electron tracking information. Electron detection in the FT will allow us to probe

the crucial low Q^2 range where hybrid baryons may be identified due to their fast dropping $A_{1/2}(Q^2)$ amplitude and the expected suppression of their scalar $S_{1/2}(Q^2)$ amplitude.

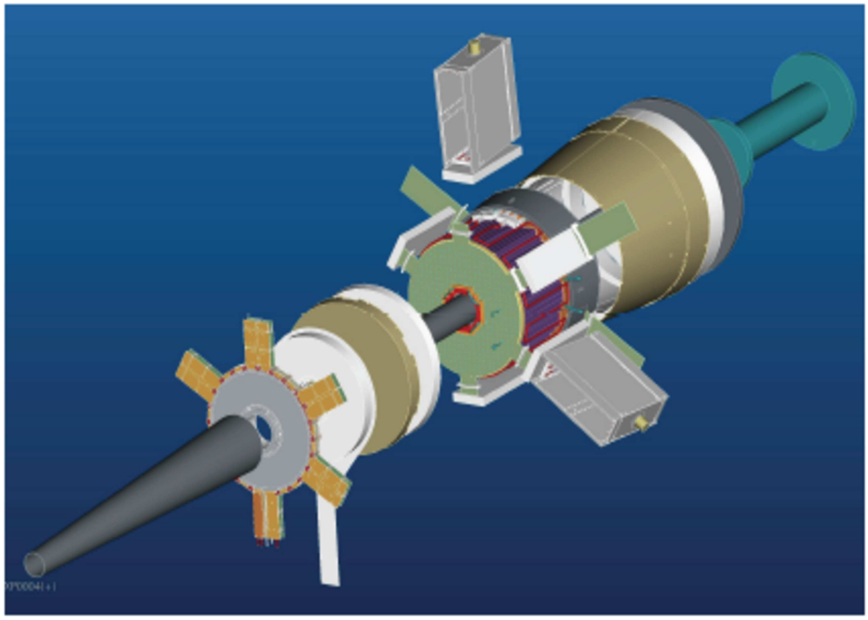

Figure 11: The Forward Tagger (FT) system. The FT provides electron and high energy photon detection in a range of CLAS12 polar angles $\theta = 2.5^\circ - 4.5^\circ$.

The construction of the FT was completed by a collaboration of INFN/Genova (Italy), CEA/Saclay (France), and the University of Edinburgh (UK). The FT is now undergoing cosmic ray testing at JLab and will be installed into CLAS12 in summer 2016.

4.3 Kinematic Coverage of Electron Scattering in CLAS12

The CLAS12 detector acceptance for inclusive electron scattering events has been studied using a fast Monte Carlo program (FASTMC), which includes a simplified version of the full CLAS12 reconstruction code. The event reconstruction takes into account the high efficient fiducial areas of the detector and provides smearing of the final state charged particle momenta. The optimal beam energies and torus current settings have been studied with the goal to maximize the scattered electron acceptance in Q^2 and W.

The virtuality of the emitted photon Q^2 is related to the scattered electron energy E'_e and polar angle θ_e through the relation $Q^2 = 4E_eE'_e\sin^2\frac{\theta_e}{2}$. Reaching the lowest Q^2 requires detecting the electrons emitted with the smallest scattering angle in the FT and using relatively low electron beam energies.

If a positive torus current is applied, the scattered electrons are forced to bend inward toward the beam axis, which causes an increase in the minimum detectable Q^2 value in CLAS12. On the contrary, a negative torus current forces the scattered electrons to bend outward, lowering the value of the minimum accessible Q^2. Fig. 12 shows scatterplots of Q^2 vs. W for the detected electrons in CLAS12 for torus currents of $I = +3375$ A and $I = -3375$ A (the nominal maximum supply operating current) at E_b=11 GeV, the maximum electron beam energy available in Hall B. The empty region corresponds to the gap between

the FT and the minimum polar angle accepted in the CLAS12 Forward Detector calorimeters. This coverage gap is clearly minimized operating the torus magnet at negative polarity. The corresponding electron acceptances vs. Q^2 are also shown in Fig. 12. The electrons that are detected in the FT at E_b=11 GeV correspond to an accessible Q^2 range from 0.2 GeV^2 to 0.6 GeV^2. The electrons detected in the CLAS12 Forward Detector calorimeters have a lower geometrical efficiency due to the defined fiducial areas of these detectors and cover a higher Q^2 range that starts from 0.8 GeV^2 or 1.4 GeV^2 for the negative and positive torus currents, respectively.

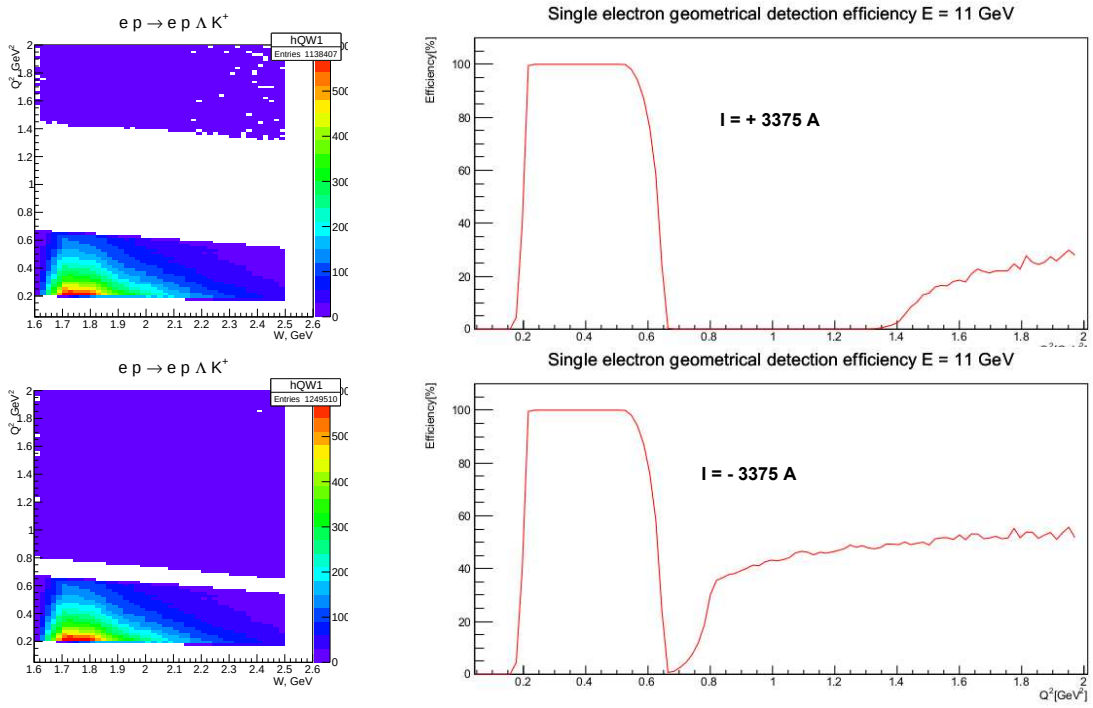

Figure 12: (Left) Q^2 vs. W scatterplots of the detected electrons in CLAS12 for the $ep \rightarrow e'K^+\Lambda$ reaction for torus currents $I = +3375$ A (top) and $I = -3375$ A (bottom) for $E_e = 11$ GeV. (Right) The corresponding electron acceptances as a function of Q^2.

Reaching the low-Q^2 region desired for this proposal requires lowering the electron beam energy. Fig. 13 shows a scatterplot of Q^2 vs. W for the detected electrons in CLAS12 for a torus current of $I = -3375$ A at electron beam energies of E_e=6.6 GeV and E_e=8.8 GeV. The corresponding electron acceptances vs. Q^2 at these energies are also shown in Fig. 13. At E_e=6.6 GeV the minimum accepted Q^2 value is as low as 0.05 GeV^2 and the accessible Q^2 range extends up to 2 GeV^2, with a gap between 0.15 GeV^2 and 0.3 GeV^2. This gap may be covered if an electron beam energy of E_e=8.8 GeV is used, as shown in the bottom plots of Fig. 13. In this case the Q^2 threshold is 0.1 GeV^2 and the acceptance gap appears in the interval from 0.35 GeV^2 to 0.5 GeV^2, providing a nicely complementary range of measurable photon virtualities.

We conclude that the optimal experimental settings for the present proposal require beam time at both E_e=6.6 GeV and E_e=8.8 GeV with operation of the CLAS12 torus at $I = -3375$ A, corresponding to negative polarity with the current set to its maximum nominal value. Detailed simulations for the $\pi^+\pi^-p$ final state are described in Section 5 and for the KY final states in Section 6.

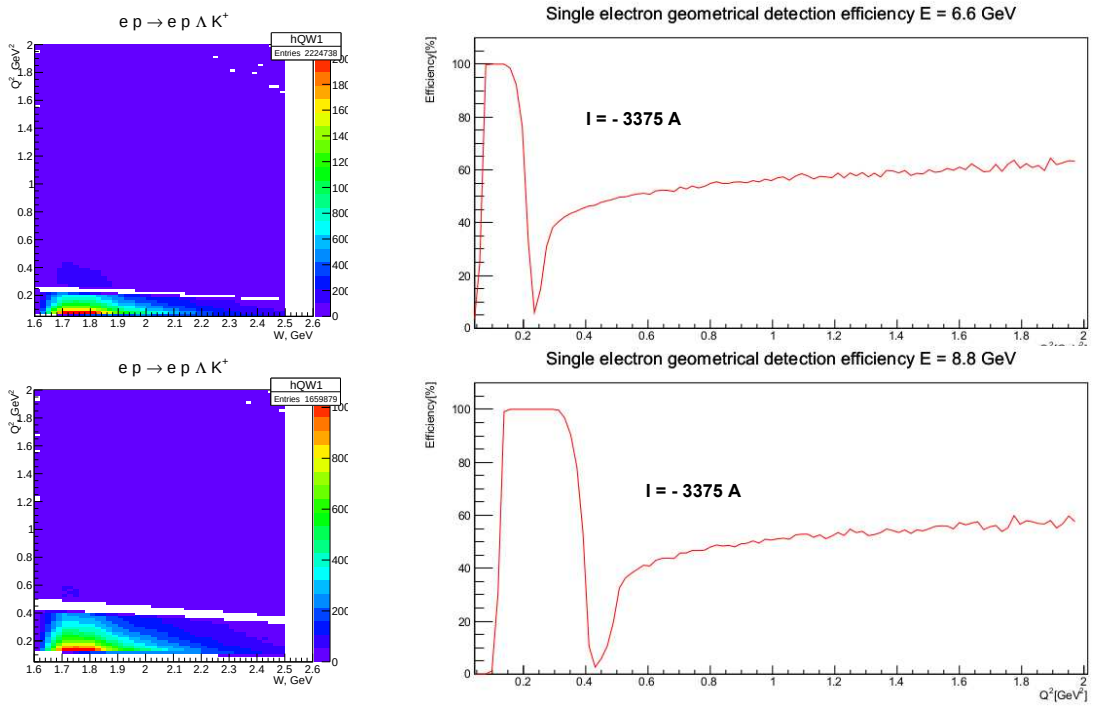

Figure 13: (Left) Q^2 vs. W scatterplots of the detected electrons in CLAS12 for the $ep \to e'K^+\Lambda$ reaction for torus current $I = -3375$ A for $E_e = 6.6$ GeV (top) and $E_e = 8.8$ GeV (bottom). (Right) The corresponding electron acceptances as a function of Q^2.

5 Simulations for the $ep \to e'p\pi^+\pi^-$ Final State

5.1 Event Generator for $ep \to e'p\pi^+\pi^-$

The standard 2π event generator for CLAS was a modified version of GENEV employing the $\pi^+\pi^-p$ differential cross sections from the older JM05 version of the JM model [34, 71, 72]. During the past several years the JM model has been further developed and significantly improved [11]. Furthermore, the two-pion part of the old GENEV event generator was only applicable up to $W \approx 2$ GeV and $Q^2 < 0.3$ GeV^2, which excludes most of the region of interest (high W and low Q^2) for this proposal. Therefore a new generator for $\pi^+\pi^-p$ electroproduction was developed for our studies.

The new event generator employs the five-fold differential cross sections from the recent version of the JM15 model fit to all results on the charged double pion photo- and electroproduction cross sections from CLAS (both the published and preliminary [13, 47, 49, 56]). In the areas covered by CLAS data, the new event generator successfully reproduces the available integrated and single differential 2π cross sections. The quality of the description is illustrated in Fig. 14 for several Q^2 bins in comparison with the available data [13, 47, 56].

In order to extend the event generator to areas not covered by the existing CLAS data, a special extrapolation procedure was applied that included additional available world data on the W dependencies of the integrated 2π photoproduction cross sections [68, 69]. The new approach allows for the generation of 2π events at extremely low Q^2 (less than 0.1 GeV^2) and high W (up to 3 GeV). On the left side of Fig. 15 the W dependence of the integrated cross section for quasi-real Q^2 (0.0015 GeV^2) is shown in comparison with the available data

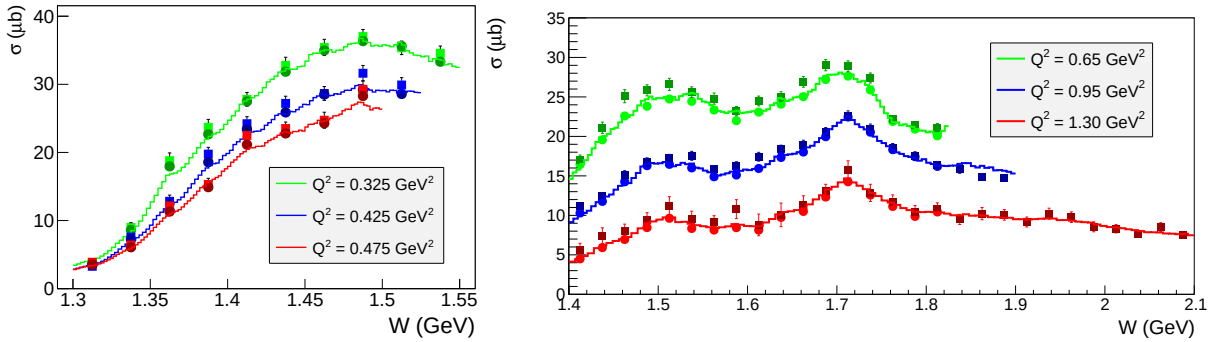

Figure 14: Comparison between the event distributions of the new two-pion event generator (curves) with the integrated cross sections from the JM model (circles) and data (squares). (Left) The W dependence of the total cross section in comparison with the model [13] and data [56] for three Q^2 points at 0.325 GeV^2, 0.425 GeV^2, and 0.475 GeV^2. (Right) The W dependence of the total cross section in comparison with the model [11] and data [47] for three Q^2 points at 0.65 GeV^2, 0.95 GeV^2, and 1.3 GeV^2.

[49, 68, 69]. The right side of Fig. 15 illustrates a typical example of the Q^2 dependence of the total cross section for one W bin in comparison with JM15 [11] for E_b=8.8 GeV.

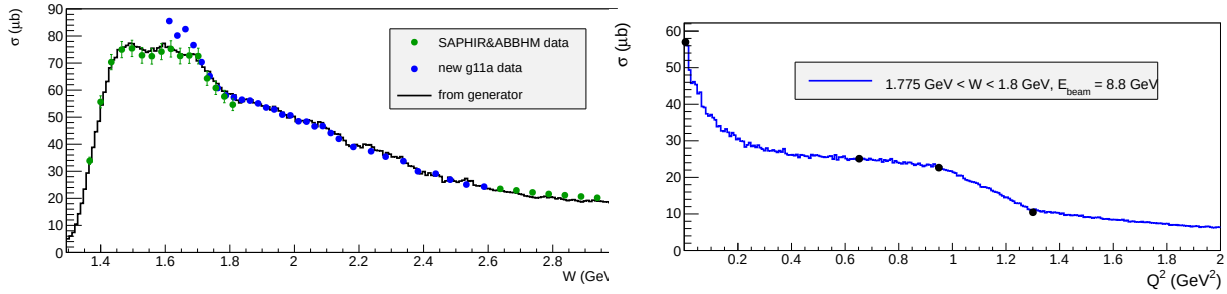

Figure 15: (Left) The W dependence of the integrated cross section for quasi-real Q^2 (0.0015 GeV^2) in comparison with the available data [49, 68, 69]. (Right) A typical example of the Q^2 dependence of the total cross section for one W bin in comparison with JM15 [11] at W = 1.7875 GeV for E_b=8.8 GeV.

The new 2π event generator has several advantages compared to the GENEV code. First it generates phase space distributions and applies a multi-dimensional cross section as a weight for each event. This method allows for a significantly faster generation process, especially in the areas with sharp cross section dependencies. The new generator also makes it possible to obtain cross sections from the generated distributions, which is helpful to predict the cross section in areas not covered by the experiment. The new 2π event generator is written in C++. It includes inclusive radiative effects according to the approach described in Ref. [70] and produces an output compatible with the new CLAS12 reconstruction software.

Exclusive events for $\pi^+\pi^-p$ electroproduction off the proton were generated in the range of W from the two-pion production threshold to 3 GeV and at Q^2 from 0.01 GeV^2 to 2.0 GeV^2 (see Fig. 16).

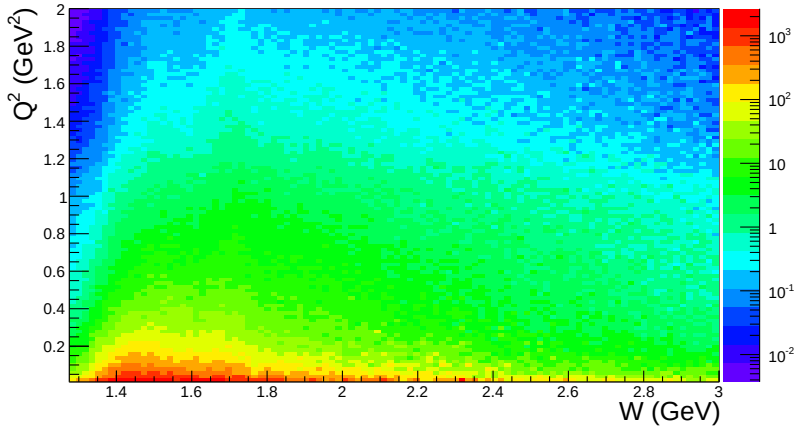

Figure 16: Q^2 versus W distribution for the generated $\pi^+\pi^- p$ events for E_b=6.6 GeV.

5.2 Acceptance Estimates for $ep \rightarrow e'p\pi^+\pi^-$

For the event reconstruction a simplified version of the CLAS12 event reconstruction software called FASTMC was employed to filter the generated events to determine the CLAS12 acceptance. The accepted $\pi^+\pi^- p$ events in Q^2 vs. W are shown in Fig. 17 at E_b=6.6 GeV and 8.8 GeV for the torus current set to $I = +3375$ A, which forces negatively charged particles to bend toward the beamline. Similar to the results obtained in Section 4.3, areas of zero acceptance can be seen in the plots, representing the gap between the Forward Tagger and the minimum polar angle accepted in the CLAS12 Forward Detector calorimeters. For the hybrid baryon search, the area of small photon virtuality is of particular interest. The size of the gap depends on the torus current setting and the momentum of the scattered electrons. For a negative torus current, i.e. outbending electrons, the gap is simply given by the geometrical acceptance of CLAS12 and is largely independent of the particle momentum, while for inbending particles the acceptance depends on scattering angle, particle momentum, and magnetic field strength. The acceptance for electron scattering angles from 2.5° to 4.5°, which is covered by the FT, is independent of the torus current settings. A simulated $ep \rightarrow e'p\pi^+\pi^-$ event in CLAS12 using the GEANT-4 simulation suite GEMC [74] is shown in Fig. 18.

With a beam energy of 6.6 GeV, the influence of the magnetic field polarity on the accessible kinematic coverage for $\pi^+\pi^- p$ electroproduction was further studied. The Q^2 versus W distributions for reconstructed $\pi^+\pi^- p$ events are shown in Fig. 19 for torus settings of $I = +3375$ A and $I = -3375$ A. A wide area of zero acceptance for the positive torus polarity setting of $I = +3375$ A is clearly seen in Fig. 19 (left). Reversing the magnetic field allows us to substantially decrease the inefficient area, as shown in Fig. 19 (right). Therefore, as anticipated in Section 4.3, the reversed magnetic field setting represents the best configuration for the proposed experiment.

We also examined the evolution of counting rates as a function of the magnetic field strength. The Q^2 versus W distributions for the accepted $\pi^+\pi^- p$ events are shown in Fig. 20 for torus currents $I = -3375$ A (left) and $I = -1500$ A (right). Comparing the reconstructed event rates shown in Fig. 20, we expect the counting rate to increase by almost a factor of two at half strength of the magnetic field because of the improved acceptance for the detection

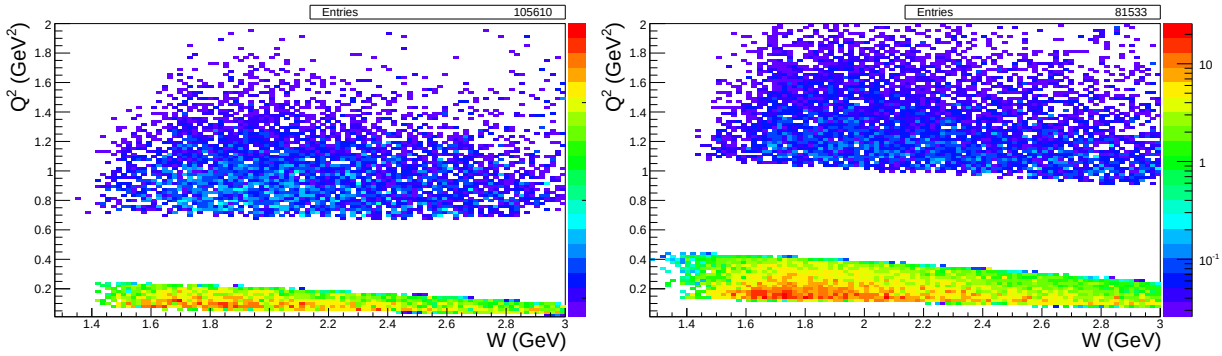

Figure 17: Q^2 versus W distributions for the reconstructed $\pi^+\pi^-p$ events (all particles in final state are registered). The left and right plots correspond to E_b=6.6 GeV and 8.8 GeV, respectively. The torus current is set to $I = +3375$ A.

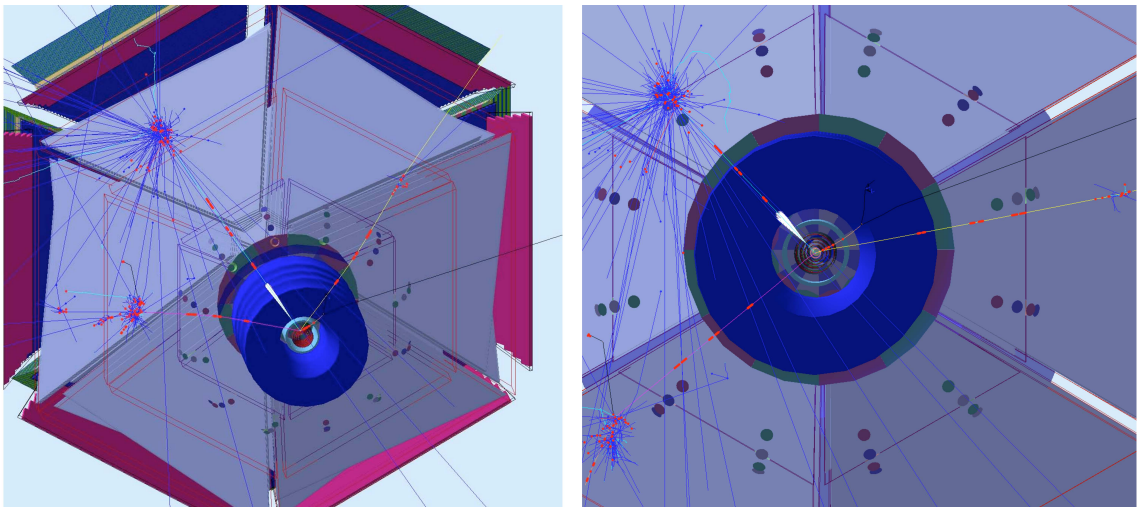

Figure 18: A GEANT-4 $ep \rightarrow e'p\pi^+\pi^-$ event as seen in CLAS12. (Left) The scattered electron (cyan) generates Cherenkov light in the HTCC, leaves track segments in the 3 drift chamber regions, hits in the FTOF planes, and finally showers in the PCAL & EC calorimeters. The two pions π^+ (purple line) and π^- (yellow line) are tracked in the DCs and leave hits in the FTOFs and calorimeters. The proton (short orange line) is tracked at large angles inside the solenoid magnet in the four SVT regions and leaves hits in the CTOF. (Right) A close-up view of the same event from a different angle. The torus magnet in this illustration was set at 50% of full current.

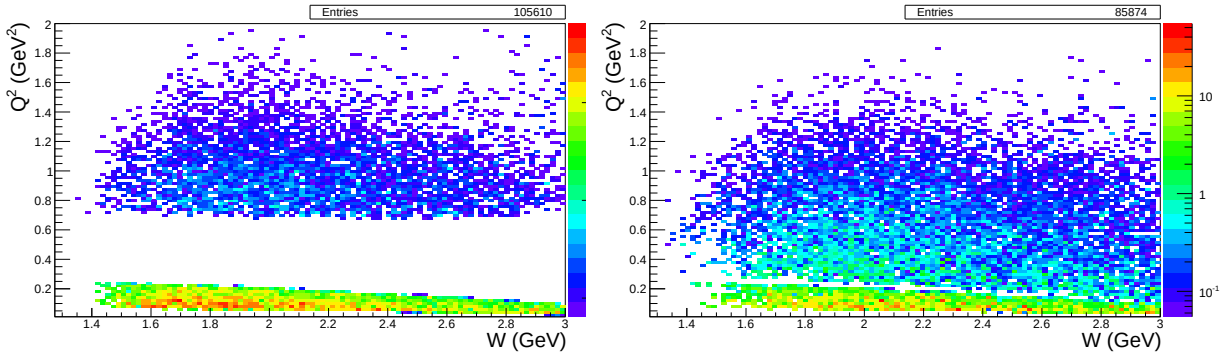

Figure 19: Q^2 versus W distributions at E_b=6.6 GeV for reconstructed $\pi^+\pi^-p$ events (all particles in final state are registered) for torus settings of $I = +3375$ A (left) and $I = -3375$ A (right). The reversed magnetic field closes the gap between the Forward Tagger and the CLAS12 Forward Detector calorimeters.

of all three particles (π^+, π^-, p) in the final state and the scattered electron. On the other hand, decreasing the torus current will negatively affect the charged particle momentum resolution, so the maximum negative torus current is optimal for this proposal.

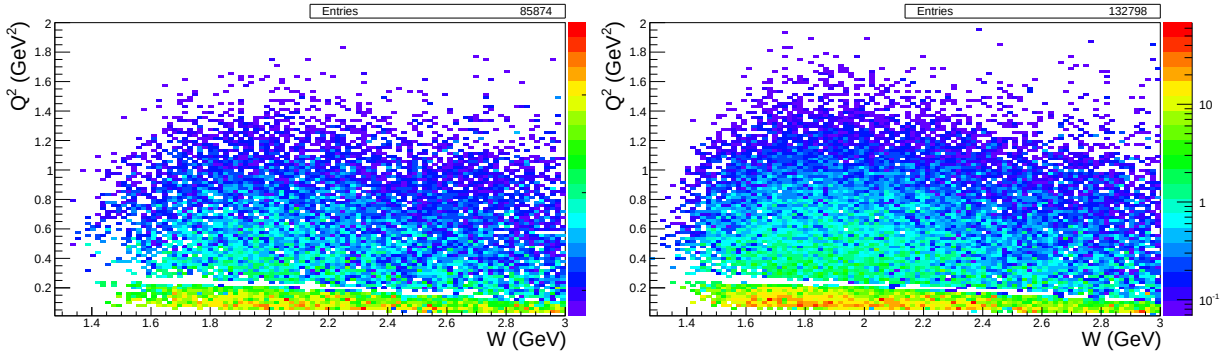

Figure 20: Q^2 versus W distributions at E_b=6.6 GeV for reconstructed $\pi^+\pi^-p$ events (all final state particles are registered) for torus settings of $I = -3375$ A (left) and $I = -1500$ A (right). With lower torus current more events are reconstructed.

5.3 Hadronic Mass Reconstruction for $ep \to e'p\pi^+\pi^-$

The hadronic mass resolution is of particular importance in studies of excited nucleon states, since this quantity determines the ability to reliably extract the resonant contributions in exclusive cross sections. For a credible separation between the resonant and the non-resonant contributions, the resolution in W should be much smaller than the N^* decay width. Typical values for the decay widths of nucleon resonances with masses > 2.0 GeV are in the range from 250 MeV to 400 MeV. Hence a mass resolution of ≈ 30 MeV is sufficient for the reliable isolation of contributions from hybrid baryons that are expected in the mass range from 2.0 GeV to 3.0 GeV. The resolution in W for the reconstructed $\pi^+\pi^-p$ events was studied

by computing for each reconstructed event the difference between the exact W_{gen} and the reconstructed W_{rec}. We compared two different ways of determining the invariant mass of the final hadronic system: a) from the difference between the four-momenta of the initial and the scattered electrons that is added to the four-momentum of the target proton (electron scattering kinematics) and b) from the sum of the four-momenta of the final state π^+, π^-, and p (hadron kinematics). The reconstructed $W_{gen} - W_{rec}$ event distributions provide the necessary information on the invariant mass resolution.

The aforementioned distributions for the electron scattering and hadron kinematics are shown in Fig. 21. The beam energy is set to 6.6 GeV and the torus current to $I = -3375$ A. For both ways of determining W_{rec}, the resolution over the full W range is better than 30 MeV and sufficient for the separation of the resonant and non-resonant contributions. If W_{rec} is computed from the hadron kinematics, the resolution is significantly better than in the case of the electron scattering kinematics. However, the hadron kinematics requires the registration of all final state hadrons with a detection efficiency lower than in the inclusive case where the value of W_{rec} is determined.

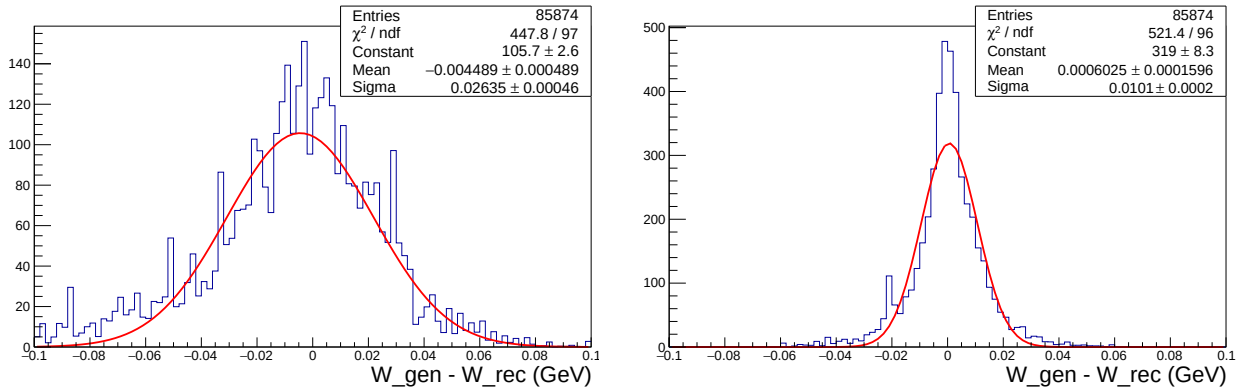

Figure 21: The $W_{gen} - W_{rec}$ distributions for $\pi^+\pi^-p$ events where W_{rec} is determined by electron scattering (left) and hadron (right) kinematics. See text for explanation of both kinematics.

The studies of charged double pion electroproduction with the CLAS detector [47, 56] demonstrated that the topology where the final π^- is not detected and its four-momentum is reconstructed from energy-momentum conservation provides the dominant part of the statistics. Hence topologies in which one of the final state hadrons is not detected will also provide the dominant statistics in the proposed experiment. We are planning to select the $\pi^+\pi^-p$ events by employing exclusivity cuts on the missing mass squared distributions of any of the final hadrons. The contribution from other exclusive channels (exclusive background) to the events within the exclusivity cuts was evaluated in the Monte Carlo simulation. Most of the exclusive background events come from the $ep \to e'p'\pi^+\pi^-\pi^0$ channel. Both $\pi^+\pi^-p$ and $\pi^+\pi^-\pi^0p$ events were generated for $W > 2$ GeV. The cross sections for the 2π and 3π channels were assumed comparable in this kinematic region. A phase space distribution is assumed for the 3π events. With this mixture of generated events, we reconstructed the $\pi^+\pi^-p$ events and determined their distribution over the relevant missing mass squared range for π^+ and π^-. The blue curves in Fig. 22 show the 2π event contributions and the green curves represent the 3π event contributions. The exclusivity cuts provide good isolation of

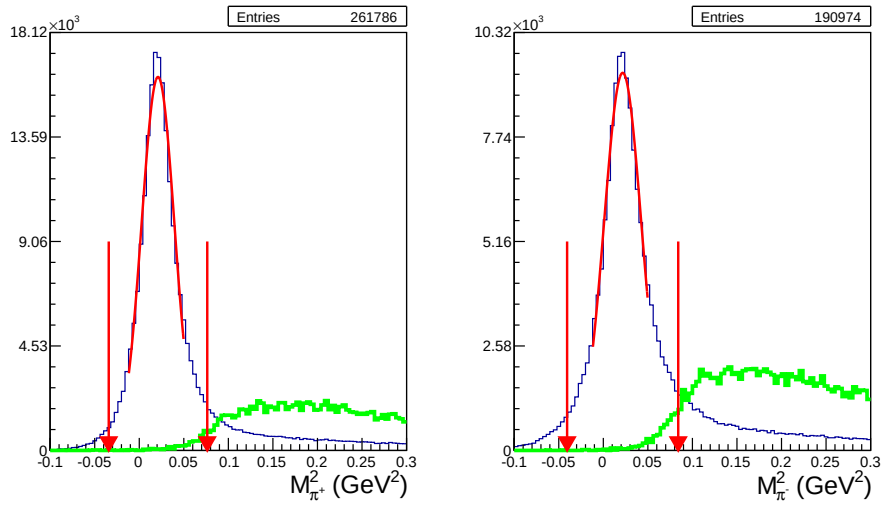

Figure 22: The reconstructed $\pi^+\pi^-p$ event distributions of the missing masses squared of π^+ (left) and π^- (right) for the generated $\pi^+\pi^-p$ events with an admixture of 3π events. The distributions were plotted for $W > 2$ GeV. The cross sections for the 2π and 3π channels were assumed comparable in this kinematic region. The contributions from the $\pi^+\pi^-p$ and the $\pi^+\pi^-\pi^0p$ events are shown in blue and green, respectively. The red arrows indicate the applied exclusivity cuts.

the $\pi^+\pi^-p$ events with the following contributions from the 3π events: $\sim 3\%$ for the missing π^+ topology and $\sim 4\%$ for the missing π^- topology.

5.4 Summary of $ep \to e'p\pi^+\pi^-$ Experimental Conditions Study

The summary of the run conditions studied in the $\pi^+\pi^-p$ simulations described above is given in Table 1. The bold rows correspond to the optimal set-up for the proposed experiment at E_b=6.6 GeV and 8.8 GeV with a torus setting of $I = -3375$ A. The columns labeled "Eff. %" represent the CLAS12 acceptance factors for different particles detected in the final state). The table also lists the minimum Q^2 possible. Finally the columns labeled $\sigma(W_e)$ and $\sigma(W_h)$ represent the hadron mass resolution for the electron scattering and hadron kinematics, respectively, detailed in Section 5.3.

The kinematic coverage in terms of the ϕ versus θ distributions for the final state hadrons is shown in Fig. 23 for all final state hadrons detected, a beam energy of 6.6 GeV, and a torus current $I = -3375$ A. The vertical strips at $\theta \sim 35°$ in all plots of Fig. 23 correspond to the detector gap between the CLAS12 Forward Detector and Central Detector. Since a reversed torus magnetic field was chosen, the low angle area is better populated for negatively charged particles (π^-).

Energy) (GeV)	Torus (A)	Eff. (%) all rec.	Eff. (%) π^+ miss	Eff. (%) π^- miss	Eff. (%) p miss	Q^2_{min} (GeV^2)	$\sigma(W_e)$ (MeV)	$\sigma(W_h)$ (MeV)
8.8	+3375	8.2	9.8	10.3	8.6	0.13	35	11
8.8	**-3375**	**8.3**	**12.7**	**10.6**	**12.1**	**0.13**	**33**	**10**
8.8	+1500	11.5	12.9	11.9	11.6	0.13	35	11
8.8	-1500	12.8	16.8	13.5	16.0	0.13	36	11
6.6	+3375	10.6	13.0	14.1	11.4	0.05	27	11
6.6	**-3375**	**8.7**	**13.8**	**11.5**	**13.1**	**0.05**	**26**	**10**
6.6	+1500	15.0	17.3	16.3	15.7	0.05	25	11
6.6	-1500	13.4	18.4	14.8	17.7	0.05	29	10

Table 1: Comparison of run conditions for the $\pi^+\pi^-p$ channel. The bold rows represent the optimal run conditions for E_b=6.6 GeV and 8.8 GeV with the torus setting of $I = -3375$ A.

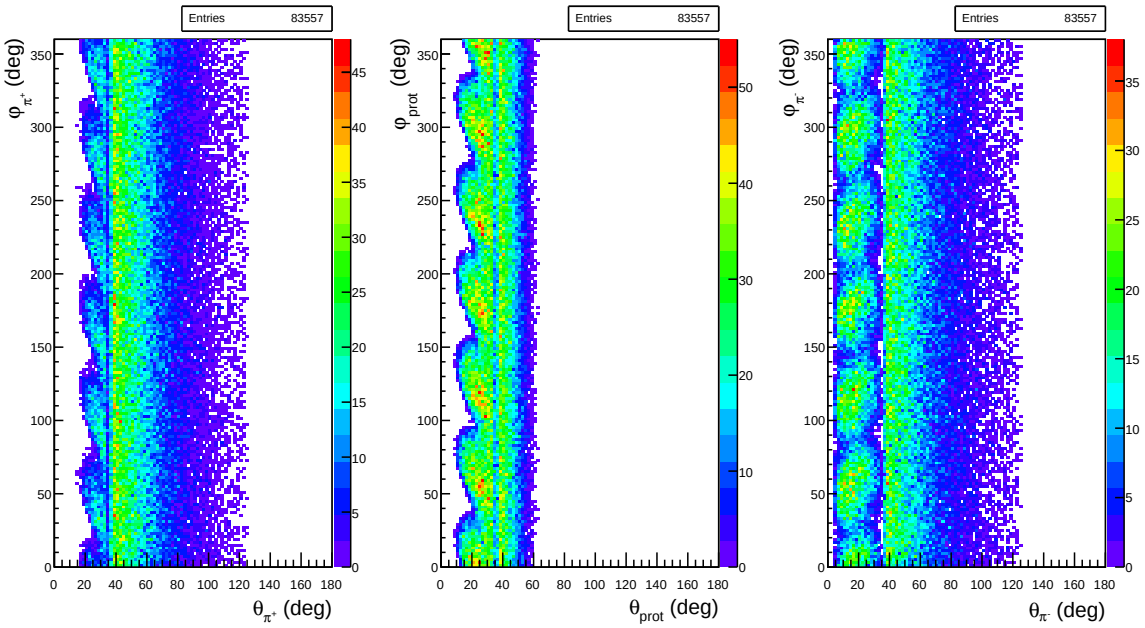

Figure 23: Laboratory ϕ vs θ distributions for the final state hadrons: π^+ (left), p (middle), and π^- (right).

6 Simulations for the $K^+\Lambda$ and $K^+\Sigma^0$ Final States

6.1 K^+Y Event Generators

The $ep \rightarrow e'K^+Y$ event generators are based on model cross section calculations. The models for the $K^+\Lambda$ [12] and for the $K^+\Sigma^0$ [58] channels describe KY electroproduction in the framework of a Regge-plus-resonance approach. The resonance contributions in the s-channel are described with the help of the effective-Lagrangian approach and the background part of the amplitude is modeled in terms of t-channel Regge-trajectory exchange.

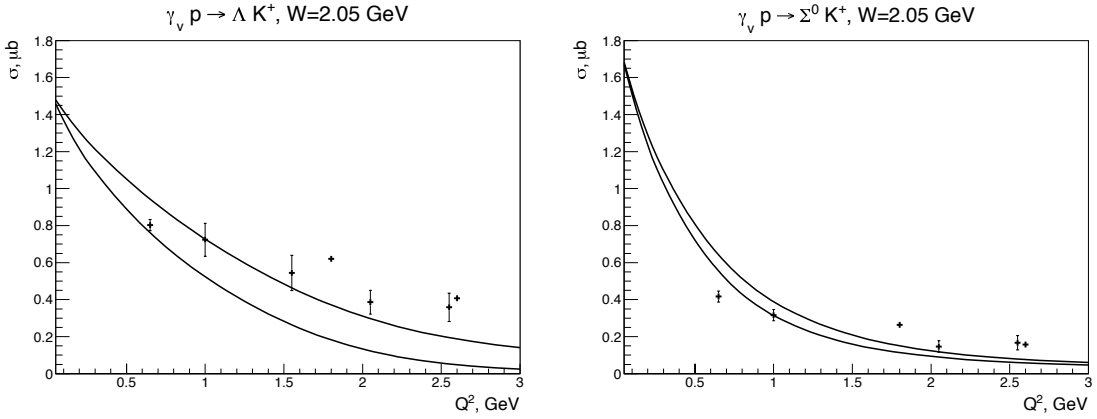

Figure 24: Integrated cross section for $K^+\Lambda$ (left) and $K^+\Sigma^0$ (right) from CLAS measurements as a function of Q^2 at $W = 2.05$ GeV [62, 64]. The cross sections at $Q^2 = 0.65$ GeV^2 are measured at a beam energy of 2.567 GeV and the cross sections at $Q^2 = 1.8$ GeV^2 and 2.6 GeV^2 are measured at a beam energy of 5.5 GeV. All other Q^2 points correspond to a beam energy of 4.056 GeV. The RPR model calculations [12, 58] are shown for E_b=2.567 GeV (upper curve) and E_b=5.5 GeV (lower curve).

A comparison of the fully integrated model cross section with experimental CLAS data is shown in Fig. 24. The cross sections are presented as a function of Q^2 for a given W bin at $W = 2.05$ GeV. The differential cross sections for representative bins of Q^2 and W are shown in Figs. 25 and 26. The model reproduces the experimental data for 0.65 $GeV^2 < Q^2 < 1.5$ GeV^2, while it considerably underestimates the cross section for $Q^2 > 1.5$ GeV^2. This underestimation is especially notable in the $K^+\Sigma^0$ channel for high Q^2 and low W. This discrepancy is not a serious concern since our kinematic region of interest is at low Q^2. However, we do have to rely on a model for the cross section as there are no experimental data available below Q^2=0.65 GeV^2 with which to compare. We can see in Figs. 25 and 26 that the model reproduces well the general features of the sharp cross section growth at large $\cos\theta_K$ for $Q^2 > 1.5$ GeV^2 and $W > 2.0$ GeV. The data included in Figs. 25 and 26 are from the CLAS measurements from Refs. [62, 64]. The Regge-plus-Resonance (RPR) model version shown included here are known as the RPR-2011 variant for the $K^+\Lambda$ final state and the RPR-2007 variant for the $K^+\Sigma^0$ final state. Further detailed comparisons of these models to the available data from CLAS for the differential cross sections, separated structure functions, and induced and transferred polarizations are given in Refs. [60, 61, 62, 63, 64].

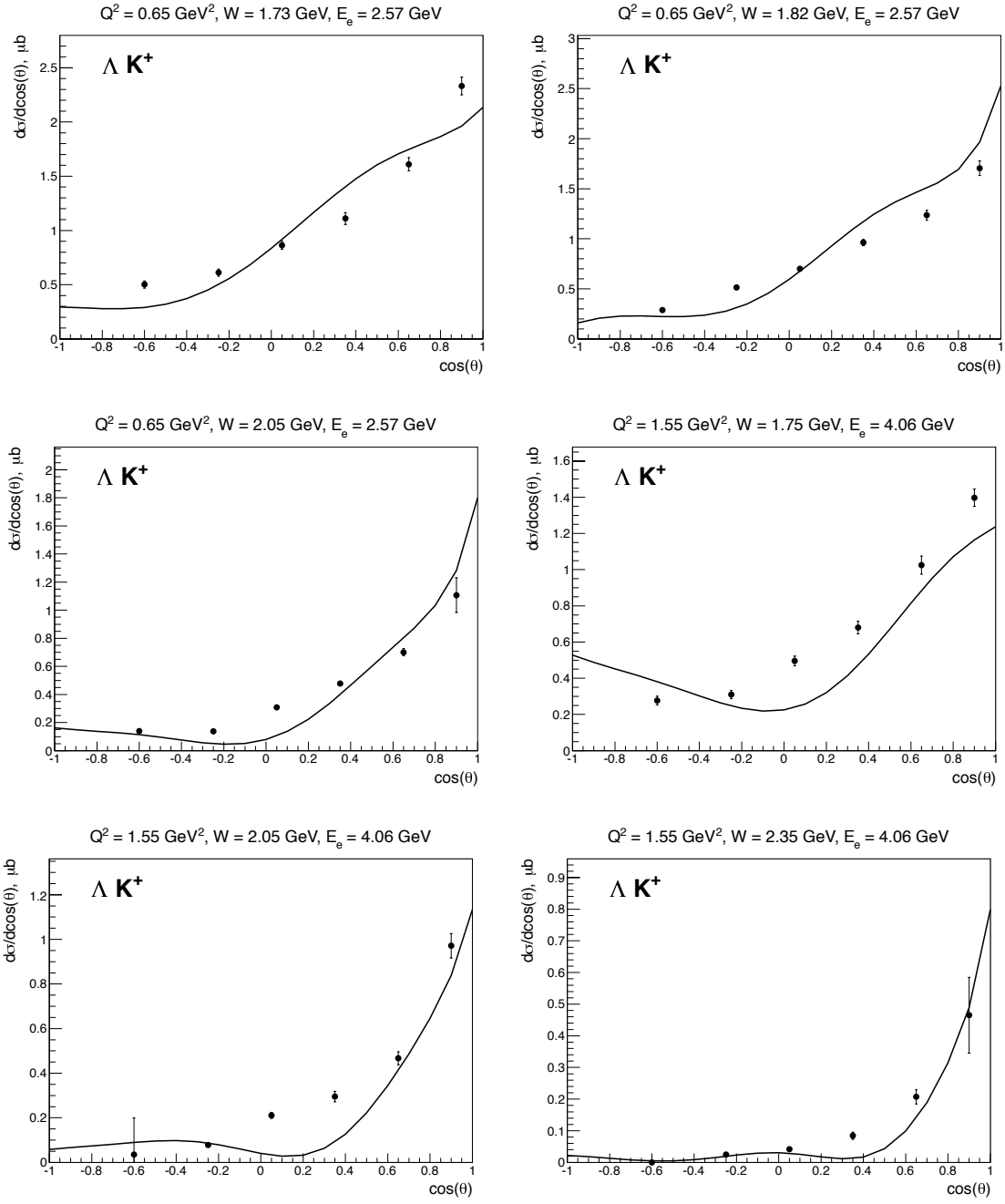

Figure 25: Differential cross sections for the $K^+\Lambda$ channel as a function of $\cos\theta_K$ from CLAS measurements in various Q^2 and W bins for two beam energies (E_b=2.57 GeV and 4.06 GeV) [62, 64] compared to the RPR model predictions (RPR-2011 variant) [12].

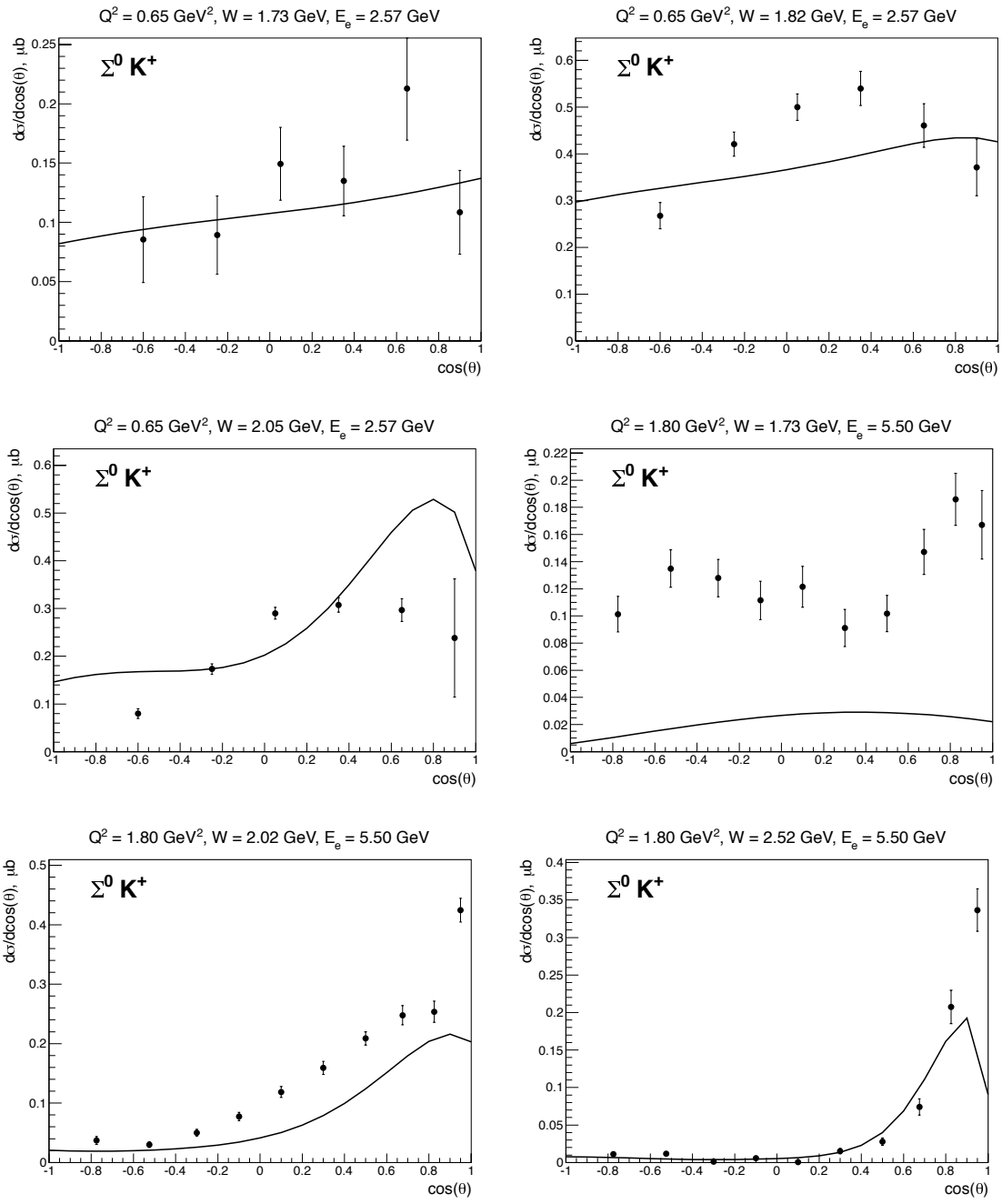

Figure 26: Differential cross sections for for $K^+\Sigma^0$ channel as a function of $\cos\theta_K$ from CLAS measurements in various Q^2 and W bins for two beam energies (E_b=2.57 GeV and 5.5 GeV). [62, 64] compared to the RPR model predictions (RPR-2007 variant) [58].

6.2 Acceptances for $ep \rightarrow e'K^+\Lambda$

In Figs. 27 and 28 we compare the angular distributions of all final states particles for an electron beam of 6.6 GeV and for torus currents of $I = +3375$ A and $I = -3375$ A. In Fig. 27 we see qualitatively the same behavior as for the $p\pi^+\pi^-$ final state: inbending electrons generated in a W interval from $K^+\Lambda$ threshold at 1.6 GeV to 3.5 GeV and scattering angles $\theta_e \geq 2^\circ$ are detected in CLAS12 starting at about 5° with the acceptance opening up toward larger scattering angles. The twisting pattern seen in the accepted p and K^+ plots is due to the azimuthal motion of charged tracks in the strong central solenoid field that generates a "kick" in azimuth that depends on the production angle and the particle momentum. It should be noted that the particles are not traversing the sectors in this pattern, as the plotted quantities are the values at the production vertex. The pattern for the π^- is different as they have on average much lower momenta and their migration in ϕ is larger and more diffuse.

For KY production off hydrogen, the recoil protons are kinematically limited to polar angles of $\leq 65^\circ$. Figure 28 shows the acceptances for outbending electrons for which the polar angle gap between the FT and the CLAS12 Forward Detector calorimeters is strongly reduced and the azimuthal response is more uniform. As a result, the event acceptance for this configuration is almost a factor of two larger than for the inbending field configuration. We also note that for both configurations there exists a polar-angle band at $\theta \approx 35^\circ$ where the acceptance is depleted due to the partially blind transition region between the Forward and Central Detector systems.

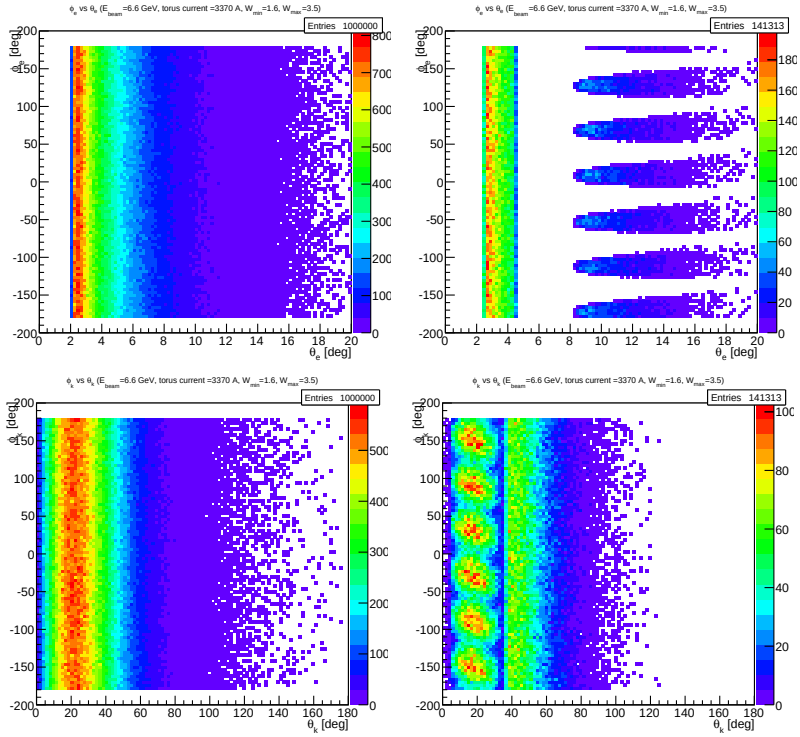

Figure 27: **(Add missing figures)** Azimuthal versus polar angle of generated (left) and accepted events (right) for electrons (top row), K^+ (2nd row), protons (third row), and π^- (bottom row). Events are generated for an electron beam energy of 6.6 GeV in a W range from 1.6 GeV to 3.5 GeV. The torus current is set I=+1500 A, that bends negatively charged particles inward towards the beamline and reduces the acceptance for electrons within CLAS12.

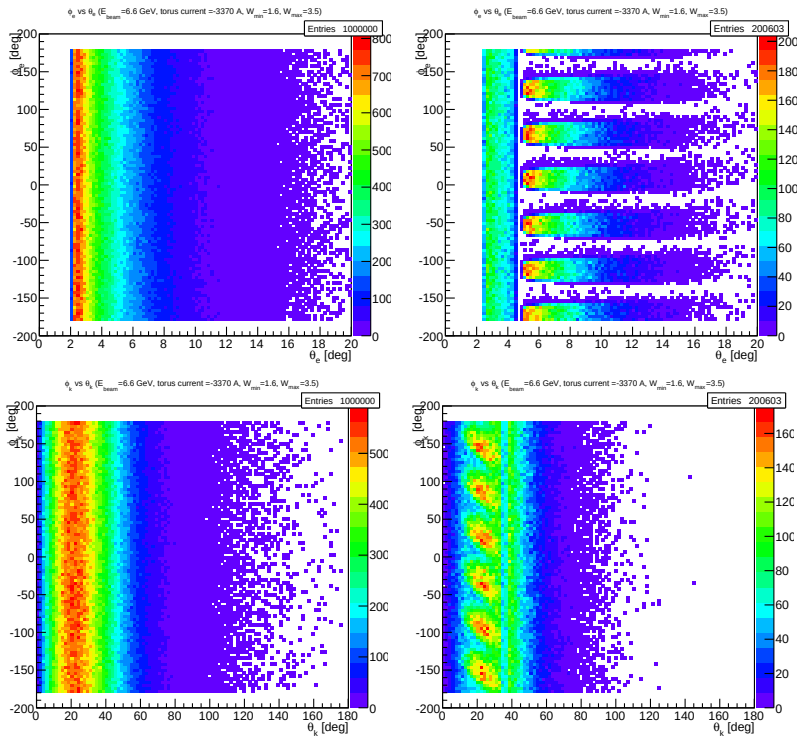

Figure 28: **(Add missing figures)** Azimuthal versus polar angle of generated (left) and accepted events (right) for electrons (top row), K^+ (2nd row), protons (third row), and π^- (bottom row). Events are generated for an electron beam energy of 6.6 GeV in a W range from 1.6 GeV to 3.5 GeV. The torus current is set at I=-1500 A, that causes negatively charged particles to bend outwards.

6.3 Run Conditions

We are planning to search for the hybrid states at low Q^2 and the accessible range of Q^2 depends on the beam energy and torus current. Another issue that affects the selection of the best run conditions is that we need good particle momentum resolution to be able to separate the $K^+\Lambda$ and $K^+\Sigma^0$ electroproduction channels and the best resolution is achieved with larger torus currents. The $K^+\Lambda$ and $K^+\Sigma^0$ channel separation is based on using cuts on the reconstructed $e'K^+$ missing mass. For this purpose the final state K^+ must be detected. Thus, we have to use the topologies where the final state electron, the K^+ and at least one of the other hadrons (p or π^-) are detected. The detection of the decay p or π^- from the Λ decay is required in order to measure the induced and transferred polarizations of the hyperons. Measurements of these hyperon polarization components from CLAS data are given in Refs. [59, 60].

The run condition studies were performed with the CLAS12 FASTMC program. Table 2 summarizes the minimum Q^2 coverage for the K^+Y final states at E_b=6.6 GeV and 8.8 GeV for different torus field settings and polarities. As already mentioned in Section 4.3, the optimal running conditions correspond to a data collection with a large negative torus current as the maximal $K^+\Lambda$ and $K^+\Sigma^0$ separation is achieved and the gap in the Q^2 coverage between the FT and the CLAS12 Forward Detector calorimeters is the smallest. Studies of the reconstructed $e'K^+$ missing mass combining the data for the $K^+\Lambda$ and $K^+\Sigma^0$ channels for different torus field/polarity conditions are shown in Figs. 29 and 30. Clearly the data collection at the highest possible torus field settings, corresponding to the best charged particle momentum resolution, is optimal for separation of the KY reaction channels.

E_b, GeV	Tor. current, A	Q^2_{min}, GeV^2
6.6	+1500	0.05
6.6	−1500	0.05
6.6	+3700	0.05
6.6	**−3375**	0.05
8.8	+1500	0.1
8.8	−1500	0.1
8.8	+3700	0.1
8.8	**−3375**	0.1

Table 2: Minimal achievable Q^2 (Q^2_{min}) for different torus currents and polarities at E_b=6.6 GeV and 8.8 GeV for the $K^+\Lambda$ and $K^+\Sigma^0$ final states.

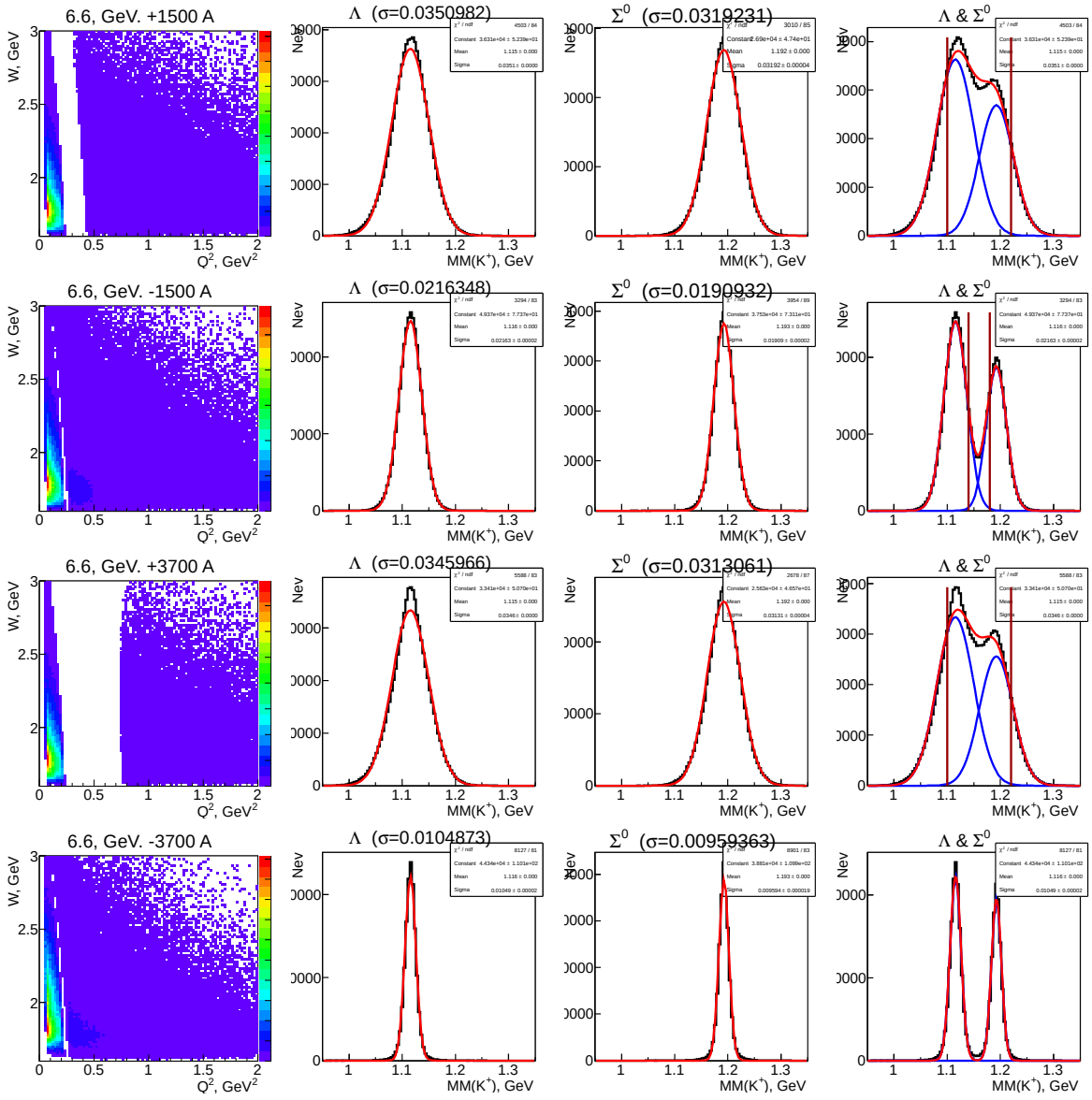

Figure 29: The left column shows the W versus Q^2 distributions at different torus currents for $Q^2 < 2$ GeV^2 for E_b=6.6 GeV. The next three columns show the distributions of the $e'K^+$ missing mass for the different torus currents. The right column shows the combined $K^+\Lambda$ and $K^+\Sigma^0$ overlaps (no background included) to demonstrate the requirement to take data at the highest possible CLAS12 torus setting.

6.4 Count Rates for $K^+\Lambda$

The expected total number of K^+Y electroproduction events in the reaction $ep \to e'K^+Y$ can be written as:

$$N = \mathcal{L} \cdot t \cdot \int \frac{d^5\sigma}{dE_e d\Omega_e d\Omega_K} dE_e d\Omega_e d\Omega_K, \tag{1}$$

where

- $\mathcal{L} = 1 \times 10^{35}$ cm^{-2}s^{-1} is the expected CLAS12 operating luminosity
- t is the expected run time, and
- $\frac{d^5\sigma}{dE_e d\Omega_e d\Omega_K}$ is the cross section from Eq.(21).

The integration in Eq.(1) is performed over the entire kinematic space and the event rate R is defined as $\frac{N}{t}$.

The integration in Eq.(1) can be done numerically. We use the same model cross sections for $d^2\sigma/d\Omega_K^*$ as was used in the event generator (see Section 6.1). The minimum achievable value of Q^2 in CLAS12 is determined by the forward hole, where high energy electrons cannot be detected. For all beam energies Q^2 is greater than 0.01 GeV^2, so we can integrate in Eq.(1) given that $Q^2 > 0.01$ GeV^2. The calculated event rates R_Λ and R_{Σ^0} are presented in Table 3.

E_{beam}, GeV	R_Λ, Hz	R_{Σ^0}, Hz
6.6	1500	1200
8.8	1400	1100

Table 3: Estimated production rates for events with $Q^2 > 0.01$ GeV^2.

To account for the acceptance of CLAS12, a detailed simulation is needed. As we need to generate events in the entire kinematic space with $Q^2 > 0.01$ GeV^2, the ratio of reconstructed to generated events gives the averaged acceptance. Multiplying the event rates from Table 3 by that ratio, we obtain the event rates that account for the CLAS12 acceptance. An $ep \to e'K^+\Lambda \to e'K^+p\pi^-$ event is considered to be reconstructed if the electron and at least two hadrons have been detected. A trigger condition requiring at least two charged hadrons and an electron would select our channels of interest.

The accepted event rate calculations are presented in Table 4 for different torus currents and polarities for E_b=6.6 GeV and 8.8 GeV, taking into account the branching ratio for the Λ decay into $p\pi^-$ (64%). A rough estimate suggests that the KY exclusive channel contribution is about 1% with respect to the two and three pion events, which are expected to dominate the events that have an electron and at least two charged hadrons in the final state. The maximal total event rate is therefore expected to be $\approx$ 25 kHz for the trigger condition described above. This estimate is compatible with the following considerations: suppose that the maximal inclusive event rate is 20 kHz, which is limited by the data acquisition. Then under the rough assumption that the $K^+\Lambda$ event rate is about 1% with respect to the inclusive event rate, we can estimate the $K^+\Lambda$ event rate to be $\approx$ 128 Hz. This number is in a reasonable agreement with the previously obtained value of 144 Hz.

E_{beam}, GeV	Torus Current A	R_Λ, Hz
6.6	+1500	144
6.6	-1500	154
6.6	+2950	87
6.6	-2950	72
8.8	+1500	108
8.8	-1500	108
8.8	+2950	67
8.8	-2950	52

Table 4: Estimated event rates for the $ep \to e'K^+\Lambda \to e'K^+p\pi^-$ channel where the electron and two hadrons are required to be detected.

6.5 Expected K^+Y Total Event Rates

At the very forward electron scattering angles, electron rates will be very high and may exceed the capabilities of the data acquisition system. Therefore additional constraints are needed to define an optimal trigger configuration to enrich the sample with final state topologies that might be expected for the hybrid baryon candidates and to reduce the total acquisition rate. For our initial running program, we therefore consider a trigger for the hadronic final states with at least two charged particles. This will cover final states: $K^+\Lambda \to K^+p\pi^-$, $p\pi^+\pi^-$, $p\phi \to pK^+K^-$, and $p\eta' \to p\pi^+\pi^-\eta$. For realistic rate estimates, projections of the hadronic coupling strengths of the hybrid baryons are needed, which are currently not available. In addition, a single charged hadron trigger will be incorporated with a pre-scaling factor for the FT, which in parallel will collect events with a single charged hadron in the final state, i.e. π^+n, $p\pi^\circ$, $K^+\Lambda$, and $K^+\Lambda$, among others.

The nominal operating luminosity of CLAS12 is expected to be $\mathcal{L} = 1 \times 10^{35}$ cm^{-2}sec^{-1}. This corresponds to a production rate of 70 Hz (for $K^+\Lambda$) and about 50 Hz (for $K^+\Sigma^0$). For a 30 day run at the nominal luminosity, the total number of $K^+\Lambda$ events is estimated to be 1.7×10^8 and the number of $K^+\Sigma^0$ events to be 1.2×10^8. The lowest event rate is expected for high Q^2 and high W. For the kinematics with lowest statistics, e.g. $2.0 \leq Q^2 \leq 2.5$ GeV^2 and $2.675 \leq W \leq 2.700$ GeV, a total number of 2.0×10^5 $K^+\Lambda$ events and 1.1×10^5 $K^+\Sigma^\circ$ events is expected.

While these rates seem very large, it should be kept in mind that the signals of the hybrid baryons that we want to detect and quantify may be one or two orders of magnitude smaller than the signal from ordinary baryon states and will likely not simply be seen as a peak in the excitation spectrum, but rather as a broad region in W where specific quantum numbers, i.e. $I = \frac{1}{2}$ and $J^P = \frac{1}{2}^+$ or $J^P = \frac{3}{2}^+$, must be identified and the electromagnetic couplings must be measured versus Q^2. This can be achieved in a partial-wave analysis that includes other channels in a multichannel fit, such as the Bonn-Gatchina or Jülich/GWU approaches. Other techniques may also be employed. Very high statistics is thus essential, and the transverse and longitudinal photon polarization that is inherent in electron scattering will provide amplitude interference that could be expected to enhance the resonant signal.

7 Data Analysis and Quasi-Data

7.1 Event Selection

Electrons will be detected both in the Forward Tagger and in the CLAS12 Forward Detector (FD). Electrons measured in the FD can be identified at scattering angles above 6° in the High-Threshold Cherenkov counter (HTCC) and in the PCAL and EC calorimeters. Due to the higher Q^2 for electrons detected at larger scattering angles in CLAS12 compared to the FT region, the FD electron rate is comparatively much lower than the hadronic rate, which ensures good electron identification.

For electrons detected in the FT, the low Q^2 leads to a very high electron rate that completely dominates the event rate in the FT calorimeter and hodoscope. A direct electron identification at the trigger level is therefore not needed. However the complete event pattern may be checked for consistency with that hypothesis in the event reconstruction. Note that the full electron kinematics is measured in the FT calorimeter and the micromegas tracker and charged particle ID is provided by the two layer hodoscope in front of the calorimeter as well as with hits in the micromegas tracker.

Charged hadrons ($\pi^{\pm}$, $K^{\pm}$, and protons) will be tracked in the drift chambers and micromegas in the FD, and in the silicon tracker and barrel micromegas at large angles in the CD. At all angles, charged particle identification is provided in the CLAS12 time-of-flight detector systems. Photons and neutrons are detected at forward angles in the electromagnetic calorimeters (PCAL, EC, FT) and neutrons at large angles are detected in the Central Neutron Detector (CND).

7.2 Event Reconstruction

The event reconstruction software has been designed and developed to be deployed within the ClaRA framework, a Service Oriented Architecture framework for data processing. The reconstruction application consists of a chain of services which can be deployed within ClaRA. The services for each detector component are compiled as java archive (JAR) plugins which are included in the complete CLAS12 Software release package coatjava. The CLAS12 reconstruction software reconstructs, on an event-by-event basis, the raw data coming from either simulation or the detectors to provide physics analysis output such as track parameters and particle identification. The package provides scripts that can be launched on the farm to cook the data as well as a framework to do event analysis using the flexible scripting language Groovy. The documentation for the coatjava package can available on the CLAS12 webpage [73]. For acceptance and efficiency studies, events are generated using the Geant-4 Monte Carlo simulation application GEMC. A detailed documentation of the detectors included in the simulation and of the various settings used to set the simulation parameters according to physics, backgrounds and magnetic field configurations is available from the gemc webpage [74]. An example of a simulated event for the reaction $ep \to e'K^+\Lambda$ is shown in Fig. 31.

At present, the reconstruction software is still in development. The components that are available are the Silicon Vertex Tracker (SVT), the Central Time of Flight (CTOF), the High Threshold Cherenkov Counter (HTCC), the Drift Chambers (DC), the Forward Time-Of-Flight (FTOF), the Electromagnetic and Pre-shower Calorimeters (EC/PCAL),

and the Forward Tagger Calorimeter and Hodoscope. A preliminary version for the Forward MicroMegas Tracker reconstruction is also available and is used to refit the track parameters coming from the DC.

An example of an event for the reaction $ep \rightarrow e'K^+\Lambda$ run through the reconstruction and displayed using the CLAS12 event display CED is shown in Figs. 32 and 33. An overall Event Builder takes the track momentum and flight path information obtained from Central and Forward tracking and links the track to the outer detector to obtain the responses and determine the PID. The electron is mostly identified by the Forward Tagger for the kinematics of the Hybrid Baryon proposal.

The studies for this letter of intent were done using FASTMC. For the proposal these studies will be repeated by generating events with the event generators described in section IV, tracking all particles through CLAS12 with GEMC and subsequently reconstructing these events with coatjava and obtaining the analysis selection criteria using the kinematic fitter available with the package.

An example of a reconstructed Λ mass spectrum obtained from the missing mass against the eK^+ in the reaction $ep \rightarrow e'K^+\Lambda$ generated with GEMC is shown in Fig. 34. The reconstruction uses only the electron detected in the Forward Tagger calorimeter and the produced K^+. Improved mass resolution is obtained when the Λ is reconstructed from the invariant mass of the proton and the π^-.

7.3 Extracting Differential Cross Sections and Normalized Yields

After the raw data have been subjected to the CLAS12 event reconstruction software package CLARA, we intend to extract differential cross section for all processes with two-body final states, e.g. KY, $N\pi$, $p\eta$, $p\eta'$, and $p\phi$ using simulations of large amounts of Monte Carlo events to fully understand the acceptances for these processes at the accuracy level required for the partial wave analysis. As for all electroproduction data, the raw cross sections will be subjected to radiative corrections in order to extract the fully corrected differential cross sections. The radiative correction procedure for exclusive processes is well established, and it has been used for correcting single π^+n and $p\pi^\circ$ production as well as $K^+\Lambda$ and $K^+\Sigma$ electroproduction employing the exact procedure developed in Ref. [75]. As it has been recently demonstrated [48], radiative corrections are very important for the analysis of exclusive processes in terms of resonance excitations as they affect both the polar and azimuthal angular dependencies, and consequently the partial wave analyses based on these processes.

For three-body final states, such as $p\pi^+\pi^-$ and $p\eta\pi^\circ$, in addition to extracting differential and integrated cross section, we also we consider event-based analysis techniques, where acceptances will be assigned to each event, and acceptance weighted events will be subjected to a maximum-likelihood fitting procedure. This procedures preserves the full correlations among the final state particles. more on how to separate the different cross sections components: σ_U, σ_{LT} and σ_{TT}

7.4 Partial Wave Analysis

Using modern partial wave analysis tools several new excited N^* and Δ^* states have been identified or have been significantly improved in their evidence and their star rating in the

2014 edition of the Review of Particle Properties (RPP) of the Particle Data Group [1]. The use of high statistics photoproduction data from CLAS of a number of final states, e.g. $K^+\Lambda$, $K^+\Sigma$, π^+n, $p\pi^\circ$, including polarization observables, was essential in establishing this new evidence. This success has also shown the importance of high statistics data sets in the search for new excited states, and has helped to re-vitalize the field of hadron spectroscopy. In the analysis of the data to be taken with the program discussed in this letter-of-intent, we will make full use of these advanced tools of amplitude and partial wave analysis. Significant progress has also been made in the analysis of electroproduction data where transition form factors have been extracted from several excited states using the high statistics data from CLAS [5, 4, 48]. We expect that these data analysis packages will be well-honed by the time the proposed data will be taken, including the extension of the photoproduction analysis to include the existing and planned electroproduction data sets.

7.5 Modeling Hybrid Baryon Contributions to KY and $\pi^+\pi^-p$

To prove the feasibility of our ability to observe hybrid baryons, we have studied the effect of implementing the contribution of the lightest hybrid state in the differential cross sections for exclusive $K^+\Lambda$, $K^+\Sigma^0$, and $\pi^+\pi^-p$ electroproduction off the proton. For the hybrid baryon mass range and spin-parity, we have considered Lattice QCD evaluations [6] that predict the lightest hybrid baryons in a mass range from 2.5 GeV to 2.7 GeV with spin-parity either $J^P = \frac{1}{2}^+$ or $J^P = \frac{3}{2}^+$ (see Fig. 1). However, these computations were carried out with a pion mass of 396 MeV. We have corrected the predicted hybrid baryon masses by employing mass shifts for states of both spin-parities towards smaller values, which can be expected when the physical pion mass will be reached. The mass shift for the lowest hybrid baryon with $J^P = \frac{1}{2}^+$ spin-parity can be estimated by the difference between the LQCD result [6] for the mass of the lightest nucleon of spin-parity $J^P = \frac{1}{2}^+$ and the measured value of the proton mass, Δ_1=0.3 GeV. For the lowest hybrid state with $J^P = \frac{3}{2}^+$, the mass shift can be estimated by the differences between the mass of the lightest LQCD resonance with $J^P = \frac{3}{2}^+$ and the physical mass of the $N(1720)\frac{3}{2}^+$ four star resonance, Δ_2=0.5 GeV.

Therefore, we have modeled the hybrid baryon contributions considering states of spin-parity $J^P = \frac{1}{2}^+$ and $J^P = \frac{3}{2}^+$ in the mass range from 2.1 GeV to 2.3 GeV employing an average mass shift of 0.4 GeV. Eventually we used the central value of 2.2 GeV for the hybrid state mass. According to the RPP14 results [1] on the resonance parameters in the mass range around 2.0 GeV, we adopted for the hybrid baryon total decay width a range from 200 MeV to 300 MeV. For the hybrid branching ratio (BR) to KY we employed the value of 5%. Recent studies of the CLAS data on $\pi^+\pi^-p$ electroproduction [28] demonstrated that many of nucleon resonances in the mass range above 1.6 GeV decay preferentially to the $N\pi\pi$ final state and most of them have the branching ratios to the $N\pi\pi$ final state above 40%. We therefore chose for the hybrid baryon branching ratio to the $N\pi\pi$ final state the value of 50%.

The differential cross sections without hybrid contributions (Model A) were computed from the amplitudes of the RPR model [12, 58] for KY exclusive channels and from the JM model [34, 72, 71, 11, 13, 28] for the $\pi^+\pi^-p$ exclusive channel. Both models contain the contributions from four star resonances and the non-resonant mechanisms added-up coherently:

- in the case of the KY channel we considered as a reference the RPR model referred to as RPR-2011 [12, 76], in which the Reggeized non-resonant amplitudes and the contributions from the established N^* states have been used to describe both KY photo- and electroproduction. The RPR web-site [77] provides the full set of KY amplitudes and photo-/electroproduction observables off the proton.

- in the case of the $\pi^+\pi^- p$ channel, we considered the coherent superposition of 8 meson-baryon channels and direct 2π-production mechanisms described in Section 3.3 with the contributions to the $\pi\Delta$ and ρp meson-baryon channels from all four star resonances with observed decays to the $N\pi\pi$ final state [34, 72, 71, 11, 13, 28].

In the evaluation of the cross sections accounting for the hybrid contribution (Model B), the hybrid resonance amplitude was added coherently to the aforementioned amplitudes of KY and $\pi^+\pi^- p$ electroproduction. The full amplitudes of the KY and $\pi^+\pi^- p$ exclusive channels $\langle \lambda_f | \, T^B \, | \lambda_\gamma \lambda_p \rangle$ in Model B were evaluated as:

$$\langle \lambda_f | \, T^B \, | \lambda_\gamma \lambda_p \rangle = \langle \lambda_f | \, T^A \, | \lambda_\gamma \lambda_p \rangle + F_{conv} \, \langle \lambda_f | \, T^r \, | \lambda_\gamma \lambda_p \rangle \, , \tag{2}$$

where the $\langle \lambda_f | \, T^A \, | \lambda_\gamma \lambda_p \rangle$ matrix element represents the full Model A amplitudes without hybrid contribution, while the hybrid contribution was described by the resonant amplitude $\langle \lambda_f | \, T^r \, | \lambda_\gamma \lambda_p \rangle$. The amplitudes were computed in the helicity representation with the helicities of the initial virtual photon and proton λ_γ, λ_p, and the final state helicity λ_f determined in the CM frame, as well as the four momenta of the final hadrons and the initial virtual photon and proton.

The relations between the model amplitudes and the cross sections for the KY and $\pi^+\pi^- p$ channels can be found in Ref. [12, 58] and Ref. [11], respectively. However, the resonant amplitudes described below for the hybrid contributions were obtained in the conventions of the JM model that relate the $\pi^+\pi^- p$ amplitudes to the cross sections. Therefore in the case of the KY cross section evaluation within the RPR model, the $\langle \lambda_f | \, T^r \, | \lambda_\gamma \lambda_p \rangle$ resonant contributions from the hybrid should be converted to the convention of the RPR model that relate the RPR model amplitudes to the cross sections. This was achieved by employing the conversion factor F_{conv} in Eq.(2). The F_{conv} conversion factor from the JM model to the RPR model was evaluated by making an identity between the cross sections computed in both models:

$$F_{conv} = \sqrt{4\pi\alpha}, \tag{3}$$

where $\alpha = \frac{1}{137}$. This factor is employed in the computations of the KY differential cross sections within the RPR model, while in the computation of the $\pi^+\pi^- p$ differential cross sections within the framework of the JM model, the factor F_{conv} is equal to unity.

The contributions from the hybrid baryon were parameterized employing the unitarized Breit-Wigner ansatz developed in Ref. [13]. For simplicity here we restrict ourselves to consideration of the Breit-Wigner ansatz for the KY final states treating the final hadrons as stable particles. The description of the Breit-Wigner ansatz used in simulation of the $\pi^+\pi^- p$ channel accounting for the formation and decays of unstable $\pi\Delta$ and ρp intermediate states can be found in Ref. [13]. As discussed in Ref. [13], for just one contributing resonance the unitarized Breit-Wigner ansatz can be simplified as:

$$\langle \lambda_f |\, T^r \,| \lambda_\gamma \lambda_p \rangle = \frac{\langle \lambda_f |\, T_{dec} \,| \lambda_R \rangle \, \langle \lambda_R |\, T_{em} \,| \lambda_\gamma \lambda_p \rangle}{M_r^2 - W^2 - i \Gamma_r M_r}. \tag{4}$$

The resonant amplitude represents the product of the $\langle \lambda_R |\, T_{em} \,| \lambda_\gamma \lambda_p \rangle$ and $\langle \lambda_f |\, T_{dec} \,| \lambda_R \rangle$ photoexcitation and hadronic decay amplitudes, respectively, and the Breit-Wigner propagator for the s-channel hybrid resonance of mass M_r and total decay width Γ_r. The hybrid electroexcitation amplitude is fully determined by the four-momenta of the initial photon and proton in the CM frame and their helicities. With the quantization axis Oz directed along the four-momentum of the initial photon, the hybrid spin projection to the Oz axis λ_R is determined by angular momentum conservation, $\lambda_R = \lambda_\gamma - \lambda_p$.

The photoexcitation $\langle \lambda_R |\, T_{em} \,| \lambda_\gamma \lambda_p \rangle$ and hadronic decay $\langle \lambda_f |\, T_{dec} \,| \lambda_R \rangle$ amplitudes are related to the two resonance photocouplings $A_{1/2}$ and $A_{3/2}$, and the partial hadronic decay widths to the KY final state Γ_{λ_f} of helicity λ_f, where $\lambda_f = -\lambda_Y$.

In order to relate the hybrid hadronic decay amplitude $\langle \lambda_f |\, T_{dec} \,| \lambda_R \rangle$ to the partial hadronic decay widths to the KY final state Γ_{λ_f} of helicity λ_f, we can rotate the quantization axis adopted for the initial-state $|\lambda_R\rangle$ wave function and re-evaluate the matrix element $\langle \lambda_f |\, T_{dec} \,| \lambda_R \rangle$ in the frame with the quantization axis $0z'$ for the final KY state. The matrix element $\langle \lambda_f |\, T_{dec} \,| \lambda_R \rangle$ after rotation becomes:

$$\langle \lambda_f |\, T_{dec} \,| \lambda_R \rangle = \sum_{\nu'} \langle \lambda_f | T_{dec} | J_r \; \nu' \rangle d^{J_r}_{\lambda_R \nu'}(\cos\theta_K) e^{i\mu\phi_K}. \tag{5}$$

The superposition of the states $|J_r \; \nu'\rangle$ in Eq.(5) with spin J_r and its projection onto the final-state quantization axis ν', is the transformed wave function of the initial-state $|\lambda_R\rangle$ after the aforementioned rotation of the initial-state quantization axis Oz. Lorentz invariance of the resonance hadronic decay amplitudes requires that the operator T_{dec} should be an SU(2) $\otimes$ O(3) - spin $\otimes$ orbital momentum scalar. Only the term with $\nu' = \lambda_f$ in Eq.(5) remains non-zero in the sum of Eq.(5), as a consequence of the Wigner-Eckart theorem applied to the matrix elements $\langle \lambda_f | T_{dec} | J_r \; \nu' \rangle$ with the scalar T_{dec} operator. The $\langle \lambda_f | T^{J_r}_{dec} | \lambda_f \rangle$ matrix elements in Eq.(5) are determined by the final-state helicity λ_f only, and are independent of resonance helicities λ_R. Assuming real values for the matrix element $\langle \lambda_f | T_{dec} | \lambda_f \rangle$, we can relate it to the Γ_{λ_f} partial hadronic decay width of the hybrid state to the final KY state of helicity λ_f Γ_{λ_f}. We employ general relations of quantum theory between the resonance decay amplitude $\langle \lambda_f | T_{dec} | \lambda_R \rangle$ of Eq.(5), the two-body state phase space of resonance decay products $d\Phi_{2b}$ in the conventions of the JM model [13], and the Γ_{λ_f} decay width:

$$\Gamma_{\lambda_f} = \frac{1}{2M_r} \frac{1}{2J_r + 1} \sum_{\lambda_R} \int |\langle \lambda_f | T_{dec} | \lambda_R \rangle|^2 d\Phi_{2b}, \tag{6}$$

with the final-state two-body phase space $d\Phi_{2b}$:

$$d\Phi_{2b} = \frac{1}{4\pi^2} \frac{p_f}{4M_r} \sin\theta d\theta d\phi. \tag{7}$$

Inserting Eqs.(5) and (7) into Eq.(6), and accounting for the d-function normalization,

$$\int d^J_{\mu\,\nu}(\cos\theta) \cdot d^J_{\mu\,\nu}(\cos\theta) \sin\theta d\theta = \frac{2}{2J+1}, \tag{8}$$

we obtain for the $\langle\lambda_f|T_{dec}|\lambda_f\rangle$ amplitudes:

$$\langle\lambda_f|T_{dec}|\lambda_f\rangle = \frac{2\sqrt{2\pi}\sqrt{2J_r+1}M_r\sqrt{\Gamma_{\lambda_f}}}{\sqrt{p_f^r}}. \tag{9}$$

The amplitudes $\langle\lambda_f|T_{dec}|\lambda_f\rangle$ are evaluated at the resonant point $W = M_r$. However, in calculations of the resonant cross sections for $W \neq M_r$, the two-body phase space becomes different than that at the resonant point. The factor $\sqrt{\frac{p_f^r}{p_f}}$, where p_f^r and p_f represent the magnitudes of the three momentum of K in the CM-frame at the resonant point and the current W, respectively, is needed to account for this difference and to evaluate the resonant cross sections and amplitudes for W values away from the resonant point, resulting in the following equation for the hybrid hadronic decay amplitude $\langle\lambda_f|T_{dec}|\lambda_f\rangle$:

$$\langle\lambda_f|T_{dec}|\lambda_f\rangle = \frac{2\sqrt{2\pi}\sqrt{2J_r+1}M_r\sqrt{\Gamma_{\lambda_f}}}{\sqrt{p_f^r}}\sqrt{\frac{p_f^r}{p_f}}. \tag{10}$$

The helicity matrix elements of T_{em} are given in terms of two independent photocouplings, $A_{1/2}$ and $A_{3/2}$, which are related to the matrix elements with net helicity $\lambda_R = \lambda_\gamma - \lambda_p = 1/2,\ 3/2$, respectively. The other two helicity states are related by parity. These photocouplings are unambiguously defined through their relation to the N^* electromagnetic decay width Γ_γ:

$$\Gamma_\gamma = \frac{E_{\gamma,r}^2}{\pi}\frac{2M_N}{(2J_r+1)M_r}\left[\left|A_{1/2}\right|^2 + \left|A_{3/2}\right|^2\right], \tag{11}$$

where $q_{\gamma,r}$ is the three-momentum modulus of the photon at $W = M_r$ in the CM frame.

The transition amplitudes $\langle\lambda_R\,|T_{em}|\,\lambda_\gamma\lambda_p\rangle$ are related to the $A_{1/2}$ and $A_{3/2}$ photocouplings by imposing the requirement that the BW parametrization [78] of the resonant cross section for a single contributing resonance should be reproduced:

$$\sigma(W) = \frac{\pi}{E_\gamma^2}(2J_r+1)\frac{M_r^2\Gamma_i(W)\Gamma_\gamma}{(M_r^2-W^2)^2 - M_r^2\Gamma_r^2}. \tag{12}$$

In this way we obtain the following relationship between the $\langle\lambda_R\,|T_{em}|\,\lambda_\gamma\lambda_p\rangle$ transition amplitudes and the $\gamma_v NN^*$ electrocouplings:

$$\langle\lambda_R\,|T_{em}|\,\lambda_\gamma\lambda_p\rangle = \frac{W}{M_r}\sqrt{\frac{8M_N M_r q_{\gamma_r}}{4\pi\alpha}}\sqrt{\frac{q_{\gamma_r}}{q_\gamma}}A_{1/2,3/2}. \tag{13}$$

The factor $4\pi\alpha$ in Eq.(13) reflects the particular relationship between the JM model amplitudes and cross sections, when the absolute value of the electron charge is factorized out of the production amplitudes.

The differential cross sections were computed from the amplitudes of Eq.(2) for the KY electroproduction employing the relations from Refs. [12, 58] and for the $\pi^+\pi^- p$ electroproduction employing the relations from Ref. [11]. In order to examine the feasibility of observing a hybrid baryon signal, we have computed the differential cross sections for the aforementioned exclusive channels in Model A (without hybrid) and model B (implementing

hybrid). The computations within Model B were carried out with variable values of the hybrid baryon electrocouplings. For the statistical uncertainties expected in the experimental data, we compared the cross sections in Model A and Model B and determined the minimal values of the hybrid baryon electrocouplings above which the difference between the cross sections become statistically significant.

In our approach we compared the differential cross sections with and without the hybrid point-by-point in several bins over Q^2 and within the interval 2.1 GeV $< W <$ 2.3 GeV. In this way, we established the minimal values of the hybrid electroexcitation amplitudes at different Q^2 above which the signal from the hybrid will be statistically significant and therefore can be observed in the data. For comparison of the differential cross sections computed in Models A and B, we are using $\chi^2/d.p.$ as a measure for the evaluation of the statistical significance of the cross section difference. In the extraction of the resonance electrocouplings from $N\pi$ and $\pi^+\pi^-p$ electroproduction data measured with CLAS, the data description within the reaction model was treated as acceptable for $\chi^2/d.p. < 3$. Therefore, we consider the hybrid signal as statistically significant if the comparison of the differential cross sections computed within Models A and B results in $\chi^2/d.p. > 4$. In this way we take into account any systematic uncertainties related to the use of the reaction model of limited accuracy in reproducing the experimental data.

7.6 Threshold Values for Hybrid Baryon Couplings in $\pi^+\pi^-p$

In order to examine the feasibility to observe a signal from a hybrid baryon in exclusive $\pi^+\pi^-p$ electroproduction, we have computed the following four one-fold differential cross sections:

- invariant mass distributions $d\sigma/dM_{\pi^+\pi^-}$ and $d\sigma/dM_{\pi^+p}$ for two pairs ($\pi^+\pi^-$ and $p\pi^+$) of the final state particles;
- angular distributions $d\sigma/d(-\cos\theta_{\pi^-})$ for the final state π^- in the CM frame;
- angular distributions $d\sigma/d\alpha_{[p'\pi^+][p\pi^-]}$ over the rotational angle α of the plane composed by the three-momenta of the final state p' and π^+ around the direction of the π^- momentum in the CM frame with respect to the plane composed by the three momenta of the initial p and the final π^-.

Each of these cross sections was computed at Q^2=0 GeV^2, 0.65 GeV^2, and 1.30 GeV^2 by integrating the five-fold differential $\pi^+\pi^-p$ cross sections as described in Ref. [28]. The five-fold differential $\pi^+\pi^-p$ cross sections were obtained from the amplitudes of the JM model with (Model A) and without the hybrid state (Model B), employing the relations between the amplitudes and the five-fold differential cross sections from the Appendices of Ref. [11]. The implementation of the hybrid baryon into the full amplitude of the JM model was outlined in Section 7.5. The computations of the one-fold differential cross sections within Model A were carried out for a hybrid baryon of spin-parity $J^P = \frac{1}{2}^+$, with the hadronic parameters described in Section 7.5 and for variable values of the $A_{1/2}(Q^2)$ hybrid electrocouplings in the range from 0 GeV$^{-1/2}$ to 0.150 GeV$^{-1/2}$ with $S_{1/2}(Q^2) = 0$.

The hybrid baryon signal should be seen in the difference of the one-fold differential cross sections computed with and without the hybrid. The statistical significance of the signal is quantified in terms of $\chi^2/d.p.$ estimated as:

$$\chi^2/d.p. = \frac{1}{N_{d.p.}} \sum_{W_i} \sum_{\substack{X=m_{\pi^+\pi^-}, m_{\pi^+p}, \\ \theta_{\pi^-}, \alpha_{\pi^-}}} \frac{\left(\frac{d\sigma_{nohyb}}{dX} - \frac{d\sigma_{hyb}}{dX}\right)^2}{\left(\varepsilon_{hyb} \frac{d\sigma_{hyb}}{dX}\right)^2}. \quad (14)$$

The $\frac{d\sigma_{hyb/nohyb}}{dX}$ values represent the one-fold differential cross sections with and without the hybrid contribution, while dX represent the differentials for the four one-fold differential cross sections listed above. We have assigned statistical uncertainties ε_{hyb} expected with the run conditions described in Section 5 to the differential cross sections of Model A, while the differential cross sections computed in Model B were treated as the fit curves known exactly from the model. Only the expected statistical uncertainties are included into the evaluation of the statistical significance of the one-fold differential cross section differences in Eq.(14). The internal sum runs over all of the quasi-data points of the four one-fold differential cross sections, computed in each bin of W and Q^2 on the grid consisting of 16 (12) bins over the final state hadron invariant masses and 14 (6) bins over the CM angles θ_{π^-} and α_{π^-} for the photoproduction (electroproduction) reaction. The external sum in Eq.(14) runs over all 25-MeV-wide W bins from 2.1 GeV to 2.3 GeV. The total number of the quasi-data points $N_{d.p.}$ involved in the studies at each Q^2 point is equal to 420 for photoproduction and 252 for electroproduction.

The statistical uncertainties of the one-fold differential cross sections with the hybrid state were chosen to be the following: 3% at $Q^2 = 1.3$ GeV^2, 2% at $Q^2 = 0.65$ GeV^2, and 1% at $Q^2 = 0$ GeV^2. The statistical uncertainties at Q^2=1.3 GeV^2 were estimated based on the comparison with the statistical uncertainties of the data from our previous CLAS experiment collected at the bin centered at Q^2=1.3 GeV^2 [47]. The statistical uncertainties of the expected data were estimated accounting for the differences between the integrated luminosity and the virtual photon fluxes of both experiments, the ratio of the efficiencies for the topology with all three final state hadrons detected (conservative evaluation), and for the differences in the data binning over the kinematic grids. The statistical uncertainties for the data in other two Q^2 bins were obtained by multiplying the uncertainties at Q^2=1.3 GeV^2 by the root square from the ratio of the fully integrated cross sections at the given Q^2 value to that at Q^2=1.3 GeV^2.

The $\chi^2/d.p.$ values were evaluated independently for the different values of the $A_{1/2}$ electrocouplings in each of the three Q^2 bins. As explained in Section 7.5, we assumed that the hybrid signal will be statistically significant if $\chi^2/d.p > 4$, taking into account the final accuracy of the reaction models in reproducing the experimental data. The minimal absolute values of the hybrid $A_{1/2}(Q^2)$ electrocouplings obtained in this way, above which the signal from the hybrid becomes statistically significant in the data on the four one-fold $\pi^+\pi^- p$ differential cross sections, are listed in Table. 5 The electrocoupling values that make the hybrid signal statistically significant are comparable with those for most conventional nucleon resonances. Therefore, the proposed experiment offers a promising prospect for the observation of any new hybrid baryon states in the exclusive $\pi^+\pi^- p$ electroproduction reaction.

Q^2 (GeV^2)	0.	0.65	1.3
$A_{1/2} \times 10^{-3}$ (GeV$^{-1/2}$)	45	37	19

Table 5: Threshold values for the $A_{1/2}$ electrocouplings for a statistically distinguishable hybrid state signal.

Representative examples for the ratio F_x of the difference between the one-fold differential cross sections estimated in Models A and B over the differential cross section from Model A are shown in Figs. 35 and 36 at W=2.19 GeV and Q^2=0 GeV^2 and 0.65 GeV^2. These ratio were obtained with the $A_{1/2}(Q^2)$ hybrid electrocoupling values listed in Table 5. Statistically significant signals from the hybrid baryon are evident in the kinematic dependencies of all four one-fold differential cross sections. The most pronounced signals from the hybrid are expected in the ρ peak in the $d\sigma/dM_{\pi^+\pi^-}$ mass distributions and in the two CM angular distributions. In Fig. 37 we show the Q^2 evolution of the ratio F_x for the CM angular distributions $d\sigma/d(-\cos\theta_{\pi^-})$ (left) and $d\sigma/d\alpha_{[p'\pi^+][p\pi^-]}$ (right). The ratio F_x for both angular distributions increases with Q^2, offering a promising opportunity to explore the Q^2 dependencies of the hybrid resonance in a relatively wide Q^2 range. This feature is of particular importance in order to establish the hybrid nature of any new baryon state based on peculiarities seen in the Q^2 behavior of its electrocouplings.

Finally, we note that all estimates presented above for the feasibility of observing a hybrid signal were conservative. The conditions for hybrid baryon observation in exclusive $\pi^+\pi^- p$ electroproduction can be further improved by:

- collecting the $\pi^+\pi^- p$ events in a topology with only two final state hadrons detected in CLAS12, while the four-momenta of the third hadron is reconstructed from energy-momentum conservation. This topology is preferential for optimizing the counting rates but leads to worse resolution for the final hadron invariant mass W;
- employing a trigger with two positive final state hadrons in coincidence with the scattered electron, allowing us to increase the percentage of $\pi^+\pi^- p$ events in the data sample. However, such a restrictive trigger may give rise to problems for the simultaneous running of several experiments;
- incorporating into the physics analysis the LT, TT, and LT' interference structure functions for the exclusive $\pi^+\pi^- p$ electroproduction.

7.7 Threshold Values for Hybrid Baryon Couplings in KY

In order to quantify the statistical significance of the difference between the exclusive KY event distributions over the θ_K, ϕ_K CMS angles, simulated according to the models A and B, as described in paragraph 7.5, the following χ^2 definition has been be used:

$$\chi^2 = \frac{1}{N_{d.p.}} \sum_{W,\cos(\theta_K),\phi_K} \frac{\left(\frac{d^2\sigma_A}{d\Omega_K} - \frac{d^2\sigma_B}{d\Omega_K}\right)^2}{\delta^2}, \tag{15}$$

where $\frac{d^2\sigma_A}{d\Omega_K}$ and $\frac{d^2\sigma_B}{d\Omega_K}$ are the cross sections simulated in the models A and B, respectively.

The χ^2 is evaluated in each Q^2 bin independently and we choose a 0.1 GeV^2 bin width in Q^2. The sum over W in (15) runs from $M_R - \Gamma_R/2$ to $M_R + \Gamma_R/2$ and the bin width in W is 20 MeV. We used 24 bins in $\cos(\theta_K)$ and ϕ_K. Assuming that the statistical uncertainties dominate, the uncertainties for the differences $\left(\frac{d^2\sigma_A}{d\Omega_K} - \frac{d^2\sigma_B}{d\Omega_K}\right)$ between the event distributions simulated in the models B and A, respectively, can be evaluated as:

$$\delta^2 = \left(\frac{\frac{d^2\sigma_A}{d\Omega_K}}{\sqrt{N_A}}\right)^2 + \left(\frac{\frac{d^2\sigma_B}{d\Omega_K}}{\sqrt{N_B}}\right)^2 , \tag{16}$$

where N_A and N_B are the number of events in three dimensional bins in W and Ω_K for the two models.

The number of events in the mentioned above three dimensional bins for a given Q^2 bin can be calculated knowing the expected total number of events in the whole covered kinematic space. The number of events in each multidimensional bin is proportional to the cross section in that bin, taking acceptance into account. The cross section $\frac{d^2\sigma}{d\Omega_K}$ are obtained by integrating over the other kinematic variables: final state electron azimuthal angle ϕ_e and spherical angles of one of the Λ decay product particles, say proton, θ_p, ϕ_p, assuming that the cross section $\frac{d^5\sigma}{d\Omega_K d\phi_e d\theta_p d\phi_p}$ does not depend on ϕ_e, θ_p and ϕ_p. Then the number of events (N) in every four dimensional bin is

$$N(Q^2, W, \theta_K, \phi_K) = C \int_{\phi_e,\theta_p,\phi_p} a \times \frac{d^5\sigma}{d\theta_K d\phi_K d\phi_e d\theta_p d\phi_p} = C \int_{\phi_e,\theta_p,\phi_p} a \times \frac{d^2\sigma}{d\Omega_K} \approx C \sum_{\phi_e,\theta_p,\phi_p} a \times \frac{d^2\sigma}{d\Omega_K} , \tag{17}$$

where a is the CLAS12 acceptance, which depends on all kinematic variables and C is a constant. Set the sum of all $N(Q^2, W, \theta_K, \phi_K)$ equal to the expected total number of events in the whole kinematic covered space we find the constant C.

The number of evens in each multidifferential bin was calculated assuming the total number of $K\Lambda$ events to be collected in the experiment is 2×10^8 (see Section 6.4).

The typical number of events in one bin of the single differential distribution $\frac{d\sigma}{d\cos(\theta_K)}$ is about few thousands and the statistical uncertainties are negligible, while in two fold differential distribution $\frac{d^2\sigma}{d\Omega_K}$ statistical uncertainties are meaning. This can be seen in Figs. 38 through 41

We define the the minimal value of the photocoupling such as it is the minimal value of the photocoupling when the χ^2 from (15) characterizing the difference between two cross sections is more than 4. The minimal values of A_{12}, A_{32} and S_{12} found in this way are presented in Tables 6 and 7. The mass of the hybrid state was 2.2 GeV and the total width was 0.250 GeV. The Q^2 bin width was 0.1 GeV^2.

It was found that the minimal photocoupling values are weakly dependent on the run conditions and Q^2. The weak dependence on Q^2 can be explained. The resonance manifestation is more pronounced at small Q^2, as the non-resonant background is smaller, on the other hand statistical uncertainties are larger (the same Q^2 bin width (0.1 GeV^2) is used at all Q^2) and the sensitivity to the resonance gets smaller. These two factors work in opposite direction and the χ^2 does not change significantly.

Q^2, GeV^2	J_R=1/2		J_R=3/2		
	A_{12}	S_{12}	A_{12}	A_{32}	S_{12}
0.1	12	12	16	11	10
0.5	17	19	18	19	12
1.0	16	21	16	18	10

Table 6: The minimal values of the photocouplings for the beam energy 6.6 GeV and the torus current -2950 A for the resonances with the spin (J_R) 1/2 and 3/2. $A_{1/2}$, $A_{3/2}$ and $S_{1/2}$ are in units of $10^{-3}\times$GeV$^{-1/2}$. When determining the minimal value of $A_{1/2}$ we varied only $A_{1/2}$ setting the other photocouplings to zero. The minimal values of $A_{3/2}$ and $S_{1/2}$ were obtained in the same way.

Q^2, GeV^2	J_R=1/2		J_R=3/2		
	A_{12}	S_{12}	A_{12}	A_{32}	S_{12}
0.3	12	12	14	12	9
0.5	19	20	19	21	12
1.0	16	21	16	18	9

Table 7: The minimal values of the photocouplings for the beam energy 8.8 GeV and the torus current -2950 A for the resonances with the spin (J_R) 1/2 and 3/2. $A_{1/2}$, $A_{3/2}$ and $S_{1/2}$ are in units of $10^{-3}\times$GeV$^{-1/2}$. When determining the minimal value of $A_{1/2}$ we varied only $A_{1/2}$ setting the other photocouplings to zero. The minimal values of $A_{3/2}$ and $S_{1/2}$ were obtained i n the same way.

Figs. 38 through 41 present examples of the comparison of the model to the model plus resonance one- and two fold differential cross sections. The model plus resonance cross section was calculated when the photocoupling was set to its minimal value from the Table 7.

7.8 Search for Hybrid Baryons from Moment Expansion

.

The analysis using the Legendre moments proved to be a good way to distinguish signal from background. Legendre moments are defined as:

$$P_m = \frac{2m+1}{2} \int_{-1}^{1} L_m d\sigma(x)_i dx \tag{18}$$

where

$$x = \cos\theta_k^*$$
$$L_m(x) = \sum_{j=0}^{m} a_{mj} x^j$$
$$a_{mj} = (-1)^{(m-j)/2} \frac{1}{2^m} \frac{(m+j)!}{(\frac{m-j}{2})!(\frac{m+j}{2})!j!}$$
$$m - j = even$$

$d\sigma(x)_i$, with $i = T,\ L,\ TT$ and LT, represent the transverse, longitudinal and interference structure functions, which depend on the variables W, Q^2 and θ_k^*.

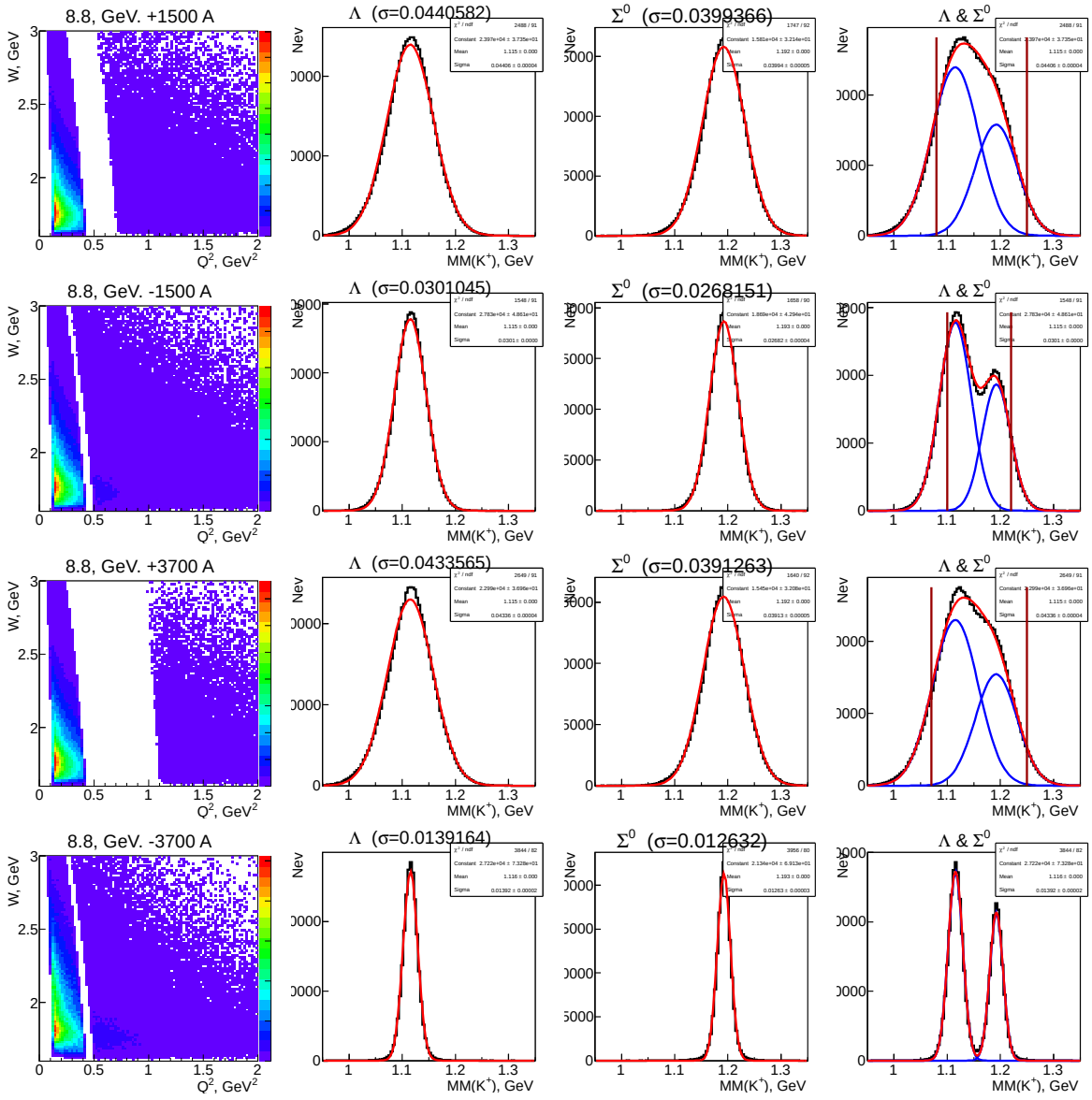

Figure 30: The left column shows the W versus Q^2 distributions at different torus currents for $Q^2 < 2$ GeV^2 for E_b=8.8 GeV. The next three columns show the distributions of the $e'K^+$ missing mass for the different torus currents. The right column shows the combined $K^+\Lambda$ and $K^+\Sigma^0$ overlaps (no background included) to demonstrate the requirement to take data at the highest possible CLAS12 torus setting.

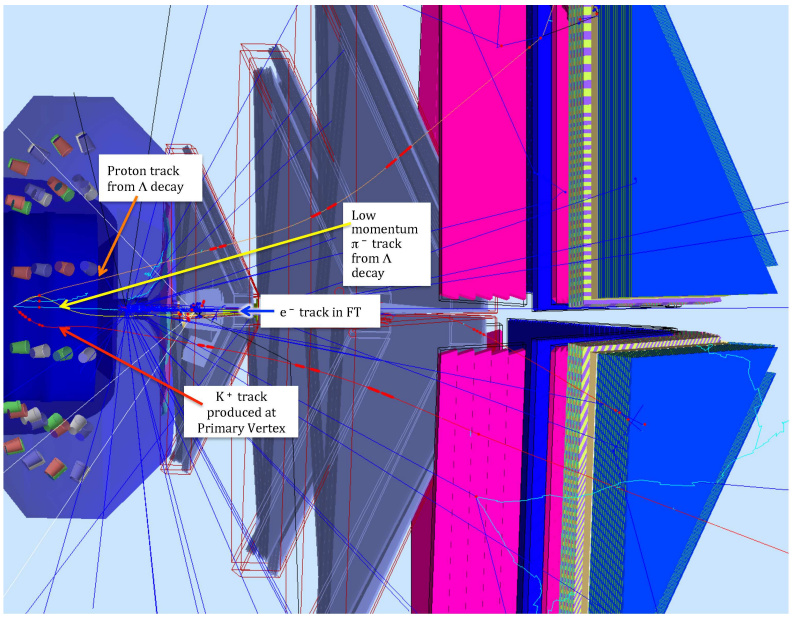

Figure 31: GEMC - Graphical User Interface Display of $ep \rightarrow e'K^+\Lambda$ ($\Lambda \rightarrow p\pi^-$) event as seen in CLAS12 detectors.

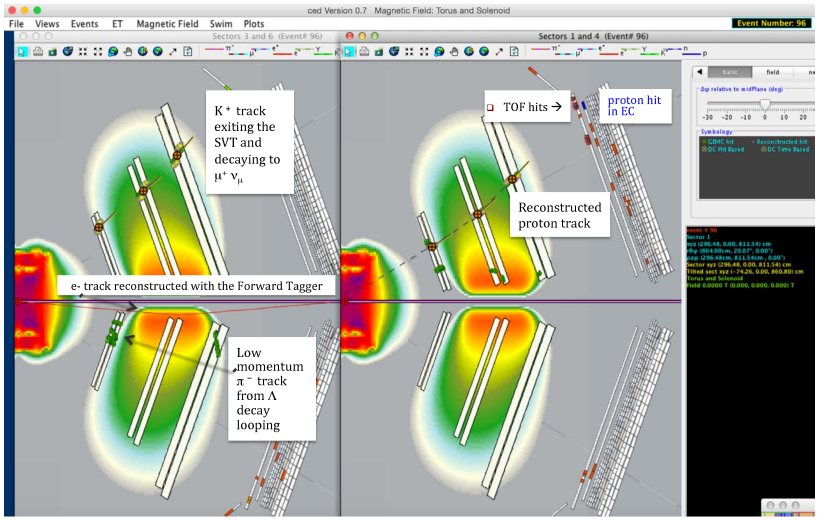

The e- and proton tracks from the reaction $e^-p \rightarrow e^{-\prime} K^+\Lambda$, $\Lambda \rightarrow p\pi^-$ reconstructed in the Forward Detectors

- The filled orange circles correspond to reconstructed 3-D points obtained from pattern recognition; the tangent to the reconstructed track at the 3-D point is represented by the line segment connected to the filled circle.
- The dashed line corresponds to tracks swam to z = 0 with the parameters extracted from the reconstruction algorithm

Figure 32: Event display for the reaction $ep \rightarrow e'K^+\Lambda$.

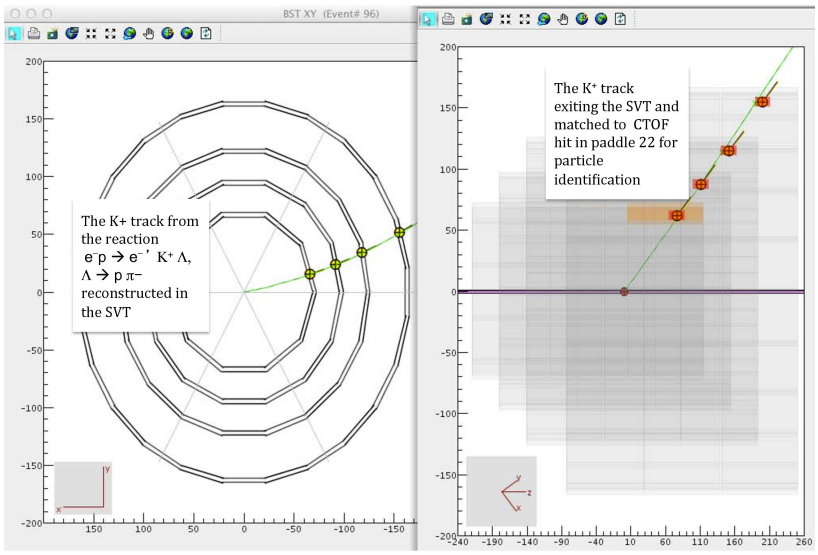

Figure 33: Event display for the reaction $ep \rightarrow e'K^+\Lambda$.

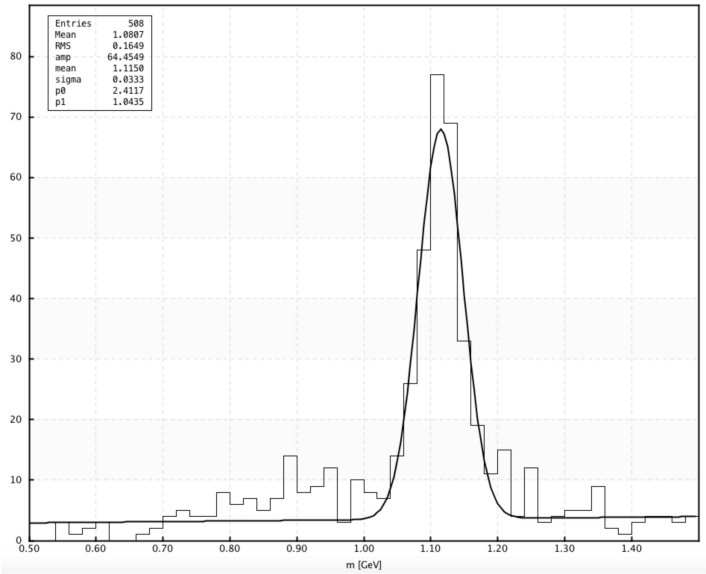

The m.m.(e⁻' K⁺) distribution from the reaction e⁻p → e⁻' K⁺ Λ, Λ → p π− reconstructed using the coatjava package.

Figure 34: Reconstructed Λ mass distribution obtained from the recoil mass against the e' and K^+ for the reaction $ep \rightarrow e'K^+\Lambda$ at a beam energy of 6.6 GeV. This figure is obtained using the coatjava plotting package (under development).

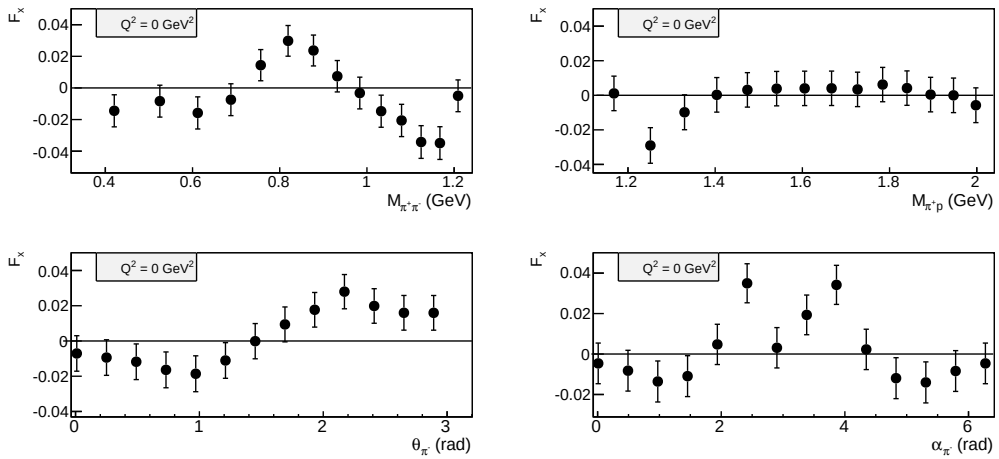

Figure 35: The ratio F_x (see Section 7.6) for the relative differences between the four one-fold differential $\pi^+\pi^-p$ cross sections at Q^2=0 GeV^2 computed with and without a hybrid baryon contribution.

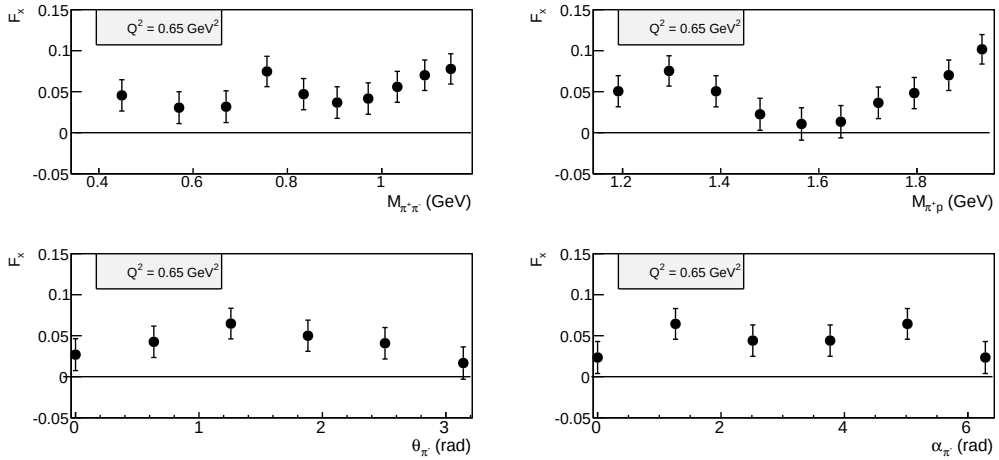

Figure 36: The ratio F_x (see Section 7.6) for the relative differences between the four one-fold differential $\pi^+\pi^-p$ cross sections at Q^2=0.65 GeV^2 computed with and without a hybrid baryon contribution.

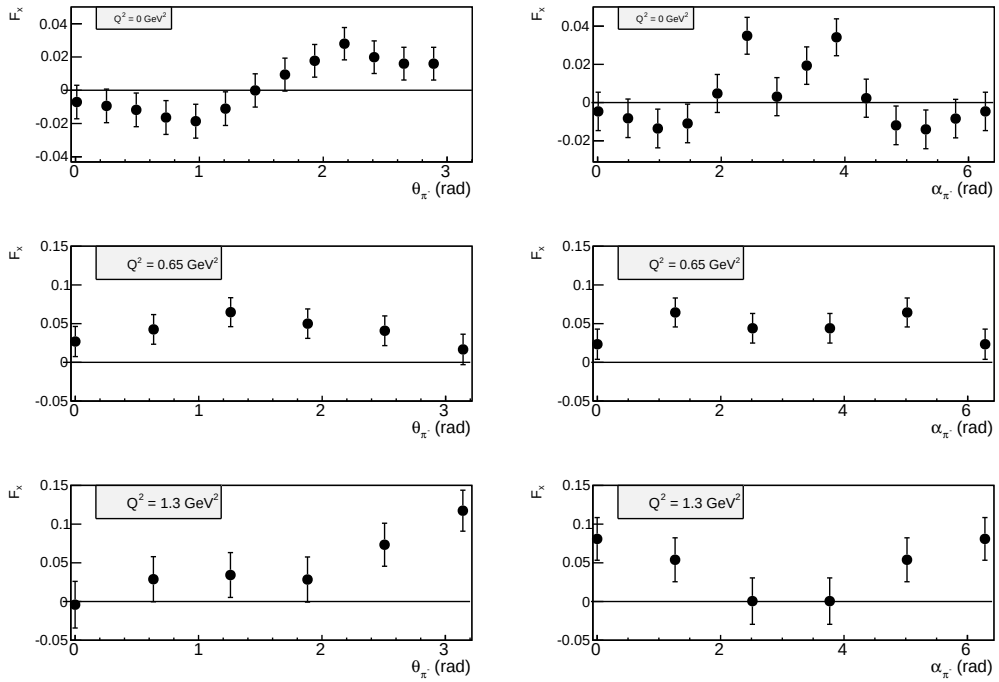

Figure 37: The Q^2 evolution of the ratio F_x for the relative differences between the $d\sigma/d(-\cos\theta_{\pi^-})$ and $d\sigma/d\alpha_{[p'\pi^+][p\pi^-]}$ one-fold differential cross sections computed with and without a hybrid baryon contribution.

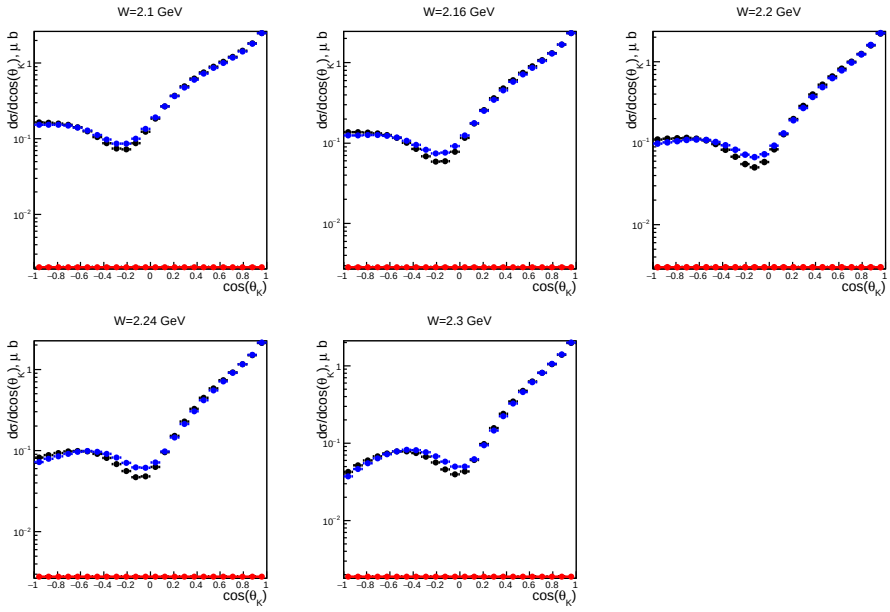

Figure 38: Comparison of the model cross section $d\sigma/d\cos(\theta_K)$ (black points) with the model plus resonance cross section (blue points) for the beam energy 8.8 GeV and the torus current -2950 A at Q^2=0.3 GeV^2 and at few values of W. The cross section of the resonance contribution is shown in red. The spin of the resonance is 1/2 and the A_{12} is 12×10^{-3}GeV$^{-1/2}$, it corresponds to the minimal A_{12} from Table 7. Statistical uncertainties are negligible.

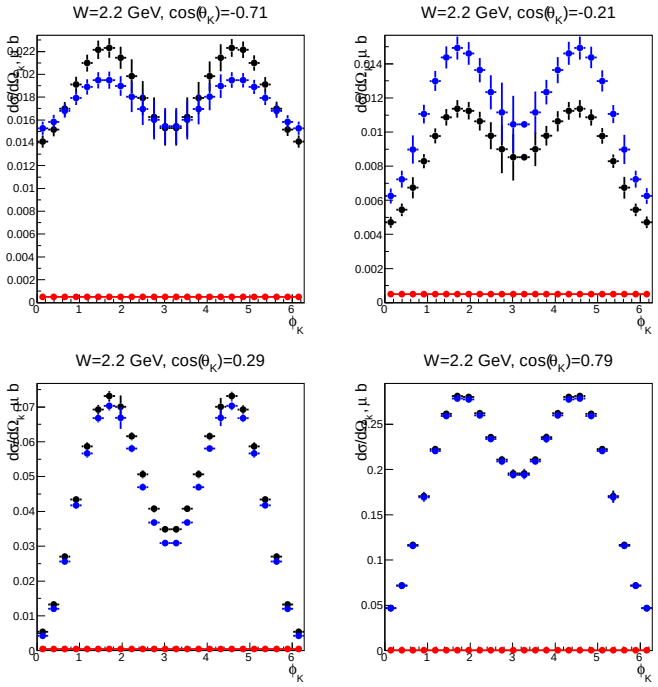

Figure 39: Comparison of the model cross section $d\sigma/d\Omega$ with the model plus resonance cross section at $W = M_R$ and few values of $\cos\theta_K$. The same conditions run condition and Q^2 as in Fig. 38. The error bars are statistical only.

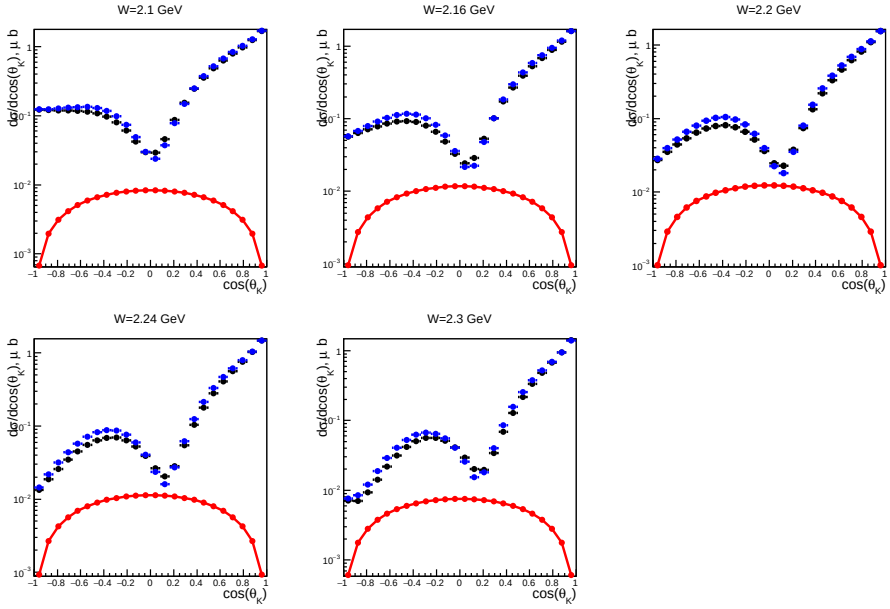

Figure 40: Comparison of the model cross section $d\sigma/d\cos(\theta_K)$ (black points) with the model plus resonance cross section (blue points) for the beam energy 8.8 GeV and the torus current -2950 A at Q^2=0.3 GeV^2 and at few values of W. The cross section of the resonance contribution is shown in red. The spin of the resonance is 3/2 and the $A_{3/2}$ is 18×10^{-3}GeV$^{-1/2}$, it corresponds to the minimal A_{32} from Table 7. Statistical uncertainties are negligible.

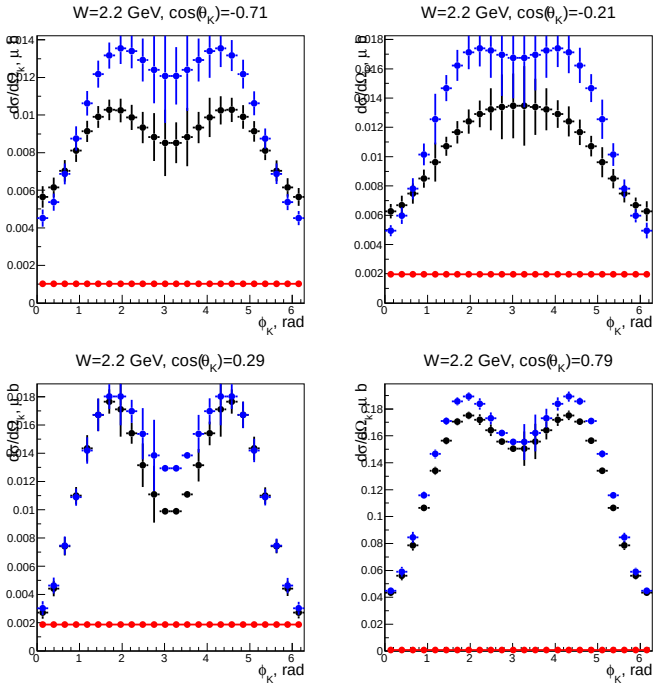

Figure 41: Comparison of the model cross section $d\sigma/d\Omega$ with the model plus resonance cross section at $W = M_R$ and few values of $\cos\theta_K$. The same conditions run condition and Q^2 as in Fig. 40. The error bars are statistical only.

The Legendre moments may be used to expand the structure functions in terms of the orthogonal Legendre polynomials:

$$\sigma(x)_i = \sum_m P_m(Q^2, W) L_M(\cos\theta^* k) \tag{19}$$

where the first seven Legendre polynomial functions have the following form:

$$\begin{aligned}
L_0 &= 1 \\
L_1 &= \cos\theta \\
L_2 &= \frac{1}{2}(3\cos\theta^2 - 1) \\
L_3 &= \frac{1}{2}(5\cos\theta^3 - 3\cos\theta) \\
L_4 &= \frac{1}{8}(35\cos\theta^4 - 30\cos\theta^2 + 3) \\
L_5 &= \frac{1}{8}(63\cos\theta^5 - 70\cos\theta^3 + 15\cos\theta) \\
L_6 &= \frac{1}{16}(231\cos\theta^6 - 315\cos\theta^4 + 105\cos\theta - 5).
\end{aligned} \tag{20}$$

The expansion of the structure function in terms of Legendre moments is believed to be an alternative way to prove the sensitivity to the hybrid baryon contribution, since the appearance of a structure in a single Legendre moment at the same value of W for each Q^2 point is likely a signal from a resonance contribution.

Figure 42 reports the first four Legendre polynomial fits, measured by CLAS for the $K^+\Lambda$ electroproduction structure functions at $Q^2 = 1.8$ GeV^2 [64]. They show the presence of a structure at $W = 1.7$ GeV for the C_0 in both the $d\sigma_U$ and $d\sigma_{LT}$ and a structure at $W = 1.9$ GeV in both C_2 and C_3 in $d\sigma_U$.

Of course only a full amplitude partial wave analysis will constitute a definite proof for the presence of a resonance, but the study of Legendre moments may provide the first hint of their appearance. A study of the first seven Legendre moments of the $d\sigma_U$, $d\sigma_{TT}$, and $d\sigma_{LT}$ structure functions has been performed for the models A and B of the $K\Lambda$ electroproduction, described in the previous section. The results are reported in Section 7.

7.9 Experimental Sensitivity to Hybrid Resonance States

The ability of the JM model to distinguish hybrid state signal is also illustrated in Fig. 43, where the χ^2 value is plotted as a function of the resonance mass for Q^2 points. The dip in χ^2 dependences is clearly seen on the W_h value corresponding to the expected mass of the hybrid state.

8 Beamtime Estimate

The complete hybrid baryon program will require two beam energies, 6.6 GeV and 8.8 GeV, to cover with high statistics the lowest Q^2 range where the scattered electron is detected

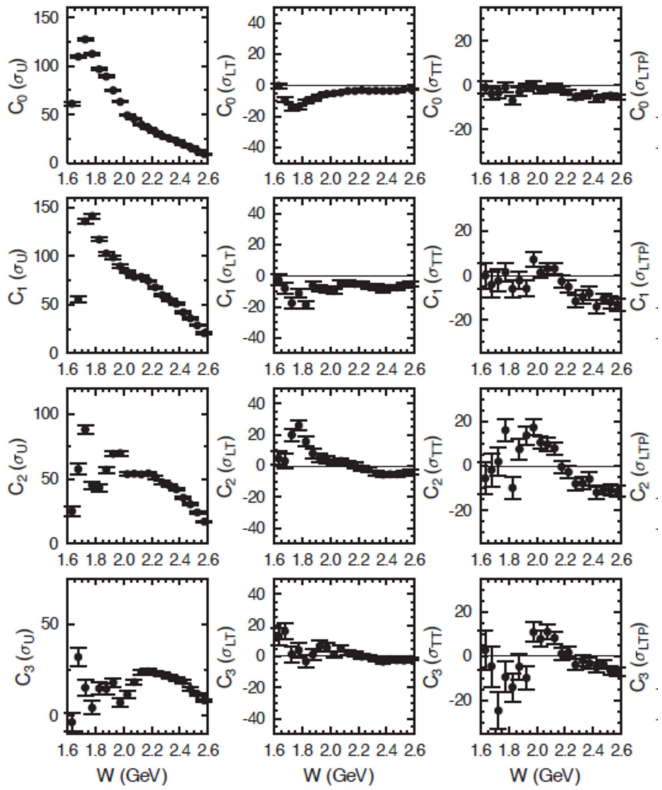

Figure 42: Legendre polynomial fit coefficients for $m = 0 \rightarrow 3$ as a function of W for the $d\sigma_U$ (left), $d\sigma_{LT}$ (middle), and $d\sigma_{TT}$ (right) structure functions for the $K\Lambda$ electroproduction at $Q^2 = 1.8$ GeV^2 [64].

in the angle range from $2.5° \leq \theta_e \leq 4.5°$. We request new beam time of 60 days that are divided into 30 days at 6.6 GeV and 30 days at 8.8 GeV.

9 Summary

In this proposal we laid out an extensive program to study the excitation of nucleon resonances in meson electroproduction using electron beam energies of 6.6 GeV and 8.8 GeV. The main focus is on the search for gluonic light-quark baryons in the mass range up to 3 GeV and in the Q^2 range from 0.05 GeV^2 to 2.0 GeV^2. We have estimated the rates for two of the channels we propose to study, $K^+\Lambda$ ($K^+\Sigma^0$) and $p\pi^+\pi^-$, but all other channels detected in CLAS12 will be subjected to analyses as well. The expected rates are very high, thanks to the very forward scattered electrons with a minimum Q^2 of 0.05 GeV^2 that are detected in the Forward Tagger. The data will be subjected to state-of-the-art partial wave analyses that were developed during the past years for baryon resonance analyses. Beyond the main focus of this proposal on hybrid baryons, a wealth of data will be collected in many different channels that will put meson electroproduction data on par with real photoproduction in terms of production rates and will allow for a vast extension of the ongoing N^* electroexcitation program with CLAS at lower energies. It will complement the already approved program to study nucleon resonance excitations at the highest Q^2 achievable at 11 GeV beam energy, by the experiment E12-11-005.

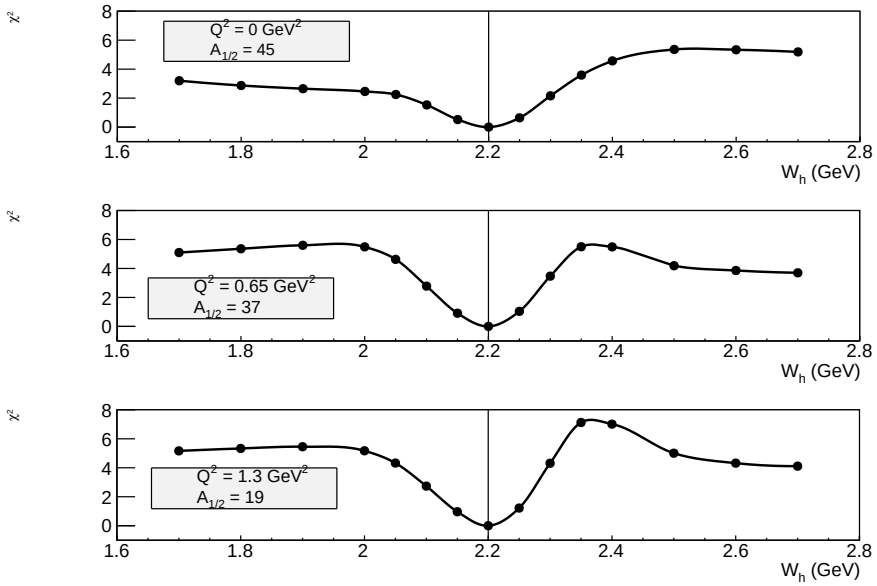

Figure 43: χ^2 versus W_h distributions for three Q^2 values obtained from JM model.

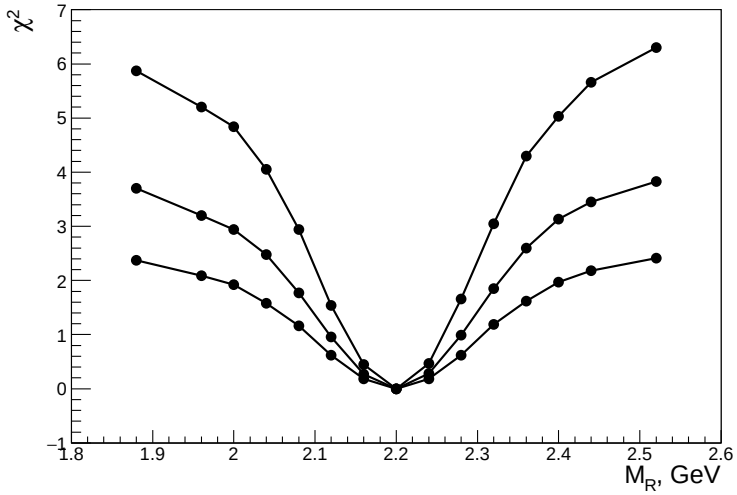

Figure 44: The χ^2 between two model cross sections. One cross section was calculated with the hybrid mass equal to 2.2 GeV. The other cross section was calculated with the variable hybrid mass (M_R). The χ^2 square was calculated as described in Section 7.7 using the estimated statistical uncertainties. Three lines from bottom to top correspond to the three values of $A_{1/2}$: 15, 19 and 25 in the units of 10^{-3} GeV$^{-1/2}$. The value 19 is the minimal $A_{1/2}$ from Table 7 for the spin 1/2 resonance at Q^2=0.5 GeV^2.

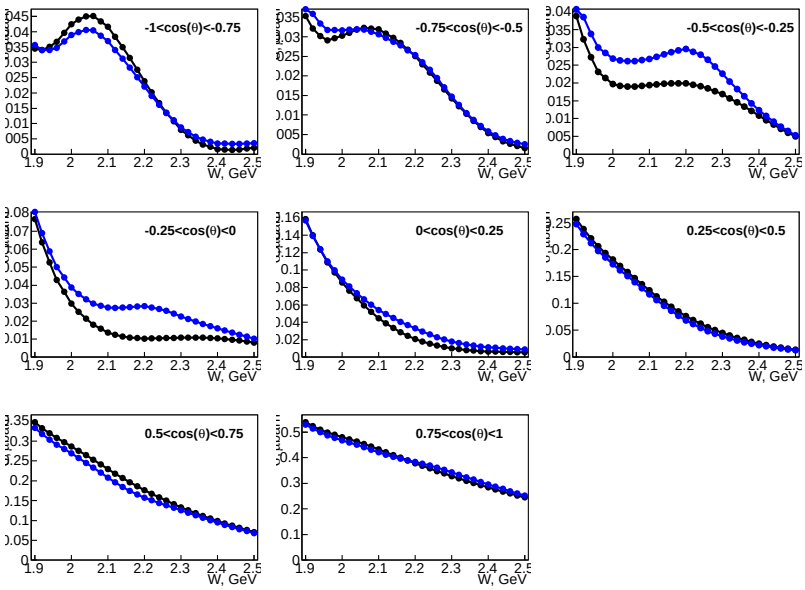

Figure 45: The integrated model cross section (in black) and model plus resonance ($A_{1/2}$=40×10^{-3} GeV$^{-1/2}$) cross section (in blue) at different $\cos\theta_K$ bins and at Q^2=0.5 GeV^2. The pronounced structures at small $\cos(\theta_K)$ can be indications of a resonance.

A Appendix A - KY Electroproduction

In the electroproduction of KY on the proton a beam of incoming electrons of energy E_e impinges on a fixed proton target of mass M_p, the scattered electrons emerging with energy $E_{e'}$ are detected at the the direction identified by the angles $(\theta_{e'}, \phi_{e'})$ and the kaons produced with momentum $\tilde{p_k} = (E_k, \vec{p_k})$ are measured. The cross section is five-fold differential in the scattered electron energy and direction $dE_{e'}d\Omega_{e'}$ and kaon direction $d\Omega_K$. In the one photon exchange approximation, a virtual photon of momentum $\tilde{q} = \tilde{p_e} - \tilde{p_{e'}} = (\nu, \vec{q})$, is emitted by the scattered electron and absorbed by the proton. The cross section can be expressed by the product of an equivalent flux of virtual photons Γ and the virtual photoproduction of the KY final state as:

$$\frac{d^5\sigma}{dE_{e'}d\Omega_{e'}d\Omega_K} = \Gamma\frac{d^2\sigma}{d\Omega^*_K} \tag{21}$$

where the virtual photoabsorbtion cross section is expressed in the γ^*p or KY CM reference frame and the photon flux Γ is given by the relation:

$$\Gamma = \frac{\alpha}{2\pi^2}\frac{E_{e'}}{E_e}\frac{W^2 - m_p^2}{Q^2}\frac{1}{1-\epsilon} \tag{22}$$

and depends on the electron scattering process only, in terms of the variables $Q^2 = -\tilde{q^2}$, the photon virtuality, $W = \sqrt{M_p^2 + 2M_p\nu - Q^2}$, the total energy in the γ^*p CM reference frame, and the virtual photon polarization ϵ:

$$\epsilon = \frac{4E_eE_{e'} - Q^2}{2(E_e^2 + E_{e'}^2) + Q^2}. \tag{23}$$

The kinematics of the process is shown in Fig. 46.

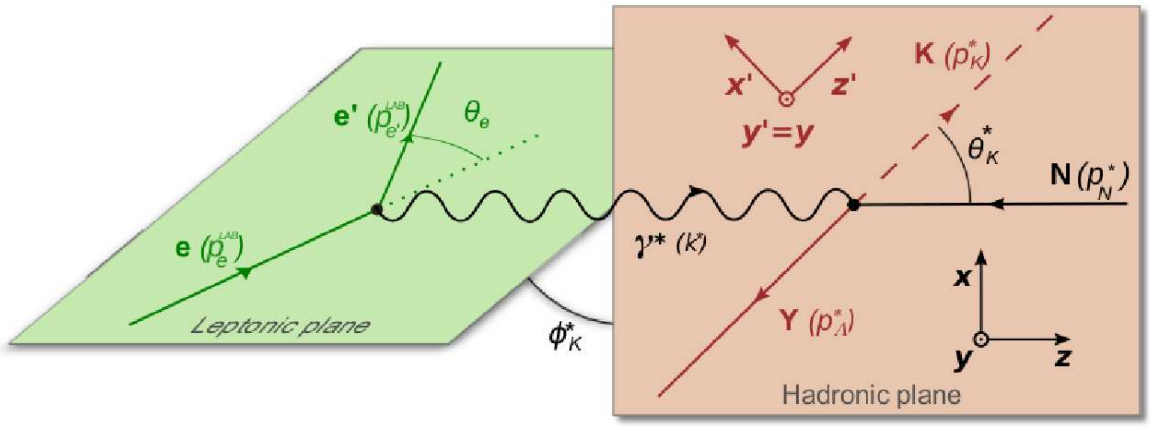

Figure 46: Kinematics of KY electroproduction. The quantities in the leptonic plane are expressed in the laboratory frame. The quantities in the hadronic plane are expressed in the CM frame of the γ^*p or KY system.

After integrating over the azimuthal angle of the scattered electron, the photoabsorbtion cross section can be expressed in terms of the variables Q^2, W, and the kaon scattering angle in the KY CM frame θ_K^* and the angle between the leptonic and hadronic plane ϕ_K^*. Introducing the appropriate Jacobian, the form of the cross section may be rewritten as:

$$\frac{d^4\sigma}{2\pi dW dQ^2 d\Omega_K^*} = \Gamma_v \frac{d^2\sigma_v}{d\Omega_K^*} \tag{24}$$

where

$$\Gamma_v = \frac{\alpha}{4\pi}\frac{W}{E^2}\frac{W^2 - m_P^2}{Q^2(1-\epsilon)}\frac{1}{m_P^2} \tag{25}$$

is the corresponding flux of virtual photons.

For the case of an unpolarized electron beam, with no target or recoil polarizations, the virtual photon absorbtion cross section can be written as:

$$\frac{d^2\sigma}{d\Omega_K^*} = \frac{d^2\sigma_T}{d\Omega_K^*} + \epsilon\frac{d^2\sigma_L}{d\Omega_K^*} + \epsilon\frac{d^2\sigma_{TT}}{d\Omega_K^*}\cos 2\phi_K^* + \sqrt{\epsilon(1+\epsilon)}\frac{d^2\sigma_{LT}}{d^2\Omega_K^*}cos\phi_K^*. \tag{26}$$

where the $\frac{d^2\sigma_i}{d\Omega_K^*}$ are the structure functions that measure the response of the hadronic system. $i = T,\ L,\ TT$, and LT represent the transverse, longitudinal, and interference structure functions and depend on the variables W, Q^2 and θ_K^* only.

In the formalism used in the Ghent model [12], the cross section may be related to the reaction amplitude as:

$$M_{\lambda_\gamma}^{\lambda_p\lambda_f} = \langle \lambda_f \left| T_r \right| \lambda_\gamma \lambda_p \rangle \tag{27}$$

in term of the nine helicity dependent bilinear functions:

$$H_{\lambda\lambda'} = \sum_{\lambda_N\lambda_Y} M_\lambda^{'\lambda_N\lambda_Y}(M_\lambda^{'\lambda_N\lambda_Y})^\dagger \tag{28}$$

where λ and λ' assume all possible values of the virtual photon helicity, $0, \pm 1$.

The transverse, longitudinal, and interference structure functions are defined as:

$$\begin{aligned}
\frac{d^2\sigma_L}{d\Omega_K^*} &= 2\chi\frac{1}{(4\pi)^2}H_{0,0} \\
\frac{d^2\sigma_T}{d\Omega_K^*} &= \chi\frac{1}{(4\pi)^2}(H_{1,1} + H_{-1,-1}) \\
\frac{d^2\sigma_{TT}}{d\Omega_K^*} &= -\chi\frac{1}{(4\pi)^2}(H_{1,-1} + H_{-1,1}) \\
\frac{d^2\sigma_{LT}}{d\Omega_K^*} &= -\chi\frac{1}{(4\pi)^2}(H_{0,1} + H_{1,0} - H_{-1,0} - H_{0,-1})
\end{aligned} \tag{29}$$

where the normalization factor χ assumes the form:

$$\chi = \frac{1}{16Wm_P}\frac{\sqrt{W^4 + (m_K^2 - m_\Lambda^2)^2 - 2W^2(m_K^2 + m_\Lambda^2)}}{2W}\frac{2m_P}{W^2 - m_P^2}. \tag{30}$$

The hybrid resonance amplitudes $M_{\lambda}^{\lambda_N\lambda_Y}$ described in Appendix B and reported in Tables 8 and 9 for spin $\frac{1}{2}$ and $\frac{3}{2}$ resonaces, respectively, have been added to the $M_{\lambda}^{\lambda_N\lambda_Y}$ reaction amplitudes from Ref. [12] (KY model A) to form a set of total amplitudes:

$$M_{\lambda}^{\lambda_N\lambda_Y} = M_{\lambda}^{\lambda_N\lambda_Y} + M_{\lambda}^{\lambda_N\lambda_Y}. \tag{31}$$

The resulting calculated cross sections from Eq.(29) have been used as the KY Model B to study the sensitivity of the proposed experiment to the hybrid baryons electrocouplings.

B Appendix B - Hybrid Baryon Excitation Amplitudes

The excitation of a single hybrid resonance in the helicity representation $\langle \lambda_f \left| T_r \right| \lambda_\gamma \lambda_p \rangle$ may be expressed using a relativistic Breit-Wigner (BW) ansatz:

$$M_{\lambda_\gamma}^{\lambda_p\lambda_f} = \langle \lambda_f \left| T_r \right| \lambda_\gamma \lambda_p \rangle = \frac{\langle \lambda_f \left| T_{dec} \right| \lambda_R \rangle \langle \lambda_R \left| T_{em} \right| \lambda_\gamma \lambda_p \rangle}{M_r^2 - W^2 - i\Gamma_r M_r}, \tag{32}$$

where M_r and Γ_r are the resonance mass and total width, respectively; we have assumed both the total and partial decay widths are energy independent.

The matrix elements $\langle \lambda_R \left| T_{em} \right| \lambda_\gamma \lambda_p \rangle$ and $\langle \lambda_f \left| T_{dec} \right| \lambda_R \rangle$ are the electromagnetic production and hadronic decay amplitudes, respectively, of the N^* with helicity $\lambda_R = \lambda_\gamma - \lambda_p$, in which λ_γ and λ_p are the helicities of the photon and proton in the initial state, respectively, and λ_f is the helicity of final-state hadron in the N^* decay.

In the case of the KY final state, the hadronic decay amplitudes $\langle \lambda_f | T_{dec} | \lambda_R \rangle$ are related to the Γ_{λ_f} partial hadronic decay widths of the N^* to the KY final states f of helicity $\lambda_f = \lambda_Y$ by:

$$\langle \lambda_f | T_{dec} | \lambda_R \rangle = \langle \lambda_f | T_{dec}^{J_r} | \lambda_R \rangle d_{\mu\nu}^{J_r}(\cos\theta_K) e^{i\mu\phi_K}, \tag{33}$$

with $\mu = \lambda_R$ and $\nu = -\lambda_Y$, and

$$\langle \lambda_f | T_{dec}^{J_r} | \lambda_R \rangle = \frac{2\sqrt{2\pi}\sqrt{2J_r+1} M_r \sqrt{\Gamma_{\lambda_f}}}{\sqrt{p_i^r}} \sqrt{\frac{p^r}{p}}. \tag{34}$$

Here p^r and p are the magnitudes of the three-momenta of the final state K for the $N^* \to KY$ decay evaluated at $W = M_r$ and at the running W, respectively. The variables θ_K, ϕ_K are the CM frame polar and azimuthal angles for the final kaon, and J_r is the N^* spin.

The final state Λ or Σ^0 baryons can only be in the helicity states $\lambda_f = \pm\frac{1}{2}$. The hadronic decay amplitudes $\langle \lambda_f | T_{dec}^{J_r} | \lambda_R \rangle$ with $\lambda_f = \pm\frac{1}{2}$ are related by P-invariance, which requires that the absolute values for both amplitudes are the same. Therefore, the hybrid state partial decay widths to the $K^+\Lambda$ and $K^+\Sigma^0$ final states Γ_{λ_f} can be estimated as:

$$\Gamma_{\lambda_f} = \frac{1}{2}\Gamma_r 0.03, \tag{35}$$

where the factor of 0.03 reflects the adopted 3% branching ratio for hybrid baryon decays to the KY final state.

The following relationships between the transition amplitudes $\langle \lambda_R \left| T_{em} \right| \lambda_\gamma \lambda_p \rangle$ and the $\gamma_v N N^*$ electrocouplings from Ref. [13] have been used:

$$\langle \lambda_R |\, T_{em}\, | \lambda_\gamma \lambda_p \rangle = \frac{W}{M_r} \sqrt{\frac{8 M_N M_r q_{\gamma_r}}{4\pi\alpha}} \sqrt{\frac{q_{\gamma_r}}{q_\gamma}} A_{1/2,3/2}(Q^2), \tag{36}$$

with

$$|\lambda_\gamma - \lambda_p| = \frac{1}{2}, \frac{3}{2} \tag{37}$$

for transverse photons and

$$\langle \lambda_R |\, T_{em}\, | \lambda_\gamma \lambda_p \rangle = \frac{W}{M_r} \sqrt{\frac{16 M_N M_r q_{\gamma_r}}{4\pi\alpha}} \sqrt{\frac{q_{\gamma_r}}{q_\gamma}} S_{1/2}(Q^2), \tag{38}$$

for longitudinal photons. Here q_γ is the absolute value of the initial photon three-momentum of virtuality $Q^2 > 0$ with $q_\gamma = \sqrt{Q^2 + E_\gamma^2}$ and E_γ the photon energy in the CM frame at the running W, with

$$E_\gamma = \frac{W^2 - Q^2 - M_N^2}{2W}. \tag{39}$$

The $q_{\gamma,r}$ value is then computed from Eq.(39) with $W = M_r$.

We have investigated the effect of adding contributions to the KY and $\pi^+\pi^- p$ reaction amplitudes from hybrid baryon states with spin-parities $J^P = \frac{1}{2}^+$ and $\frac{3}{2}^+$. Electroexcitation of the former state can be described by two electrocouplings $A_{1/2}$ and $S_{1/2}$, while the latter should be described by three electrocouplings, $A_{1/2}$, $S_{1/2}$, and $A_{3/2}$. Information on the expected Q^2 evolution of the aforementioned electrocouplings for hybrid states is, to the best of our knowledge, currently not available. Therefore we have varied the hybrid baryon electrocouplings to determine their minimal absolute values above which the signal from the hybrid baryon can be observed, in the difference between the angular distributions with and without the hybrid baryon contributions. These studies have independently been done at fixed values of Q^2, for different bins in the range proposed by this proposal. It may be noted that, in the very high Q^2 regime, the following relations for the hybrid baryon electrocouplings have been used in literature [23] to model the hybrid baryon signatures:

$$A_{1/2} = A, \quad S_{1/2} = AQ, \quad A_{3/2} = A/Q^2, \tag{40}$$

where $Q = \sqrt{Q^2}$ and A is a common term. However, in the low Q^2 regime, these relations are not valid and we have considered fixed independent values for all three electrocouplings.

Substituting Eq.(33) and Eq.(38) in Eq.(32), one obtains:

$$M_{\lambda_\gamma}^{\lambda_p \lambda_f} = \langle \lambda_f |\, T_r\, | \lambda_\gamma \lambda_p \rangle = \frac{\langle \lambda_f |\, T_{dec}\, | \lambda_\gamma \lambda_R \rangle \langle \lambda_R |\, T_{em}\, | \lambda_\gamma \lambda_p \rangle}{M_r^2 - W^2 - i\Gamma_r M_r} \tag{41}$$

$$= \frac{\langle \lambda_f |\, T_{dec}^{J_r}\, | \lambda_R \rangle}{M_r^2 - W^2 - i\Gamma_r M_r} d^{J_r}_{\mu\nu}(\cos\theta_K^*) e^{i\mu\phi_K^*} \frac{W}{M_r} \sqrt{\frac{c M_N M_r q_{\gamma_r}}{4\pi\alpha}} \sqrt{\frac{q_{\gamma_r}}{q_\gamma}}, \tag{42}$$

with $A_{1/2,3/2}(Q^2)$, $c = 8$ and $S_{1/2}(Q^2)$, $c = 16$. Substituting also Eq.(34), the following expression is obtained:

$$M_{\lambda_\gamma}^{\lambda_p\lambda_f} = \frac{2\sqrt{2\pi}\sqrt{2J_r+1}M_r\sqrt{\Gamma_{\lambda_f}}}{M_r^2 - W^2 - i\Gamma_r M_r} d_{\mu\nu}^{J_r}(cos\theta_K^*)e^{i\mu\phi_K^*}\frac{W}{M_r\sqrt{p_i}}\sqrt{\frac{cM_N M_r q_{\gamma_r}}{4\pi\alpha}}\sqrt{\frac{q_{\gamma_r}}{q_\gamma}}, \tag{43}$$

with $A_{1/2,3/2}(Q^2),\ c = 8$ and $S_{1/2}(Q^2),\ c = 16$.

At this point it is possible to express $M_{\lambda_\gamma}^{\lambda_p\lambda_Y}$ in terms of a factor that doesn't depend on the λ_p, λ_Y, and λ_γ helicities:

$$F_{J_r} = \frac{2\sqrt{2\pi}\sqrt{2J_r+1}M_r\sqrt{\Gamma_{\lambda_f}}}{M_r^2 - W^2 - i\Gamma_r M_r}\frac{W}{M_r\sqrt{p_i}}\sqrt{\frac{cM_N M_r q_{\gamma_r}}{4\pi\alpha}}\sqrt{\frac{q_{\gamma_r}}{q_\gamma}}, \tag{44}$$

with $A_{1/2}(Q^2) = A,\ c = 8$ and $S_{1/2}(Q^2) = AQ,\ c = 16$, which is multiplied by the terms that introduce the angular dependence upon the K angles in the CM frame:

$$M_{\lambda_\gamma}^{\lambda_p\lambda_f} = \langle\lambda_f|\, T_r\, |\lambda_\gamma\lambda_p\rangle = F_{J_r} d_{\mu\nu}^{J_r}(cos\theta_K^*)e^{i\mu\phi_K^*}, \tag{45}$$

with $\mu = \lambda_R$ and $\nu = -\lambda_Y$. In the formalism used by the Ghent RPR-2011 model [12], the expressions F_{J_r} must be multiplied by a factor $\sqrt{4\pi\alpha}$.

The $d_{\mu\nu}^{J_r}(\cos\theta_K^*)$ coefficients are the Wigner rotation matrix elements, for which the relationship $d_{m',m}^J = (-1)^{m-m'}d_{m,m'}^J = d_{-m,-m'}^J$ is valid. For $J = \frac{1}{2}$ they present the following explicit form:

$$\begin{aligned}
d_{1/2\ 1/2}^{1/2}(\cos\theta_K^*) &= \cos\theta_K^*/2 \\
d_{1/2\ -1/2}^{1/2}(\cos\theta_K^*) &= -\sin\theta_K^*/2 \\
d_{-1/2\ -1/2}^{1/2}(\cos\theta_K^*) &= d_{1/2\ 1/2}^{1/2}(\cos\theta_K^*) = \cos\theta_K^*/2 \\
-d_{-1/2\ 1/2}^{1/2}(\cos\theta_K^*) &= d_{1/2\ -1/2}^{1/2}(\cos\theta_K^*) = -\sin\theta_K^*/2,
\end{aligned} \tag{46}$$

while for $J = \frac{3}{2}$ one has:

$$\begin{aligned}
d_{3/2\ 3/2}^{3/2}(\cos\theta_K^*) &= \frac{1+\cos\theta_K^*}{2}\cos\theta_K^*/2 = d_{-3/2\ -3/2}^{3/2}(\cos\theta_K^*) \\
d_{3/2\ 1/2}^{3/2}(\cos\theta_K^*) &= -\sqrt{3}\frac{1+\cos\theta_K^*}{2}\sin\theta_K^*/2 = -d_{-3/2\ -1/2}^{3/2}(\cos\theta_K^*) \\
d_{3/2\ -1/2}^{3/2}(\cos\theta_K^*) &= \sqrt{3}\frac{1-\cos\theta_K^*}{2}\cos\theta_K^*/2 = (-1)^{-3/2-1/2}d_{-3/2\ 1/2}^{3/2}(\cos\theta_K^*) \\
&= d_{-3/2\ 1/2}^{3/2}(\cos\theta_K^*) \\
d_{3/2\ -3/2}^{3/2}(\cos\theta_K^*) &= -\frac{1-\cos\theta_K^*}{2}\sin\theta_K^*/2 \\
d_{1/2\ 1/2}^{3/2}(\cos\theta_K^*) &= \frac{3\cos\theta_K^*-1}{2}\cos\theta_K^*/2 = d_{-1/2\ -1/2}^{3/2}(\cos\theta_K^*) \\
d_{1/2\ -1/2}^{3/2}(\cos\theta_K^*) &= -\frac{3\cos\theta_K^*+1}{2}\sin\theta_K^*/2 = -d_{-1/2\ 1/2}^{3/2}(\cos\theta_K^*)
\end{aligned} \tag{47}$$

The final expressions for the hybrid baryon excitation amplitudes $M_{\lambda_\gamma}^{\lambda_p \lambda_f}$, are given in Table 8 and Table 9, for $J = \frac{1}{2}$ and $J = \frac{3}{2}$, respectively. No explicit dependence on the ϕ_K angle is introduced.

λ_γ	$\lambda_p = 1/2$ $\lambda_Y = 1/2$	$\lambda_p = 1/2$ $\lambda_Y = -1/2$	$\lambda_p = -1/2$ $\lambda_Y = 1/2$	$\lambda_p = -1/2$ $\lambda_Y = -1/2$
1	$F_{1/2}A_{1/2}(-\sin\theta_K^*/2)$	$F_{1/2}A_{1/2}(\cos\theta_K^*/2)$	0	0
0	$F_{1/2}S_{1/2}(\cos\theta_K^*/2)$	$F_{1/2}S_{1/2}(\sin\theta_K^*/2)$	$F_{1/2}S_{1/2}(-\sin\theta_K^*/2)$	$F_{1/2}S_{1/2}(\cos\theta_K^*/2)$
-1	0	0	$F_{1/2}A_{1/2}(\cos\theta_K^*/2)$	$F_{1/2}A_{1/2}(\sin\theta_K^*/2)$

Table 8: Expressions for $M_{\lambda_\gamma}^{\lambda_p \lambda_Y}$ for $J^P = \frac{1}{2}^+$ for all possible values of λ_P, λ_Y, and λ_γ. The Wigner rotation matrix elements have been inserted.

λ_γ	$\lambda_p = 1/2$ $\lambda_Y = 1/2$	$\lambda_p = 1/2$ $\lambda_Y = -1/2$	$\lambda_p = -1/2$ $\lambda_Y = 1/2$	$\lambda_p = -1/2$ $\lambda_Y = -1/2$
1	$F_{3/2}A_{1/2}d^{3/2}_{1/2\ -1/2}$	$F_{3/2}A_{1/2}d^{3/2}_{1/2\ 1/2}$	$F_{3/2}A_{3/2}d^{3/2}_{3/2\ -1/2}$	$F_{3/2}A_{3/2}d^{3/2}_{3/2\ 1/2}$
0	$F_{3/2}S_{1/2}d^{3/2}_{-1/2\ -1/2}$	$F_{3/2}S_{1/2}d^{3/2}_{-1/2\ 1/2}$	$F_{3/2}S_{1/2}d^{3/2}_{1/2\ -1/2}$	$F_{3/2}S_{1/2}d^{3/2}_{1/2\ 1/2}$
-1	$F_{3/2}A_{3/2}d^{3/2}_{-3/2\ -1/2}$	$F_{3/2}A_{3/2}d^{3/2}_{-3/2\ 1/2}$	$F_{3/2}A_{1/2}d^{3/2}_{-1/2\ -1/2}$	$F_{3/2}A_{1/2}d^{3/2}_{-1/2\ 1/2}$

Table 9: Values of $M_{\lambda_\gamma}^{\lambda_p \lambda_Y}$ for $J^P = \frac{3}{2}^+$ for all the possible values of λ_P, λ_Y, and λ_γ. Note that now the terms with $\mu = 3/2$ are non-zero.

References

[1] K.A. Olive *et al.* [Particle Data Group Collaboration], Chin. Phys. C **38**, 090001 (2014)

[2] I.G. Aznauryan *et al.* [CLAS Collaboration], Phys. Rev. C **78**, 045209 (2008).

[3] T. Barnes and F.E. Close, Phys. Lett. B **123**, 89 (1983); E. Golowich, E. Haqq, and G. Karl, Phys. Rev. D **28**, 160 (1983);C.E. Carlson and T.H. Hansson, Phys. Lett. B **128**, 95 (1983); I. Duck and E. Umland, Phys.Lett. B **128** (1983) 221.

[4] I.G. Aznauryan and V.D. Burkert, Prog. Part. Nucl. Phys. **67**, 1 (2012).

[5] I.G. Aznauryan *et al.* [CLAS Collaboration], Phys. Rev. C **80**, 055203 (2009).

[6] J.J. Dudek and R.G. Edwards, Phys. Rev. D **85**, 054016 (2012).

[7] I.G. Aznauryan *et al.*, Int. J. Mod. Phys. E **22**, 1330015 (2013).

[8] V.I. Mokeev and I.G. Aznauryan, Int. J. Mod. Phys. Conf. Ser. **26**, 1460080 (2014).

[9] V.I. Mokeev. Presentation at the ECT* Workshop, *Nucleon Resonances: From Photoproduction to High Photon Virtualities*, (2015).

[10] V.I. Mokeev *et al.*, Phys. Rev. C **93**, 025206 (2016).

[11] V.I. Mokeev *et al.*, Phys. Rev. C **80**, 045212 (2009).

[12] L. De Cruz, J. Ryckebusch, T. Vrancx and P. Vancraeyveld, Phys. Rev. C **86**, 015212 (2012).

[13] V.I. Mokeev *et al.* [CLAS Collaboration], Phys. Rev. C **86**, 035203 (2012)

[14] A. Anisovich *et al.*, Eur. Phys. J. A **48**, 15 (2012).

[15] D. Ronchen *et al.*, Eur. Phys. J. A **50**, 101 (2014).

[16] A.P. Szczepaniak and M.R. Pennington, Phys. Lett. B **737**, 283 (2014).

[17] See http://pdg.lbl.gov/2015/reviews/rpp2015-rev-n-delta-resonances.pdf

[18] JLab Experiment E12-09-003, spokespersons: V.D. Burkert, P. Cole, R. Gothe, K. Joo, V. Mokeev, P. Stoler

[19] JLab Experiment E12-06-108A, spokespersons: D.S. Carman, R. Gothe, V. Mokeev

[20] S. Capstick and P.R. Page, Phys. Rev. C **66**, 065204 (2002); Phys. Rev. D **60**, 111501 (1999).

[21] P.R. Page, Int. J. Mod. Phys. A **20**, 1791 (2005).

[22] C.K. Chow, D. Pirjol and T.M. Yan, Phys. Rev. D **59**, 056002 (1999).

[23] C.E. Carlson and N.C. Mukhopadhyay, Phys. Rev. Lett. **67**, 3745 (1991).

[24] T.T. Takahashi and H. Suganuma, Phys. Rev. Lett. **90**, 182001 (2003).

[25] E. Kou, Phys. Rev. D **63**, 054027 (2001).

[26] I.V. Anikin, V. M. Braun, and N. Offen, Phys. Rev. D **92**, 074044 (2015).

[27] J. Segovia , B. El-Bennich, E. Rojas, *et al.*, Phys. Rev. Lett. **115**, 015203 (2015).

[28] V.I. Mokeev *et al.*, Phys. Rev. C **93**, 054016 (2016).

[29] Z.P. Li, Phys. Rev. D **44**, 2841 (1991).

[30] Z.P. Li, V. Burkert and Z.J. Li, Phys. Rev. D **46**, 70 (1992).

[31] S.J. Brodsky and G.R. Farrar, Phys. Rev. Lett. **31**, 1153 (1973); Phys. Rev. D **11**, 1309 (1975); V.A. Matveev, R.M. Muradyan, and A.V. Tavkhelidze, Lett. Nuovo Cimento **7**, 719 (1978).

[32] M. Dugger *et al.*, [CLAS Collaboration], Phys. Rev. C **79**, 065206 (2009).

[33] V.I. Mokeev *et al.*, Eur. Phys. J. Web Conf. **113**, 01013 (2016).

[34] M. Ripani *et al.*, Nucl. Phys. A **672**, 220 (2000).

[35] A.V. Anisovich *et al.*, Eur. Phys. J. A **48**, 15 (2012).

[36] A.V. Anisovich *et al.*, Eur. Phys. J. A **48**, 88 (2012).

[37] A.V. Anisovich *et al.*, Eur. Phys. J. A **49**, 158 (2013).

[38] J.W.C. McNabb *et al.* [CLAS Collaboration], Phys. Rev. C **69**, 042201 (2004).

[39] R. Bradford *et al.* [CLAS Collaboration], Phys. Rev. C **73**, 035202 (2006).

[40] R. Bradford *et al.* [CLAS Collaboration], Phys. Rev. C **75**, 035205 (2007).

[41] M.E. McCracken *et al.* [CLAS Collaboration], Phys. Rev. C **81**, 025201 (2010).

[42] K.H. Glander *et al.* [SAPHIR Collaboration], Eur. Phys. J. A **19**, 251 (2004).

[43] T.C. Jude *et al.* [Crystal Ball Collaboration], Phys. Lett. B **735**, 035205 (2014).

[44] A. Lleres *et al.* [GRAAL Collaboration], Eur. Phys. J. A **31**, 79 (2007).

[45] A. Lleres *et al.* [GRAAL Collaboration], Eur. Phys. J. A **39**, 149 (2009).

[46] M. Ablikim *et al.* [BESIII Collaboration], Phys. Rev. Lett. **110**, 022001 (2013).

[47] M. Ripani *et al.* [CLAS Collaboration], Phys. Rev. Lett. **91**, 022002 (2003)

[48] K. Park *et al.*, (CLAS Collaboration), Phys. Rev. C **91**, 045203 (2015).

[49] E. Golovach *et al.*, $\gamma p \to p\pi^+\pi^-$ cross sections from g11a experiment, CLAS ANALYSIS NOTE (in preparation).

[50] C.D. Roberts, J. Phys. Conf. Ser. **630**, 012051 (2015).

[51] C.D. Roberts and J. Segovia, arXiv:1603.02722 [nucl-th].

[52] A. Sarantsev, "The BoGa Amplitude Analysis Methods and its Extension to High W and to Electroproduction", the invited talk at the Workshop "Nucleon Resonances: From Photoproduction to High Photon Virtualities", ECT*, Trento, October 12-16 2015, http:/boson.physics.sc.edu gothe/ect*-15program.html

[53] H. Kamano, T-S. H. Lee, AIP Conf. Proc. **1432**, 74 (2012).

[54] H. Kamano, S. X. Nakamura, T-S. H. Lee, T. Sato, Phys. Rev. C **88**, 035209 (2013).

[55] N. Suzuki, T. Sato, and T-S. H. Lee, Phys. Rev. C **82**, 045206 (2010).

[56] G.V. Fedotov *et al.* [CLAS Collaboration], Phys. Rev. C **79**, 015204 (2009)

[57] Jefferson Laboratory Joint Physics Analysis Center, https://jpac.jlab.org/.

[58] T. Corthals, D.G. Ireland, T. Van Cauteren and J. Ryckebusch, Phys. Rev. C **75**, 045204 (2007).

[59] D.S. Carman *et al.* [CLAS Collaboration], Phys. Rev. Lett. **90**, 131804 (2003).

[60] D.S. Carman *et al.* [CLAS Collaboration], Phys. Rev. C **79**, 065205 (2009).

[61] M. Gabrielyan *et al.* [CLAS Collaboration], Phys. Rev. C **90**, 035202 (2014).

[62] P. Ambrozewicz *et al.* [CLAS Collaboration], Phys. Rev. C **75**, 045203 (2007).

[63] R. Nasseripour *et al.* [CLAS Collaboration], Phys. Rev. C **77**, 065208 (2008).

[64] D.S. Carman *et al.* [CLAS Collaboration], Phys. Rev. C **87**, 025204 (2013).

[65] B.A. Raue and D.S. Carman, Phys. Rev. C **71**, 065209 (2005).

[66] J. Nys, "Hunting the Resonances in $p(\gamma, K^+)\Lambda$ Reactions: (Over)Complete Measurements and Partial-Wave Analyses", the invited talk at the Workshop "Nucleon Resonances: From Photoproduction to High Photon Virtualities", ECT*, Trento, October 12-16 2015, http:/boson.physics.sc.edu gothe/ect*-15program.html

[67] For details see: https://www.jlab.org/Hall-B/clas12-web/

[68] C. Wu *et al.*, Eur. Phys. J. A **23**, 317 (2005).

[69] [Aachen-Berlin-Bonn-Hamburg-Heidelberg-Munich Collaboration], Phys. Rev. **175**, 1669 (1968).

[70] L.W. Mo and Y.S. Tsai, Mod. Phys. **41**, 205 (1969).

[71] V.I. Mokeev *et al.*, in "Proc. of the Workshop on the Physics of Excited Nucleon. NSTAR2005", ed. by S. Capstick, V. Crede, P. Eugenio, World Scientific Publishing Co., p. 47.

[72] I.G. Aznauryan, V.D. Burkert, G.V. Fedotov, B.S. Ishkhanov, and V.I. Mokeev, Phys. Rev. C **72**, 045201 (2005).

[73] CLAS12 Software Development,
see http://clasweb.jlab.org/clas12offline/docs/software/html/

[74] GEMC Documentation,
see https://gemc.jlab.org/gemc/Documentation/Documentation.html

[75] A. Afanasev, I. Akushevich, V. Burkert, and K. Joo, Phys. Rev. D **66**, 074004 (2002).

[76] T. Vrancx, J. Ryckebusch, and J. Nys, Phys. Rev. C **89**, no. 6, 065202 (2014)

[77] StrangeCalc website: http://rprmodel.ugent.be/calc/

[78] D. Luke and P. Soding, Multiple Pion Photoproduction in the s Channel Resonance Region, Springer Tracts in Modern Physics **59**, (1971).